Search for muonic W decays with the H1 detector at HERA

by

Christian Veelken

Suche nach $W \to \mu\nu$ Ereignissen am H1 Experiment bei HERA

Diplomarbeit
am II. Institut für Experimentalphysik
der Universität Hamburg

vorgelegt von
Christian Veelken

Hamburg
Juli 2001

Gutachter der Diplomarbeit: Prof.Dr. F.-W. Büßer

Prof.Dr. J. Meyer

Abgabedatum der Diplomarbeit: 06.07.2001

Zusammenfassung

Die Produktion reeller W-Bosonen wird in der ep-Streuung bei Hera mit einem totalen Wirkungsquerschnitt von etwa 1pb erwartet, wobei etwa 10% der Ws in ein Myon-Neutrino Paar zerfallen. In der in den Jahren 1994-97 und 1999-2000 am H1 Detektor genommenen Datenmenge mit einer integrierten Luminosität von $101pb^{-1}$ wird nach Kandidaten-Ereignissen fuer myonische W-Zerfälle gesucht.

Ein charakteristisches Merkmal dieser Ereignisse sind isolierte Myonen und fehlender Transversalimpuls. Die bisher von H1 publizierten Daten zeigten -bei geringerer Statistik- einen Überschuß von Ereignissen mit einer solchen Topologie. Neben einer im Vergleich zu den bisherigen Analysen grösseren Datenmenge wird in dieser Diplomarbeit ein erweiterter Phasenraumbereich betrachtet.

Abstract

Previous H1 publications reported an excess of events with an isolated high p_t lepton and missing transverse momentum. The dominant standard model contribution to the observed event sample is due to the production of W bosons. This analysis examines the muonic decay of W bosons produced in e-p collisions at Hera. It extends previous analyses to the $101pb^{-1}$ luminosity of the full 1994-2000 e^+ H1 dataset and investigates events in an enlarged kinematic region. The expected cross section for W production within the standard model is about $1pb$, with roughly 10% of all Ws decaying into a muon-neutrino pair.

Contents

Chapter 1

Introduction

The analysis presented here uses data taken during the years 1994 - 2000 with the H1 detector at DESY, Hamburg. The H1 detector is one of the two general purpose detectors of the HERA storage ring at DESY. HERA collides electrons respective positrons and protons at a center of mass energy of about 300 GeV which allows to study *deep inelastic lepton-nucleon scattering* at an energy scale one order of magnitude above previous fixed target experiments.

One can think of these scattering events as if the point-like electron or positron "probes" the structure of the proton. Because the *resolving power* is proportional to the energy in this process the increase of the center of mass energy in the lepton-nucleon system at HERA allows the structure of the proton to be evaluated down to smaller distances. At these small distances of the order $10^{-18}m$ one can study the point-like constituents of the proton, the *quarks*, and the force carriers (or, more technically, *gauge bosons*) which confine the quarks inside the proton, the *gluons*.

In the current *Standard Model* of particle physics the proton consists of three so called *valence quarks*. These carry a significant fraction of the total proton momentum. The rest of the momentum is split between gluons and low energetic quark-antiquark pairs called *sea quarks*, which are dynamically produced in quantum fluctuations out of gluons.

One of the observations made in deep inelastic scattering events was that only half of the proton momentum is carried by quarks while the other half is carried by gluons [8]. The momentum distribution between the constituents of the proton are described by the *structure functions* of the proton.

The slope of the structure functions is determined from the measurement of many thousands of events recorded at HERA and in fixed target experiments.

Another aspect of the high center of mass energy at Hera is that the *weak force* which is suppressed at lower energy by a gauge boson mass of nearly 100 GeV begins to contribute measurable to the scattering cross section.

The weak interaction can be tested best in *charged current* scattering events where the electron or positron is converted into a neutrino. A few thousand events of this kind are recorded by H1 in agreement with the standard model.

In contrast to the charged current scattering events where the gauge boson W of the weak interaction acts as a virtual particle propagating the momentum transfer Q^2 between electron or positron and proton the W can also be produced as a "real" particle in the final state. Four-vectors of real particles are *on mass*

shell in $E - |\vec{p}|$ space (they satisfy $p^2 = E^2 - \vec{p}^2 = m^2$).

These events are quite seldom at HERA. For approximately $100pb^{-1}$ luminosity in the e^+p dataset and an estimated cross section of $1pb$ one can expect 100 W production events in the whole H1 positron data taken so far. If one multiplies the produced number with the *branching ratio* of 10% for the W decay into muons, the decay channel considered in this analysis, and takes into account efficiency losses one ends up with the expectation of 2 to 3 such events in the data. In the data the H1 collaboration has reported an excess of events with isolated leptons and missing transverse momentum indicating a neutrino [5]. Events of this topology can best be explained as W production, although the rate expected from the standard model is lower than that observed.

In previous analyses [31] and also [28] the detection of muonic W decays was restricted by a set of triggers which are sensitive to a transverse imbalance of energy in the calorimeter. The electron is mostly scattered by a small angle thus having small transverse momentum components. Since the muon deposit only small energies in the calorimeter and the neutrino none the energy required by the triggers mainly cut in the transverse momentum of the hadronic system of the scattered quark. This significantly reduces the acceptance to about one third.

In this analysis the fraction of detectable muonic W decays is increased by using an additional trigger which is sensitive to events with a scattered positron in the detector. The trigger was developed for the detection of inelastic J/Ψ events and requires a muon signal in coincidence with an energy deposit in the calorimeters compatible with a single electron or positron. This additional, alternative trigger condition increases the acceptance (of the trigger system) by roughly 25% and allows the investigation of a different phase space region. It is interesting to examine whether the excess of events observed at higher hadronic transverse momenta continues to lower values in this extended phase space.

The thesis is divided into several sections. The first chapter consists of this introduction. The second chapter contains a short overview over theoretical aspects of W production in ep collisions including a brief discussion of production processes beyond the standard model. The third and fourth chapters continue with an overview over the experimental conditions. Therein a description of the HERA machine and the H1 detector components which are most relevant for the reconstruction of muonic W decay events will be given. The experimental section ends with a definition of the trigger conditions for the two investigated phase space regions of the calorimetric and electron triggered event samples. The fifth and sixth chapters will present a more detailed description of how muonic W decays look like in the detector and what background contributes to event samples with isolated muons and missing transverse momentum. These discussions will be made on the basis of *Monte Carlo* simulations of the underlying physical processes smeared by the simulated detector resolution. It turns out that a reliable muon identification is crucial for this analysis because the dominating background consist of processes where the required muon is not produced in the primary ep interaction but is a decay product of pions or kaons or a hadron which "fakes" a muon signal. The muon identification in the H1 detector is covered in the seventh chapter which then forms the basis for the eights chapter which describes specific further cuts to isolate muonic W production from the remaining background. The ninth chapter is devoted to the presentation of the results of the applied selection. Therein a comparison will

be given between the expected number of events on the one hand and the ones observed in the H1 data on the other hand. Finally the results are summarized and an outlook is given.

In this thesis *natural units* will be used in which

$$\hbar = c = 1.$$

Chapter 2

Theoretical overview of W production in ep scattering

This chapter describes the mechanisms for W production at HERA. It starts with the definition of common quantities to most ep processes and proceeds with a discussion of the standard model W production and two possible extensions of the standard model, *anomalous gauge boson coupling* and anomalous production of single top quarks in *flavour changing neutral current* processes.

2.1 General kinematics of ep reactions

The interaction

$$ep \rightarrow l \; + \; something$$

between electrons and protons at HERA can be described by the exchange of a virtual gauge boson. For low momentum transfers $Q^2 \ll M^2_{Z,W}$ it is sufficient to consider only photon exchange because the exchange of the heavy weak gauge bosons Z^0 and $W^{\pm}$ is suppressed by the square of the propagator $\frac{1}{Q^2+M^2_{Z,W}}$.

The Feynman graph for this reaction is shown in picture 2.1. Here k denotes the four-momentum of the incident electron, P that of the incident proton and k' that of the outgoing lepton.

These four-vectors define the *center of mass energy*

$$\sqrt{s} = \sqrt{(P+k)^2}.$$

If the exchanged gauge boson is electrically neutral (photon and Z^0) the process is called *neutral current* otherwise, if it carries a charge ($W^{\pm}$) the process is called *charged current*.

The *four-momentum transfer*

$$Q^2 = -q^2 = -(k-k')^2 \approx 4E_e E'_e sin^2\left(\frac{\theta'_e}{2}\right)$$

is related to the energy and angle of the outgoing lepton. The transfered momentum Q^2 describes the *virtuality* of the boson. For low Q^2 the photon is

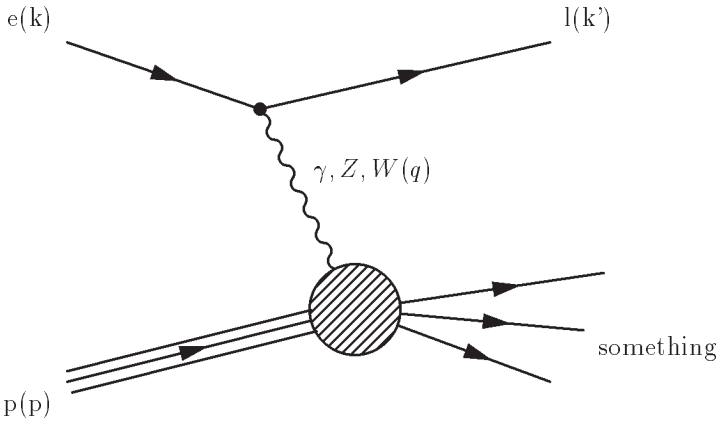

Figure 2.1: *General electron - proton reaction, the lepton l describes the scattered electron in* neutral current *or a neutrino* charged current *processes, something summarizes all particles despite the lepton*

almost real, or *on mass shell*. Using the energy-time uncertainty relation low virtualities allow for a longer lifetime of the photon. In this case the photon can fluctuate in a quark-antiquark pair. In these cases in addition to the *direct* interaction of the photon with the proton also a *resolved* process is possible where one of the quarks out of the photon interacts with the proton. These low Q^2 events are referred to as *photoproduction*.

The size of the proton is of the order 1 fm, which corresponds to Q^2 in the order of 1 GeV^2. For momentum transfers below this value the mediated boson does not resolve the proton, the proton remains intact and the scattering is said to be *elastic*. For higher Q^2 the boson does resolve the proton and usually interacts with a single quark inside the proton. Because the proton can dissociate in this process these events are called *deep inelastic scattering* (DIS).

There is a rather smooth transition between the low Q^2 photoproduction regime and the deep inelastic scattering events at higher Q^2 in the region of Q^2 in the order of 1 GeV^2.

For H1 the limit is derived from the geometry of the detector. For $Q^2 \gtrsim 4\,GeV^2$ the scattering angle of the electron is large enough to fall in the geometrical acceptance region of the H1 detector such that the scattered electron itself can be measured. This then marks the transition between photoproduction and deep inelastic scattering. For $Q^2 \lesssim 4\ GeV^2$ the lepton leaves the detector undetected through the beam pipe.

Another important variable is the *inelasticity* of the event, defined by

$$y = \frac{P \cdot q}{P \cdot k}, 0 \leq y \leq 1$$

which describes the relative momentum transfer of the electron.

2.2 W production

In the following an overview over processes which are capable of producing the observed experimental signature of events with an isolated muon and intrinsic

missing transverse momentum originating from a neutrino will be given. Processes where the isolated muon has hadronic origin or the reconstructed missing momentum is due to a simple miss-measurement will be treated as background in more detail in chapter four.

First the W production within the standard model will be discussed followed by a section about the possible extension to anomalous gauge coupling. The last section will describe physics beyond the standard model, anomalous production of single top quarks via *flavour changing neutral currents* which could enhance the observed W production rate and furthermore yields a natural explanation for the high hadronic transverse momenta in the observed isolated lepton events at H1 [5].

2.2.1 W production in the standard model

The dominant Feynman diagram for the production of real W bosons in ep collisions is shown in figure 2.2.

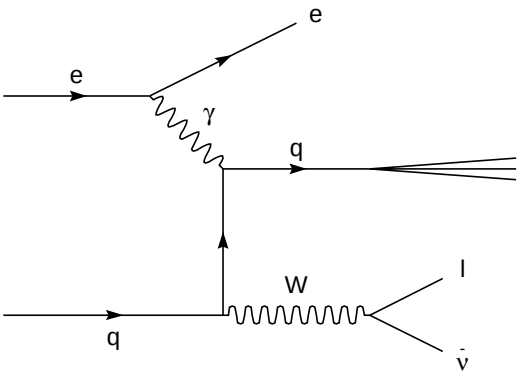

Figure 2.2: *Dominant contribution to real W production*

With a total cross section of about 1 pb (see calculations in the theory papers [7] and [37]) W production is comparatively rare at HERA. It would be therefore desirable to keep as many as possible of the events in the selection. Unfortunately the experimental signature of hadronic W decays which amount to a *branching fraction* of roughly 70% is not that different from photoproduction events with two or three jets in the final state which have a much higher cross section. It is therefore extremely difficult to isolate a W signal from this background [16]. The study of tauonic W decays is aggravated by the large fraction of tauons which decay hadronically and look quite similar to charged current scattering events. At the moment the only accessible decay channels are the electronic and muonic ones which have a much easier experimental signal. The selection of both channels is described in [31].

This analysis will limit to the muonic decay channel because it is the experimentally easiest (in the electronic channel the background is considerably higher due to badly measured deep inelastic scattering events) and also the one where the observed excess of events with isolated leptons [5] is concentrated.

The experimental signature of such an event consists of a jet formed by the

scattered quark, a muon and missing momentum carried away by the neutrino. Since the W decay is independent from the scattering process the muon is expected to be isolated from the jet in the detector and due to the high W mass both muon and neutrino will have high transverse momenta.

Standard model W production is simulated by the *EPVEC* Monte Carlo generator [14] based on the calculations presented in [7].

Some kinematic distributions predicted by EPVEC are shown in figure 5.1 for the discussion of typical event topologies. The simulated event properties are used for the determination of trigger and selection efficiencies, in the following all estimations of expected event rates will be taken from the Monte Carlo simulation. In the calculation of the W production cross section there are several technical difficulties which lead to a quoted error in the order of 30% [7]. It includes uncertainties from the *photon flux factor* of the electron, *parton densities* which describe the quark distribution of the proton and the *cut off parameter* which one has to introduce for the regularisation of divergences. In reference [37] the resolved part of the W production cross section was calculated in next to leading order and turned out to be 40% higher than the tree level one. As described in the same paper the calculated resolved part is expected to dominate the total cross section. Since in the high transverse momentum region of the observed excess the resolved part falls steeply such that the direct part becomes more and more important, the difference between tree level and higher order calculations remains an uncertainty there. The relatively large quoted error of 30% also covers the differences in the published cross sections. ($\sigma \approx 1.0$ in the calculation of [7] and [37], $\sigma \approx 1.3$ [27])

2.2.2 Anomalous gauge couplings

The dominant Feynman graph (see picture 2.2) displayed in the discussion of the standard model W production in the previous section is not gauge invariant alone. A gauge invariant description is achieved after the summation over all possible tree level Feynman diagrams which describe the process.

The complete gauge invariant set of leading order Feynman diagrams for standard model W production with subsequent muonic decay at HERA is shown in picture 2.3.

It include a diagram (e) with a $WW\gamma$ vertex which arises from the *nonabelian* nature of the electroweak interactions which is described by a $SU(2) \otimes U(1)$ gauge group. The standard model makes some simplifying assumptions on the structure of this *triple gauge boson coupling*. A general gauge invariant ansatz contains seven free parameters for the description of the $WW\gamma$ interaction [21].

After the requirement of C and P parity conservation in the electromagnetic $WW\gamma$ interaction the ansatz simplifies to two remaining free parameters κ and λ in the effective Lagrangian

$$\mathcal{L} = e\left(W^+_{\mu\nu}W^{\mu}A^{\nu} - W^{\mu\nu}W^+_{\mu}A_{\nu} + \kappa W^+_{\mu}W^+_{\nu}F^{\mu\nu} + \frac{\lambda}{m^2_W}W^+_{\rho\mu}W^{\mu}_{\nu}F^{\nu\rho}\right)$$

with photon field A^{μ} and field strength tensor $F_{\mu\nu} = \partial_{\mu}A_{\nu} - \partial_{\nu}A_{\mu}$.

In the standard model

$$\begin{aligned} \kappa &= 1 \\ \lambda &= 0, \end{aligned}$$

hence deviations from the standard model are parameterized by

$$\Delta\kappa \quad = \quad \kappa - 1 \text{ and } \lambda.$$

Because the standard model amplitude of the Feynman diagrams with the $WW\gamma$ vertex is relatively small compared to the dominant contribution (displayed in picture 2.2), one needs rather big deviations $\Delta\kappa$ and λ in the order of one to observe an effect at the HERA luminosity. This possibility is disfavored since the production of WW pairs at LEP2 has set strict limits on these parameters recently [19],

$$\begin{aligned} \Delta\kappa &= 0.08 \pm 0.17 \\ \lambda &= -0.04 \pm 0.07. \end{aligned} \tag{2.1}$$

2.2.3 Anomalous top production

Another possibility for the production of real W bosons is in the decay $t \to bW$. The high top quark mass could naturally explain the high hadronic transverse momenta observed in the isolated lepton events [5].

The center of mass energy at HERA does not allow for top pair production.

Within the standard model the rate for top production is negligible at Hera because the possible single top production in charged current reactions as displayed in picture 2.4 is highly suppressed. The cross section is tiny due to the propagator term of the virtual W boson and reduced further by the small elements V_{td} and V_{ts} in the *Cabibbo-Kobayashi-Maskawa* matrix which describe the coupling of the top to the quarks in the proton.

Despite the unobservable standard model production rate several models beyond the standard model (as in [17] and [13]) predict *flavour changing neutral currents* which would allow sizeable single top production in a process like the one shown in picture 2.5.

The flavour changing processes are described by the Lagrangian [22]

$$\begin{aligned} \mathcal{L} \quad = \quad & e\bar{t}\frac{i\sigma_{\mu\nu}q^{\nu}}{m_t + m_u}\left(\kappa_{tu\gamma} - i\kappa_{tu\tilde{\gamma}}\gamma_5\right) uA^{\mu} + \\ & e\bar{t}\frac{i\sigma_{\mu\nu}q^{\nu}}{m_t + m_c}\left(\kappa_{tc\gamma} - i\kappa_{tc\tilde{\gamma}}\gamma_5\right) cA^{\mu} + hermitian\ conjugate \end{aligned}$$

with CP conserving coupling parameters κ and CP violating $\tilde{\kappa}$.

Current experimental limits on the $tu\gamma$ and $tc\gamma$ couplings are taken from the branching ratios of top decays $t \to u\gamma$ and $t \to c\gamma$ in the Tevatron data and from top-charm associated production $\gamma \to tc$ at LEP2. The sensitivity of HERA is much higher for the anomalous coupling of the top to the u quark due to the more favorable parton density. The most stringent existing bound $\kappa_{tu\gamma} < 0.28$ ([2], with 95% confidence level) limits the anomalous single top cross section to $\sigma_{anotop} < 1pb$, high enough to produce a detectable signal. An H1 analysis of anomalous single top production gave preliminary results [1].

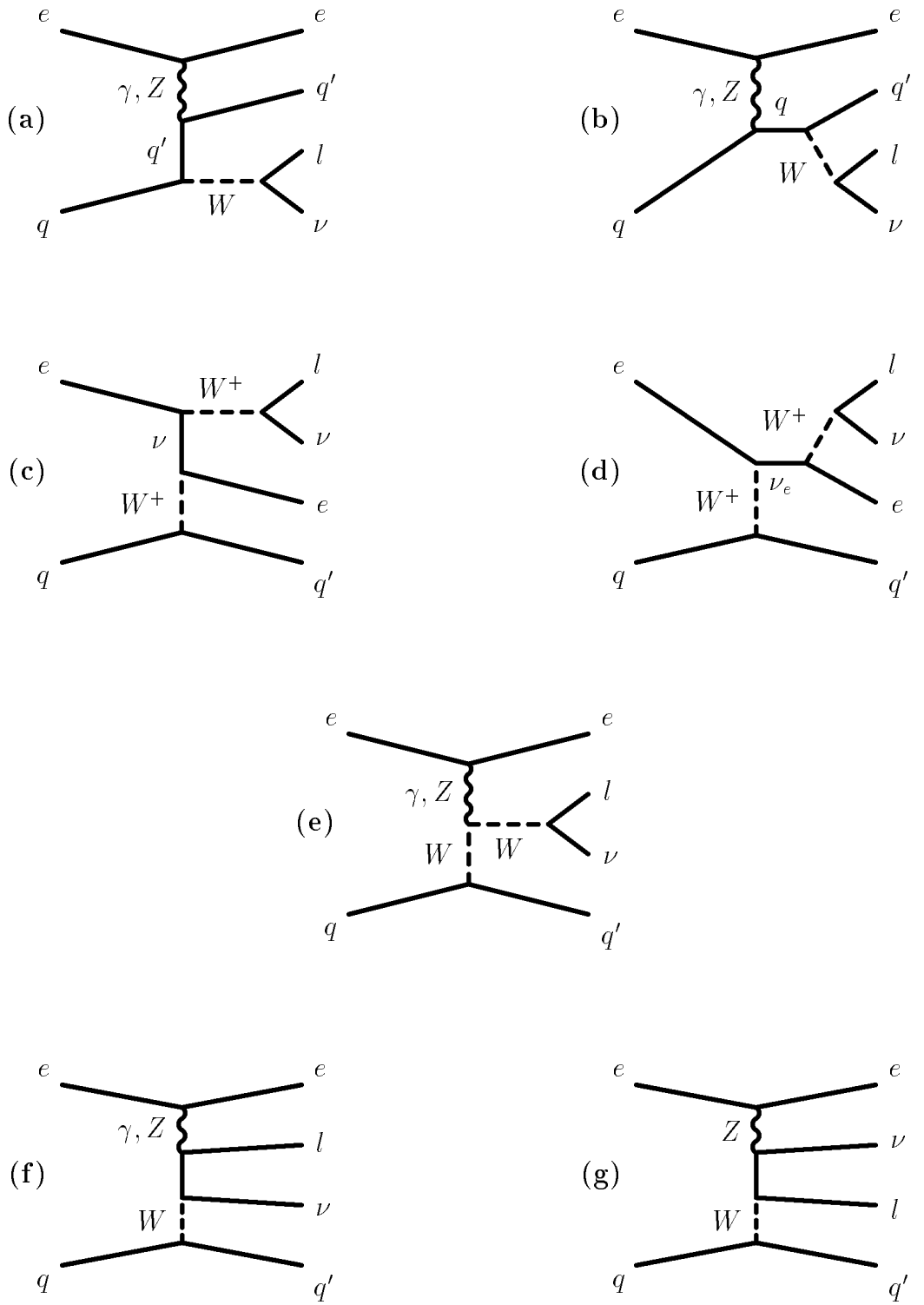

Figure 2.3: *Leading order Feynman diagrams for standard model W production (with subsequent leptonic decay)*

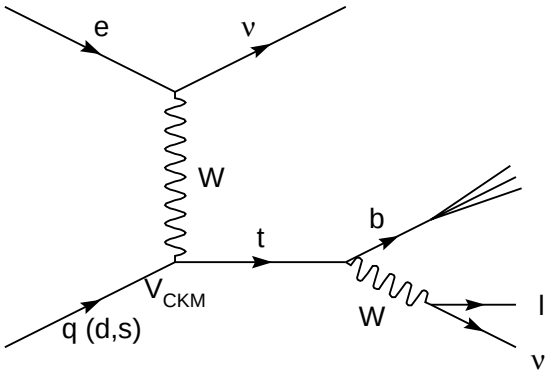

Figure 2.4: *Standard model production of single top quarks in ep collisions*

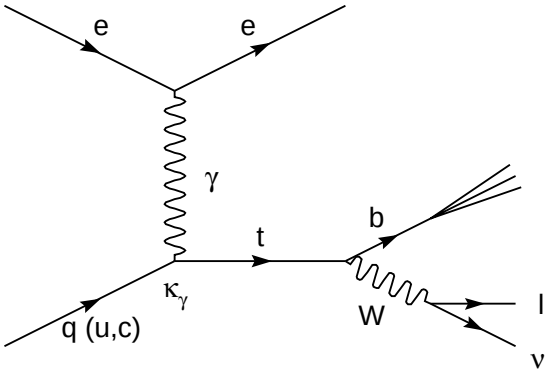

Figure 2.5: *Anomalous production of single top quarks at HERA via flavour changing neutral currents*

Chapter 3

HERA accelerator

The construction of the *Hadron-Elektron-Ringanlage* (HERA) was finished in 1990. HERA is a ring accelerator residing in a tunnel with 6.4 km circumference at *Deutsches Elektronen Synchrotron* (DESY) in Hamburg-Bahrenfeld some meters below the "Volkspark".

It consists of two storage rings, one for electrons or positrons and one for protons. For simplicity both electrons and positrons will be referred to as "electrons" in the following.

A sketch of the HERA ring is shown in picture 3.1.

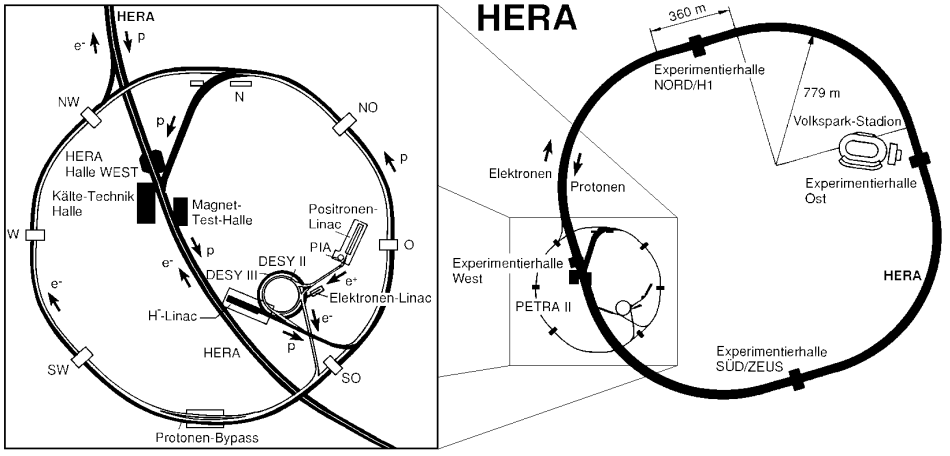

Figure 3.1: *Sketch of HERA ring accelerator with enlargement of pre-accelerators*

After being pre-accelerated in small linear accelerators and in the DESY and PETRA rings the electrons and the protons are fed into the HERA storage ring where they get accelerated to the final beam energies of 27.6 GeV for electrons and 820 GeV, since 1998 920 GeV, for protons.

The electron and proton beams are brought into collision in the interaction regions of the two general purpose detectors H1 and ZEUS located in the north and south experimental halls respectively.

year	luminosity $[pb^{-1}]$		
	delivered by HERA	recorded by H1	good data quality
1994	4.7	3.5	2.7
1995	10.1	6.2	3.8
1996	13.3	8.9	7.9
1997	32.4	27.3	21.3
1999	25.7	22.3	18.1
2000	66.8	59.4	47.2

Table 3.1: *Amount of e^+p data taken in individual years, "good data quality" requires stable run conditions and the operation and high voltage supply of necessary subdetectors*

The electrons and protons are stored in up to 220 *bunches* in the two rings with a time interval of 96ns between two consecutive bunch crossings. The typical number of *colliding bunches* was $\approx$ 175. The space between these is filled with *pilot bunches* of electrons and protons which are not colliding with any bunch from the other beam. Since no ep reactions should take place in the pilot bunch crossings they allow for beam-wall and beam-gas background studies. Every bunch consists of approximately 10^{11} particles. The particle density within a bunch follows in longitudinal direction a Gaussian distribution with a width of $\sigma_e \approx 1$ cm and $\sigma_p \approx 10$ cm [29] for the electron and proton bunches respectively. This translates in a Gaussian distribution of event vertices around the nominal *interaction point*.

In 1994-97 positrons were accelerated to an energy of 27.6 GeV and protons to 820 GeV leading to a center of mass energy of $\sqrt{s} = 301$ GeV in the collision. During this period HERA delivered data with $60.5pb^{-1}$ integrated luminosity to the H1 experiment. In 1998 the proton beam energy was increased to 920 GeV leading to a center of mass energy of $\sqrt{s} = 319$ GeV. Between 1998 and 1999 HERA was run with electrons and delivered $24.8pb^{-1}$ to H1. This relatively small data set is not used in this analysis. For the 1999-2000 running period HERA was again filled with positrons and operated with the increased proton beam energy of 920 GeV. Additional $92.5pb^{-1}$ positron data were delivered by Hera in that time.

A summary of the luminosity yield over these years is given in table 3.1. The three columns in this table quote the luminosity delivered by Hera, the amount recorded by H1 and the fraction of the recorded luminosity which has a sufficient data quality. The *luminosity* describes how many physics processes happen in the H1 detector and is measured with *Bethe-Heitler* processes ($ep \rightarrow ep\gamma$) which have a well known cross section. In practice not all ep events in the H1 detector are available for analysis. Due to occasional problems in the event read out chain of the data acquisition system the luminosity recorded by H1 and written on tape is lower. From these a further fraction is lost when subdetectors fail or the high voltage supply breaks down. Individual runs are also rejected if there are very noisy ("hot") cells in the calorimeter or a problem with the Hera machine occurs after a short time of running. Events from runs which fulfill these criteria are said to have a good data quality and are available for this analysis. They amount to $35.7pb^{-1}$ in the 1994-97 and to $65.3pb^{-1}$ in the 99-

2000 running period adding up to $101pb^{-1}$ in the 94-00 e^+ data set used in this analysis.

As already mentioned in the introduction this analysis will concentrate on the positron data - but will nevertheless still continue the common practice to refer to the positrons as electrons in the following.

Chapter 4

H1 detector

The H1 detector is built around the northern collision point of the HERA ring. It is designed to measure the direction, energy and charge of the particles resulting from the ep collisions in its center. From these information also a particle identification can be derived. The detector is asymmetric with a concentration of the instrumentation in the *forward* region defined as the direction of the proton beam. Unlike most other collider experiments the center of mass system of the colliding particles is not at rest in the laboratory frame but boosted with $\gamma_{cm(ep)} = 2.86$ along the proton direction. In the following the direction of the electron beam will be often referred to as *backward* region.

A sketch of the detector is shown in figure 4.1 together with the H1 coordinate system. Its origin is located at the nominal interaction point where the bunch crossing of the electron and proton beam takes place. The z-axis is chosen in direction of the proton beam with the polar angle θ defined as the angle between the particle trajectory and the proton beam. The x-axis points to the center of the HERA ring and the y-axis upwards. The azimuthal angle ϕ is defined such that $\phi = 0°$ on the x-axis and $\phi = 90°$ on the y-axis.

In the design of the detector prime attention has been given to the clean identification of electrons and to their energy measurement. To facilitate this the electromagnetic [4] and hadronic calorimeters [5] are put inside a large coil [6] which produces the magnetic field for the track momentum measurement in the drift chambers [2,3] which surround the interaction point in the innermost part of the detector. With this technique the amount of dead material in front of the calorimeters is kept small and together with the high granularity of the *liquid argon* calorimeter it allows for a good separation of electrons from hadrons by their shower shape. The iron return yoke [10] of the coil is instrumented with *limited streamer tubes* for muon identification. The instrumented iron is in addition equipped with a *tail catcher* system which allows to identify hadronic energy "leaking" out of the calorimeter. The muon system is complemented in the forward region by the *forward muon toroid* [11] a toroidial magnet surrounded by additional drift chambers on both sides suiteable to measure tracks of particles near the proton beam direction. The angular covering is increased by the *plug* calorimeter [13] in the very forward region and an electromagnetic calorimeter in the backward region [12]. In 1995 the former *backward electromagnetic calorimeter* (BEMC) was replaced by the *spaghetti calorimeter* (SpaCal) which has a higher granularity and also a hadronic section. The remaining holes in the

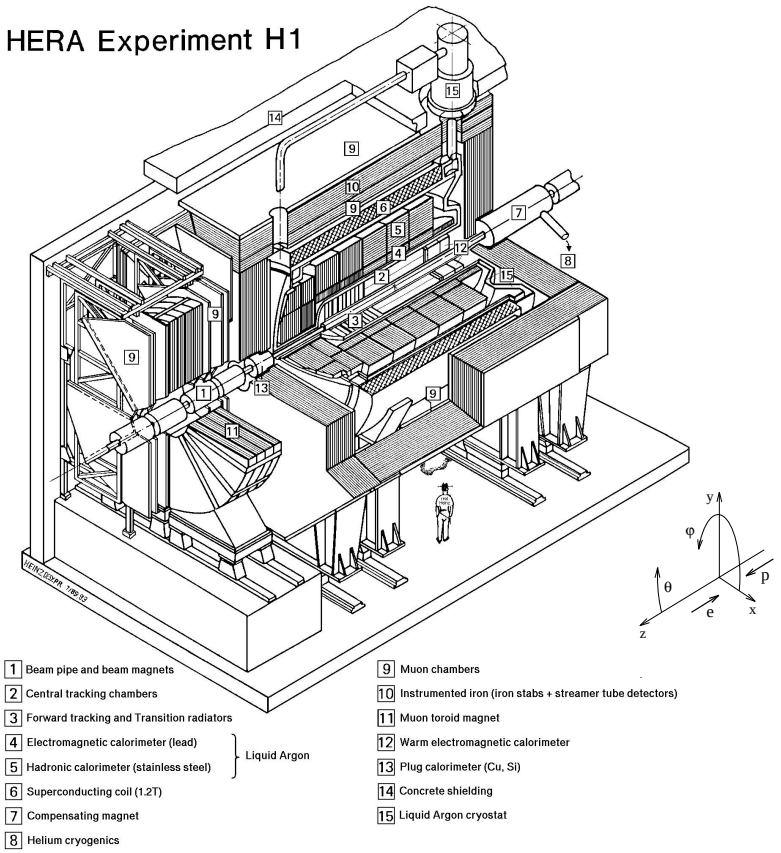

Figure 4.1: *Schematic view of the H1 detector, taken from the design paper [3] where also a more detailed description is given*

geometrical acceptance of the detector are mainly due to the beam pipe, with small contributions from cabling, cooling and structural supplies. The main detector system measures approximately 12 m length $\times$ 10 m width $\times$ 15 meters height and weights $\approx$ 2800 tonnes.

Due to the short bunch crossing period of 96 ns and a high proton induced background from beam-gas and beam-wall interactions an efficient multi level trigger system is needed to keep the data flow manageable. For the rejection of non-ep background produced "upstream" of the detector by the proton beam two scintillator walls with good timing resolution are installed in the backward region which supply a veto condition for the trigger.

4.1 Tracking system

The tracking system provides track triggering and reconstruction. The drift chambers form the innermost part of the detector such that the particles can be measured before they loose energy in the calorimeters or develop showers in

some dead material.

The tracking chamber is divided into three angular regions each optimized for the measurement of particle tracks into its angular region. The *forward tracking detector* (FTD) is displayed together with the *central tracking detector* (CTD) and the *backward drift chamber* (BDC) in the enlarged clipping of the detector center shown in picture 4.2.

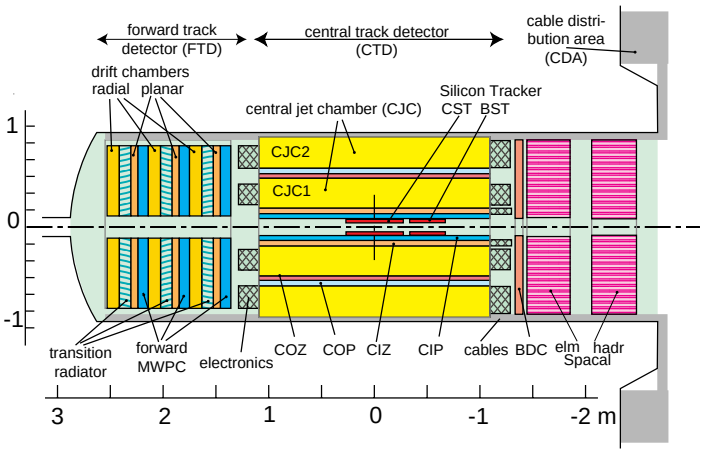

Figure 4.2: *Enlarged view of the H1 tracking system in $r-z$ projection*

The geometrical acceptance regions of the tracking detectors are summarized in the following table

detector	θ_{min}	θ_{max}
FTD	5°	25°
CTD	10°	165°
BDC	150°	177.5°

Tracks in the proton direction near the beam pipe are measured by the forward tracker and the ones in the central region of the detector are measured by the central tracker. These tracks are then called *forward tracks* and *central tracks* respectively. For tracks with polar angles between 10° and 25° degrees both central and forward tracker measure short track segments which are then linked to a *combined track*.

The reconstruction software of the tracking detectors searches for possible track segments in the wire hits of the drift chambers and calculates their curvature in the magnetic field. The transverse momentum of a unit charged particle is then determined by the curvature radius R as

$$p_T[GeV] = 0.345\ R[m]$$

(for a magnetic field of 1.15 Tesla in the H1 detector). Because the spatial resolution of the drift chambers is constant for all tracks while the curvature of high momentum tracks differ only by a small amount from an entire straight line, the momentum resolution of the tracking detectors degrades for higher p_T,

roughly as

$$\frac{\sigma(p_T)}{p_T} \sim 1\% \cdot p_T \ [GeV].$$

The reconstruction is such that the transverse momenta of the tracks tend to get underestimated rather than overestimated. Only for stiff high momentum tracks with $p_T \gtrsim 25\ GeV$ the transverse momentum is sometimes overestimated.

It should be noted that often short track lengths do not allow for a precisely determined curvature and the obtained value for the transverse momentum is then dominated by the extrapolation and constraint to the event vertex. The momentum measurement of the tracks therefore depend on the vertex reconstruction. This dependence gets stronger in the forward region when individual track segments in the forward tracking detectors have to be combined with each other or a track segment in the central tracker.

4.1.1 Central tracking detector (CTD)

The central tracking detector covers the largest part of the polar angle range. Its main component are two large concentric drift chambers with wires parallel to the beam axis. The *central jet chambers* (CJC) provide a space point resolution of $\sigma_{r\phi} = 170\mu m$ in the transverse $r\phi$ plane yielding a good resolution of the azimuthal track angle. Both drift chambers are built as gas-tight mechanically distinct units with a length of $\Delta z = 2200mm$ starting at $z = -1125mm$. The inner one (CJC1) extends from $r_i = 203mm$ to $r_o = 451mm$, the outer one (CJC2) from $r_i = 530mm$ to $r_o = 844mm$. By comparison of the signals read out from both wire ends a longitudinal precision of one percent of the wire length can be achieved in z, corresponding to $\sigma_z = 22mm$. The measurement of the polar angle is complemented by the *central inner z chamber* (CIZ) and the *central outer jet chamber* (COZ) which improve the z resolution to $\sigma_z = 300\mu m$. The inner z chamber is located at the inner surface of CJC1 and has the cross section of a regular 16-edge polygon with an edge length of 9 cm and wires in four planes parallel to the edges. The outer z chamber separates the inner CJC1 from the outer CJC2. It has a 24-fold symmetry with an edge length of 12 cm, like the inner z chamber also with four parallel wire layers.

Next to the inner and outer z chambers the central tracker has multi-wire proportional chambers (CIP and COP) which provide a fast timing signal with a good time resolution for trigger purposes.

An overview of the radial structure of the central tracking detector is given in picture 4.3.

The *sense wires* collect the low energetic *drift electrons* set free from the gas atoms in the drift chamber when charged tracks traverse the chamber volume. They are put on positive potential as anodes to accelerate the negatively charged electrons. The sense wires are separated by two *potential wires* which isolate the sense wires from each other and improve the shape of the drift field. The planes of sense wires and potential wires parallel to the beam line are tilted by about 30° with respect to the radial direction such that the ionisation electrons which get deflected by the *Lorentz angle* in the presence of the magnetic field drift approximately perpendicular to stiff high momentum tracks. This improves the resolution and helps to resolve ambiguities in the track reconstruction. Since the measurement of the drift time to each wire fixes the position of the corresponding

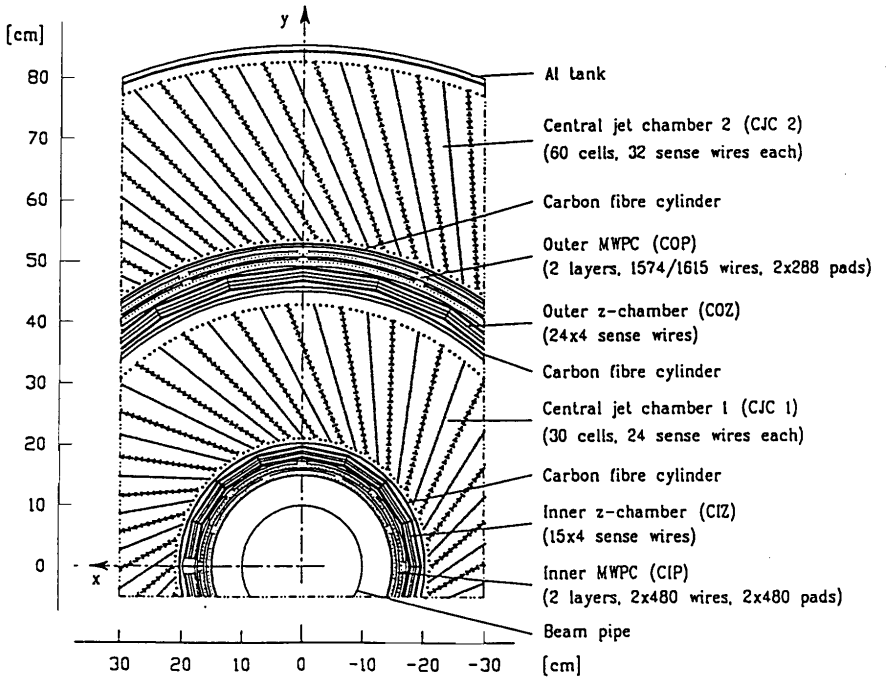

Figure 4.3: $r - \phi$ *view of the central tracking chamber*

ionisation only up to a circular area *mirror tracks* can occur as a second solution to the real tracks as illustrated in figure 4.4.

The sense wire planes are divided into cells by cathode wire planes. The cathode wires are set to a negative voltage proportional to the distance from the sense wire plane in order to create a uniform *drift field* and hence a constant drift velocity over almost all the cell.

The ends of the sense wire planes are surrounded with *field wires* at the inner and outer radii of the central jet chambers which further improve the uniformity of the drift field.

4.1.2 Forward tracking detector (FTD)

Precise momentum measurement of particle tracks is difficult in the forward region because tracks with small polar angles do not traverse the full radius in the transverse plane of the bending solenoid magnetic field.

This has been taken into account by a higher wire density in the forward tracker. The complete forward tracking detector consists of an integrated assembly of three nearly identical *supermodules* which are slightly tilted with respect to each other in azimuth. Each supermodule includes, in increasing z: three different orientations of planar wire drift chambers designed to provide accurate θ measurements, a multi-wire proportional chamber for fast triggering, a passive *transition radiator* and a radial wire drift chamber which provides accurate ϕ measurements and moderate radial position information by charge division from the wire ends at the inner and outer radii.

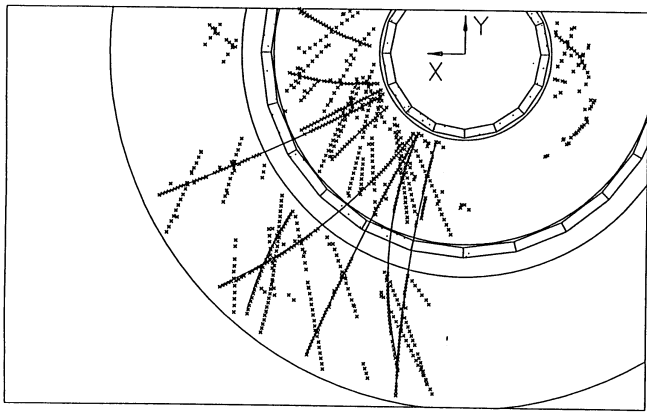

Figure 4.4: *Illustration of* mirror tracks *in the tracking detectors*

The three planar wire drift chambers each have a depth of four wires and are rotated at 60° to each other in azimuth to provide homogeneous spatial precision in x and y.

The radial drift chamber extends over twelve wire layers. The radial chamber also measures the transition radiation X-ray emission produced when charged particles traverse the dielectric foils inside the upstream transition radiator. The amount of transition radiation should improve the electron-pion discrimination because unlike ionisation losses which depend on the particle velocity β and differ only by a small amount for high energetic electrons and pions the energy loss due to transition radiation is proportional to the *Lorentz factor* $\gamma = \frac{E}{m} = \frac{1}{\sqrt{1-\beta^2}}$. In practice the transition radiation detection was not as useful as estimated and the transition radiator will be removed in future data taking.

An overview of the assembly of the forward tracker is given in figure 4.5.

By linking short track segments from different supermodules a reasonable tree dimensional track reconstruction becomes possible.

4.1.3 Backward drift chamber (BDC)

The backward drift chamber was installed as part of the 1995 upgrade of the H1 detector. It replaced the former *backward proportional chamber* (BWPC). Since most of the data used for this analysis was taken after this upgrade only the BDC will be described here. Description of the BWPC can be found in [3].

The backward drift chamber is displayed in picture 4.2. It consists of eight wire layers displaced in the z direction and parallel to the $r\phi$ plane, with each layer divided into eight sectors in ϕ and each sector having 32 drift cells. The eight layers are paired up and each pair is rotated by 11.25° in azimuth with respect to the previous pair. The entire structure is then mounted in front of the spaghetti calorimeter.

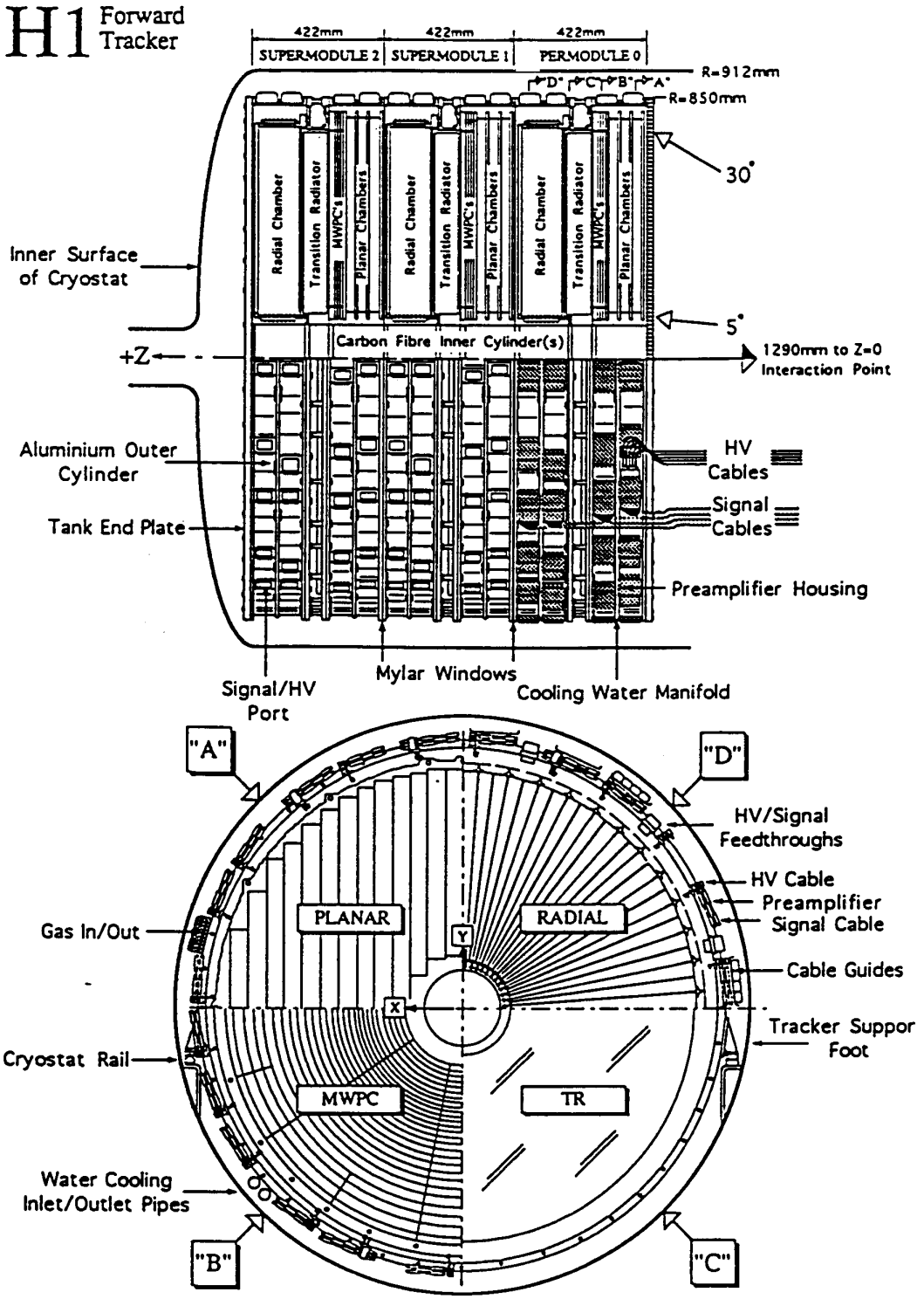

Figure 4.5: *Forward tracking detector in $r-z$ view showing the chamber structure in the upper half and wire orientation in $r-\phi$ view in the lower half of the picture*

4.2 Calorimeters

The Calorimeters measure the energy (and the absolute momentum $|\vec{p}| \approx E$) of high energetic particles (despite muons) with much better precision than the tracking detectors. They also allow an estimate of the direction of a particle and are the only way to measure electrically neutral particles.

Calorimetry at H1 is mainly done in the *liquid argon calorimeter* capable of measuring electrons and hadrons in the forward and central region between $5° \leq \theta \leq 153°$. Full angular covering is increased by the *plug* calorimeter which measures the hadronic energy flow in the very forward region $0.6° \leq \theta \leq 3°$ and the *spaghetti calorimeter* in the backward region $153° \leq \theta \leq 177.5°$ mainly for the measurement of electrons in low Q^2 scattering events.

All three calorimeters are "sandwich" constructions with alternating layers of "passive" *absorber plates* and "active" *sampling material*. High energetic particles traversing the absorber layer undergo multiple interactions with the absorber material, producing secondary particles which can interact with the absorber again to develop a cascade of progressively lower energetic *shower particles*. The energy of the shower produced in the absorber layers is then measured in the inbetween sampling layers. The shower development stops when ionisation losses of the shower particles exceed the production of new shower particles, the shower dies out. If neither the high energetic incident primary particle nor the secondary shower particles leave the calorimeter volume the shower is said to be "fully contained" within the calorimeter and the energy of the incident particle is then proportional to the amount of ionisation collected in the sampling layers.

Electrons passing through an absorber layer rapidly loose energy in *bremsstrahlung* processes due to their low mass. The energy loss is characterized by the *radiation length* X_0 after which the electron lost on average all but $\frac{1}{e}$ of its initial energy. Lead the most common electromagnetic absorber has a radiation length of $X_0 \approx 0.56cm$. Radiated photons with an energy above some MeV (at the threshold of $E = 2m_e$ Compton scattering dominates the energy loss) will produce new electrons in electron-positron *pair production* after traveling a mean distance of approximately one further radiation length. Because of the small radiation length electromagnetic showers have a fast exponential growth which allow for thin electromagnetic calorimeters.

The development of hadronic showers is typically much slower so that a larger depth is required for hadronic calorimeters. Hadrons and mesons interact with the nuclei of the atoms in the absorber. In these interactions secondary strongly interacting particles are produced resulting in the development of a hadronic shower. The characteristic scale over which such a shower growths is described by the *hadronic interaction length* λ which is much larger than X_0 for most materials. For both lead and steel is $\lambda \approx 17cm$.

Therefore much absorber material is needed to measure hadronic particles and electromagnetic calorimeters are placed before hadronic ones nearer to the interaction point. Hadronic showers differ from electromagnetic ones also in their greater transverse extension. The *shower shape* is used for discrimination by the *electron finder*.

4.2.1 Liquid argon calorimeter (LAr)

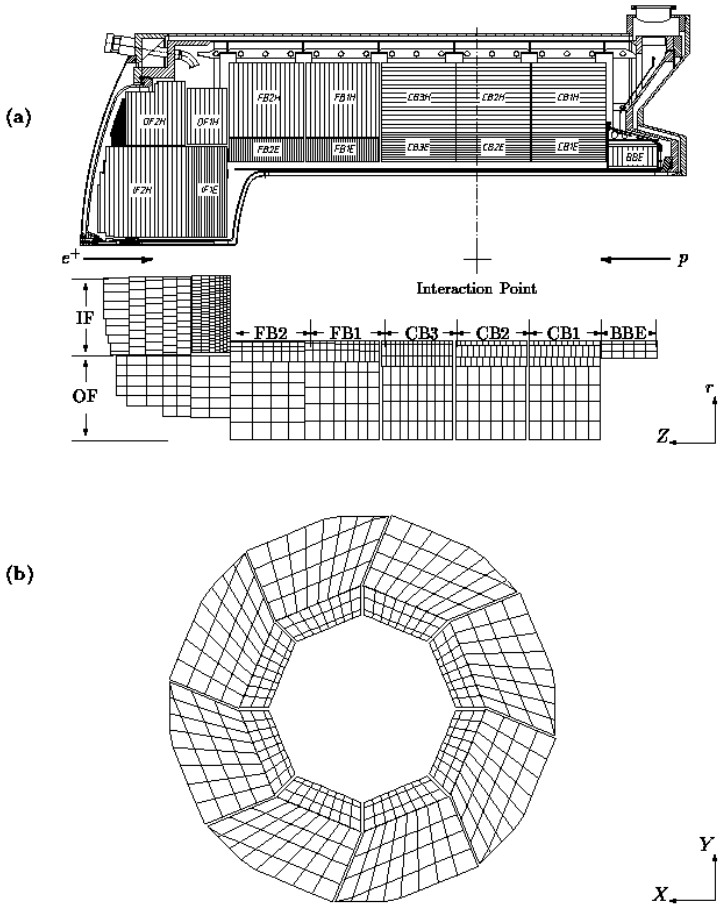

Figure 4.6: *Liquid argon calorimeter in $r-z$ view (a) showing the division into individual parts and the orientation of absorber layers in the upper half of and the cell segmentation in the lower half of (a) and in $r-\phi$ view (b)*

In the upper part the electromagnetic and hadronic sections of the liquid argon calorimeter can be seen with the horizontal and vertical lines indicating the orientation of the absorber plates. For the inner electromagnetic section 2.4 mm thick plates of lead are used as absorber, for the outer hadronic section 16 mm stainless steel plates. The gaps between the absorber plates is filled with liquid argon as sampling medium and instrumented with rectangular cathode pads for the readout of the ionisation charge. The high density of the liquid argon results in an efficient ionisation production and a good energy resolution

of

$$\frac{\sigma_{em}(E)}{E} \approx \frac{15\%}{\sqrt{E[GeV]}}$$
$$\frac{\sigma_{had}(E)}{E} \approx \frac{50\%}{\sqrt{E[GeV]}}$$

The calorimeter is *non compensating* which means that for the same incident particle energies the signal for hadrons is only $\approx 70\%$ of that for electrons. The reason for the lower response to strongly interacting particles is that the other $\approx 30\%$ of the energy are on average lost in excitations of nuclei in the traversed material. This effect is corrected for by an energy reweighting algorithm in the event reconstruction software.

The liquid argon calorimeter is built of different "wheels", with increasing z these are the *backward barrel electromagnetic calorimeter* (BBE), the *central barrel calorimeter modules* (CB1, CB2, CB3), the *forward barrel calorimeter modules* (FB1, FB2) and the *inner and outer forward calorimeters* (IF, OF). Apart from the BBE which consists of an electromagnetic section only and the OF which consists of two hadronic sections all wheels have an electromagnetic and a hadronic section. The wheels are divided in azimuthal angle into eight octants (see $r\phi$ view of figure 4.6). Between the individual modules there are insensitive regions indicated by gaps in the picture which are problematic for the energy measurement due to inevitable energy losses in these regions. The walls between the wheels are called *z-cracks*, the ones between the octants *ϕ-cracks*.

For a good spatial resolution of deposited energies the liquid argon calorimeter is highly segmented, into 45000 cells in total. Both electromagnetic and hadronic sections are deeper and more segmented in the forward region, where the particle density is higher due to the beam asymmetry. The cell sizes vary and are optimized to measure the longitudinal and transverse extension of electromagnetic showers which are used for the identification of the scattered electron. The segmentation of the calorimeter into cells is shown in the lower part of the rz view in figure 4.6. The depth of the electromagnetic section is $\approx 20 - 30$ radiation lengths, the total depth of the calorimeter $\approx 5 - 8$ interaction lengths.

The angular dependence of the depth of the calorimeter in units of interaction lengths for hadrons and mesons is displayed in figure 4.7.

It sometimes happens that hadronic showers are not fully contained in the liquid argon calorimeter which leads to an underestimation of the energy of the associated hadronic system. An estimate of such "leakage" can be achieved by the readout of the *tail catcher* which detects ionisation caused by hadronic showers in the instrumented iron yoke. A more detailed description of the tail catcher will be given in the following section as part of the muon system.

4.2.2 Plug calorimeter

The *plug calorimeter* (Plug) is located in the iron return yoke of the solenoid magnet. It is situated in the very forward region of the detector and covers the gap between the liquid argon calorimeter and the beam pipe. Because the available space in the return yoke is limited to a cylinder with $0.7m$ length and $0.7m$ diameter the calorimeter had to be built very compact. A silicon instrumented sampling calorimeter with nine passive copper layers was chosen

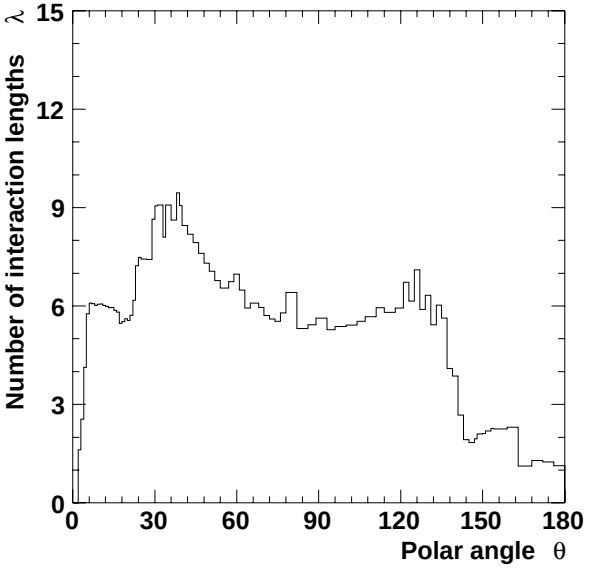

Figure 4.7: *Amount of material between the interaction point and the instrumented iron in strong interaction lengths as a function of the polar angle θ. Due to support structures, cabling and cryogenic supplies the amount of material is not simply proportional to $1/sin\,(\theta)$ (picture taken from reference [30]).*

and installed in the cylindrical gap. The energy resolution is limited by the coarse sampling and the incomplete containment of showers and is estimated to be

$$\frac{\sigma_{plug}(E)}{E} \approx \frac{150\%}{\sqrt{E}}.$$

4.2.3 Spaghetti calorimeter (SpaCal)

Since the H1 upgrade in 1995 the spaghetti calorimeter (SpaCal) resides in the backward region of the H1 detector replacing the former *backward electromagnetic calorimeter* (BEMC). Since only a small part of the data used in this analysis was taken with the backward electromagnetic calorimeter, the description will concentrate on the SpaCal here. A description of the BEMC can be found in [3].

The spaghetti calorimeter owes its name a few millions of scintillating fibers embedded in a lead matrix. Incident particles shower in the lead causing the embedded fibers to emit scintillation light. The basic structure of the lead plates holding the fiber bundles is shown in figure 4.8 with lengths given in units of millimeters for the electromagnetic section.

Individual lead plates are put together and coupled to a light mixer connected to a photomultiplier. Such a unit is displayed in figure 4.9.

The electromagnetic section is 28 radiation lengths deep with a spatial resolution of a few millimeters and an excellent energy resolution for electrons

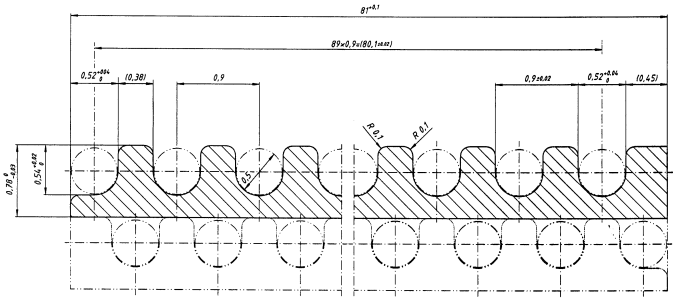

Figure 4.8: *Front view of a lead plate with 0.5 mm diameter scintillating fibres in the* spaghetti calorimeter

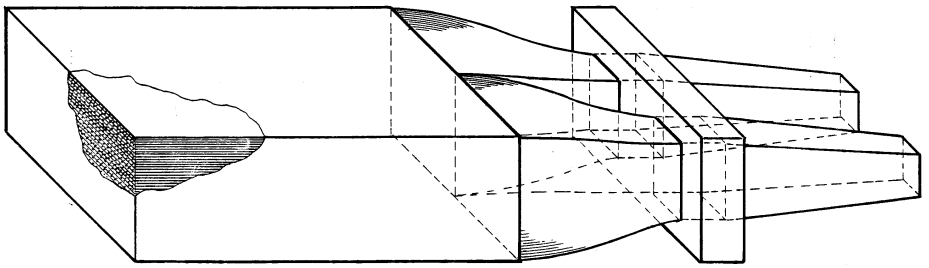

Figure 4.9: *SpaCal submodule*

of

$$\frac{\sigma_{em}(E)}{E} \approx \frac{7.5\%}{\sqrt{E[GeV]}}.$$

The hadronic part has a coarse fiber structure reflecting the greater lateral extent of hadronic showers The hadronic section is approximately one interaction length in depth and has an energy resolution of

$$\frac{\sigma_{had}(E)}{E} \approx \frac{55\%}{\sqrt{E[GeV]}}.$$

4.3 Muon System

Muon identification in the H1 detector is based on the detection of penetrating particles behind iron layers. While high energetic muons only loose roughly one GeV due to ionisation if they traverse one meter in iron, the same meter in iron means a wall of approximately five interaction lengths for hadrons and mesons and more than fifty radiation lengths for electrons.

In the central detector region

$$6^\circ \leq \theta \leq 172^\circ$$

muons are identified in the instrumented iron yoke while their momentum is measured in the central and forward tracking detectors.

In the forward region

$$3^\circ \leq \theta \leq 17^\circ$$

muons are measured and identified by the *forward muon detector*. The forward muon system is built from drift chamber planes mounted on either side of a toroidal magnet.

4.3.1 Instrumented iron return yoke

The iron yoke which returns the magnetic flux of the solenoid magnet is built of ten iron plates with a thickness of $7.5cm$ each. The plates are separated by slits which are on average $2.5cm$ wide allowing the gaps to be equipped with *limited streamer tubes* (LST). The central muon system is divided into three parts, the *forward* and *backward end-caps* and the *barrel* in the central region.

For safety reasons the limited streamer tubes are built of the halogen free plastic Luranyl. They are operated with a non-inflammable gas mixture of 88% CO_2, 9.5% isobutane and 2.5% argon at normal pressure.

One LST unit contains eight cells with a size of $10 \times 10mm^2$. The anode is built from a silver coated Cu-Be wire of $100\mu m$ diameter kept at ground potential in the center of each cell. The cell walls are made conducting by a coat of graphite paint and act as cathodes with $4.5kV$ high voltage applied to them. Two of such units are put together in a gas tight box which is shown in picture 4.10.

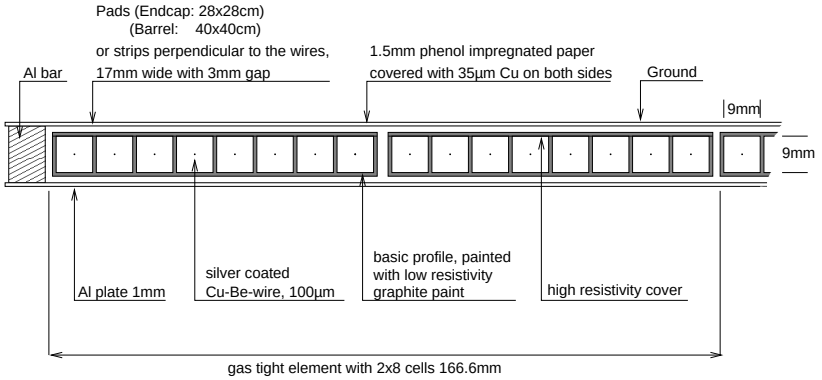

Figure 4.10: *Structure of a limited streamer tube with two units of eight cells each*

A complete streamer tube layer is built of several boxes which are mounted on an aluminum plate. Either *strips* or *pads* are glued onto one side of the planes. They act as electrodes where influence charges are induced and measured when passed by a charged particle. The strips are $17mm$ wide with a spacing of $3mm$. The size of the pads varies from $25 \times 25cm^2$ in the end-caps to $50 \times 50cm^2$ in the barrel region.

In total the iron yoke is instrumented with 16 layers of limited streamer tubes, 11 of these are equipped with pads.

The wire orientation in the tubes is parallel to the z-axis in the barrel and parallel to the x-axis in the end-caps. The strips are mounted perpendicular to the wires allowing for a two dimensional space measurement in the streamer tube layers. Wires and strips are read out digitally to provide *hits* in the instrumented iron. The analog signals from the five inner and the six outer pad layers are summed up to form two *tower signals*. These towers yield a rough energy estimate with a resolution of

$$\frac{\sigma_{tc}(E)}{E} \approx \frac{100\%}{\sqrt{E}}$$

and constitute the *tail catcher* (TC).

The configuration of the layers within the iron yoke is shown in figure 4.11. All slits contain at least one LST layer with pad electrodes. On the inside three layers are mounted in a *muon box* in front of the iron yoke. The muon box is a mechanically distinct unit holding one pad and two strip layers. The fourth slit in the iron has a doubled width of $5cm$ and contains two layers, one with pads and one with pads and strips. On the outer side of the iron another muon box is mounted.

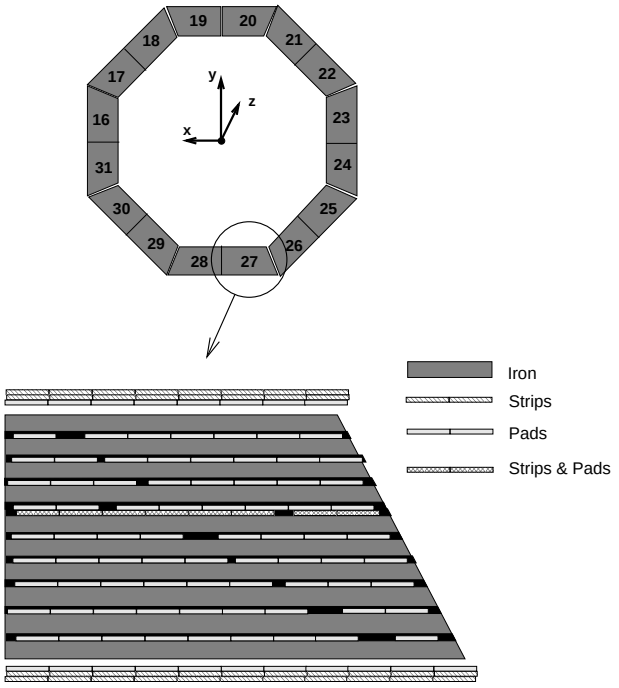

Figure 4.11: *Configuration of the streamer tube layers in the instrumented iron yoke, the upper half shows a transverse section of the barrel and the lower half an enlargement of one of the octants. Areas not filled with limited streamer tubes are marked black*

Since the barrel gets broader on the outside while the tubes have a fixed size some gaps had to be inserted between them as can be seen from the sketch of

the barrel octant in picture 4.11. The alignment of these gaps is made such that they do not line up for particles coming from the interaction point.

The geometrical acceptance of the muon system is limited by three holes in the instrumentation with streamer tube layers. One hole at ($\phi \approx 90°$, $\theta \approx 75°$) is due to a liquid argon transfer line, two further regions at ($\phi \approx 90°$, $\theta \approx 120°$) and ($\phi \approx -90°$, $\theta \approx 120°$) are occupied by cryogenics supply. These insensitive regions reduce the overall muon detection efficiency in the instrumented iron by $\approx 10\%$.

4.3.2 Forward muon detector

The *forward muon toroid* (FMT) is built to detect and measure charged particles penetrating through the forward end-cap of the main H1 detector at polar angles in the range $3° \leq \theta \leq 17°$. It is designed to provide a good momentum resolution between 5 GeV and 200 GeV for muons, the lower limit determined by the energy loss in the liquid argon calorimeter and the iron yoke and the upper one determined by the maximum field of the toroid and the spatial resolution of the drift chambers. It achieves a resolution of

$$\frac{\sigma_{fmt}(p)}{p} \approx 24\% \text{ for } p = 5\ GeV \text{ and } \frac{\sigma_{fmt}(p)}{p} \approx 36\% \text{ for } p = 200\ GeV.$$

The iron toroid has an inner radius of $0.65m$, an outer radius of $2.9m$ and is $1.2m$ thick. Its field strength varies from $1.75T$ at the inner radius to $1.5T$ at the outer radius. A schematic view along the beam axis is shown in figure 4.12.

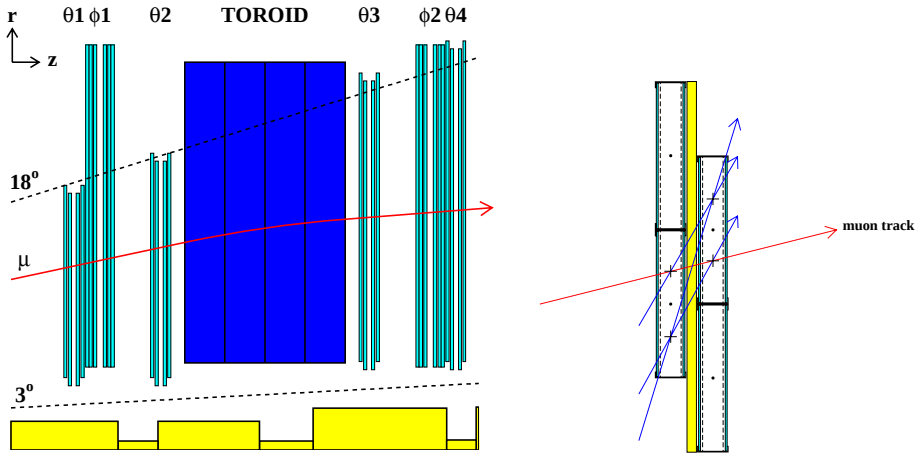

Figure 4.12: $r-z$ *view of* forward muon detector *on the left with an enlargement of the second* θ *double layer on the right illustrating the avoidance of ambiguities by the shifted double layer*

On both sides of the magnet three double layers of drift cells are mounted. In two of the cells mounted on either side of the toroid the wires are strung tangential to the z-axis for the precise determination of the polar angle and one has radial strung wires which measure more accurately the azimuthal angle. All cells in the double layer are shifted by half a cell width to resolve left-right ambiguities.

4.4 Trigger system

The task of the *trigger* system is the steering of the data taking. If some conditions indicating interesting physic events are fulfilled in certain subdetectors the trigger "fires" and initiates readout and processing of the event information. Thereby the trigger electronic constitutes an interface between the high collision rate of $10.4MHz$ on the one hand and a limited band width of $\sim 10Hz$ for the event recording on tape on the other hand. If the trigger rate exceeds the available bandwidth then the data taking system often has to wait for the event processing to be finished. During that time the detector is insensitive for further events in which case *deadtime* accumulates. The design criterium of the trigger system is then to keep as much as possible interesting physics events while not exceeding a fixed rate at the same time. These requirements are met by a multi level trigger system.

The discussion of the trigger system presented in the following is kept comparatively simple. A more detailed description can be found in [25], a study of the muon triggers with main focus of attention on their use for W analysis is also in [28].

4.4.1 Level 1

After the bunch crossing each subdetector sends a subset of digitized information to the central trigger logic. Since the subdetectors need some bunch crossing periods of 96 ns for signal shaping (drift time and integration time of preamplifiers with cables introducing further delays) the system has to cope with information from several consecutive bunch crossings simultaneously. The signals of the different subdetectors are synchronized to the HERA clock such that pieces transmitted separately and at different times can be assigned to the same event later on and stored in a pipeline. After 24 BC or $\approx 2\mu s$ the information from all subdetectors is complete and the first trigger level (L1) decision is evaluated.

The L1 decision is based on the combination of conditions from different subdetectors. Each such condition describes whether a certain threshold was exceeded in the measurement and constitutes one of 192 *trigger elements*. The trigger elements are fed to the trigger logic where they are combined to 128 *subtriggers* according to rules given in the trigger setup. Individual setups with sets of subtrigger conditions can be used for different purposes and running conditions.

Since not every fulfilled subtrigger condition is intended to keep the event (e.g. high rate triggers for very common physics processes, *monitor* triggers which supervise the efficiency of other subtriggers) each individual subtrigger can be *prescaled*. This means that at a prescale factor n, the subtrigger is taken into account for the trigger decision only every n-th time it is set. Due to interactions of the beam particles the beam currents in HERA decrease with time after each fill. The data taking during one fill is called a *luminosity run* which is divided into four phases with rather stable run conditions. Because the trigger rates decrease with the beam currents the rate suppression with prescales can be relaxed during a run. For each phase a different set of prescale factors is applied.

At first for each fulfilled subtrigger condition an associated counter gets

incremented. If one of the counters equals its prescale factor the counter is reset, the filling of the pipelines is stopped and the event gets validated by the next trigger levels. This starts the dead time in which succeeding events are lost since the pipelines are stopped. Otherwise the event is rejected immediately. This process is dead time free.

4.4.2 Level 2

When the first trigger level decides to keep the event for further processing a complete read out of the entire detector information is started. This process depends on the multiplicity of the event and usually takes $1 - 2ms$.

During the readout the second trigger level (L2) decision is evaluated in parallel. The operation of L2 is therefore said to be *synchronous*. The second trigger level performs more complex operations on the information available for L1. It is realized by two separate subsystems, the L2 *topological trigger* (L2TT) and the L2 *neural network* (L2NN) which both supply additional 16 L2 trigger elements. The decision of L2TT is based on topological correlations between different subdetectors, mainly energy clusters in the $\theta - \phi$ plane, and describes the agreement of the event topology with a predefined reference topology. L2NN is a two layer neural network which is trained to recognize specific event signatures for different physics processes, the output represents the significance for the event to belong to one of the trained classes.

For every such value above a programmable threshold an L2 trigger element is set. After a fixed time of $20\mu s$ these trigger elements are used to validate the positive decisions of the first trigger level. If none of them is confirmed the readout is stopped immediately, the event gets rejected and the restarting of the pipelines terminates the dead time of the detector.

4.4.3 Level 3

The third trigger level was foreseen to perform more complex operations on the available data within a few $100\mu s$. A L3 reject would stop the time consuming readout of the full detector information and reduce the input rate for L4. This trigger level has not yet been used.

4.4.4 Level 4

The level four trigger operates on the full event information from all subdetectors. After the read out commences a processor farm performs a partial event reconstruction using the final algorithms of the H1 reconstruction software package *H1REC*. The partially reconstructed event allows for an efficient rejection of remaining typical background from beam-gas and beam-wall interactions which reduces the necessary bandwidth of the storage system by $\approx 80\%$. A small fraction (about 1%) of the events is always kept for monitoring purposes.

Since L4 operates *asynchronous* to the previous trigger levels it does not introduce further dead times as long as the number of submitted events does not exceed a critical rate of $\approx 50Hz$ determined by the available computing power and the complexity of the reconstruction tasks.

The events which passes the level four filtering are then written to *raw data tapes*.

subtrigger	trigger elements
ST15	(Mu_Bar || Mu_ECQ) && DCRPhi_THig && zVtx_sig
ST3	SPCLe_IET > 2 && SPCLe_ToF_E_2
ST56	(SPCLe_IET > 1 || SPCLe_IET_Cen_2) && DCRPhi_Ta && Mu_Any
ST61	(SPCLe_IET > 2 || SPCLe_IET_Cen_3) && DCRPh_THig && zVtx_sig
ST66	Lar_Etmiss > 2 && Lar_IF > 1
ST67	Lar_electron_1
ST71	zVtx_sig && DCRPhi_Tc && Lar_BR
ST77	Lar_Etmiss > 1

Table 4.1: *Trigger elements required by the subtriggers used for the detection for muonic W decays*

4.4.5 Level 5

The fifth and final level of the H1 trigger and data acquisition system performs the complete event reconstruction of the L4 raw data. On L5 H1REC runs in parallel on a dedicated multiprocessor workstation which needs ≈ 1 *cpu s* per event. The processing is done off-line after the data taking. At good terms the entire L4 output data can be reconstructed within a few hours after they have been taken. After the reconstruction the events are classified as candidates for selected physics processes. Events which fall in at least one such physics class are then written to *production output tape* (POT). A subsample of event properties sufficient for most analyses is copied to *data summary tapes* (DST) which are small enough to be stored on disk.

4.5 Subtriggers used for this analysis

For a clean physics sample with well defined trigger efficiency it is necessary to limit the set of used triggers in the analysis. The subtriggers used for the detection of muonic W decays are listed in table 4.1. The table shows the trigger elements required by the applied subtriggers.

Some trigger elements are defined by two bits with three thresholds, "small", "medium" and "high". In the above list "TE > 1" means the requirement of a medium or high threshold and "TE > 2" accepts only the high one.

4.5.1 Triggers elements derived from energy deposits in LAr

Neighboring cells in the liquid argon calorimeter are combined to so called *trigger towers* (TT). Their analog signals are summed up and digitized to form *big towers* (BT). Several thresholds are introduced in this process to suppress electronic noise and background.

For this analysis there are five important trigger elements provided by the LAr trigger.

- **LAr-Etmiss**
  The LAr-Etmiss TE describes the imbalance of transverse momentum

measured in the calorimeter. From the energies measured in the big towers the quantity

$$
\begin{aligned}
P_T^{BT} &= \sqrt{\left(\sum_i P_{x,i}^{BT}\right)^2 + \left(\sum_i P_{y,i}^{BT}\right)^2}, \\
P_{x,i}^{BT} &= E_i^{BT} sin\theta_i^{BT} cos\phi_i^{BT} \\
P_{y,i}^{BT} &= E_i^{BT} sin\theta_i^{BT} sin\phi_i^{BT}
\end{aligned}
$$

is calculated with angles θ_i^{BT} and ϕ_i^{BT} of the known BT positions. Each big tower energy must exceed a threshold which depends on the position in the detector in order to enter the above sum. The two big towers closest to the beam pipe are not included since they are very sensitive to background from beam-gas and beam-wall interactions. In the central barrel the thresholds are relatively high (6 GeV) due to high electronic noise.

The LAr-Etmiss trigger is implemented with three thresholds, 4.5 GeV (low), 6 GeV (medium) and 7.5 GeV (high).

- **LAr-electron**
  LAr-electron is set if the energy in one trigger tower exceeds a certain threshold value. Since the energy of hadronic showers is mostly spread over several trigger towers and an electron in the liquid argon requires $Q^2 \gtrsim 100\ GeV^2$ which limits the rate, a minimum threshold of 6 GeV (for Lar-electron_1) can be used without prescale.

- **LAr-T0**
  LAr-T0 is a timing signal derived from the trigger towers. It indicates whether the signal of the trigger towers is synchronized with the bunch crossing.

- **LAr-IF**
  LAr-IF is set for events with high energy deposits in the IF cells in the forward region near the beam pipe

- **Lar-BigRay**
  The Lar-BigRay TE is provided by the L2 topological trigger. It combines the requirement of energy deposits in the liquid argon with a link to a central track. The trigger element is set if the energy in any one trigger tower exceeds 1 GeV and is matched in azimuthal and polar angle with a *ray* (see below) from the $DCr\phi$ trigger.

4.5.2 Trigger elements of the SpaCal

This analysis uses two *inclusive electron trigger* (IET) trigger elements of the spaghetti calorimeter. For these trigger elements sixteen cells in the electromagnetic section of the SpaCal are summed up to trigger towers which are in dependence of their distance r to the beam pipe divided into the inner (r $<$ 16cm) and outer (r $>$ 16cm) ones. The trigger towers overlap each other such that the entire cluster of an electron is contained within one trigger tower (*sliding window technique*).

A third trigger element combines the total energy in the electromagnetic section of the SpaCal with timing information derived from the analog readout.

- **SPCLe_IET**
  The SPCLe_IET TE is set if the energy in a trigger tower in the outer part of the electromagnetic SpaCal exceeds a fixed threshold. At least 2 GeV are required for SPCLe_IET > 1 and 6 GeV for SPCLe_IET > 2.

- **SPCLe_IET_Cen**
  SPCLe_IET_Cen requires energy in the inner part of the SpaCal. The thresholds are set to 2 GeV energy in a trigger tower for SPCLe_IET_Cen_2 and 6 GeV for SPCLe_IET_Cen_3.

- **SPCLe_ToF_E2**
  SPCLe_ToF_E2 is set if the total energy in the electromagnetic section of the SpaCal exceeds 12 GeV and is synchronized with the nominal bunch crossing time.

4.5.3 Track based trigger elements

- **zVtx-sig1**
  The inner and outer proportional chambers (CIP, COP) of the CJC and the first multi-wire proportional chamber (MWPC) of the FTD are used to form track candidates for a fast determination of the event vertex. Each particle coming from the interaction point passes two double layers of proportional chambers, either in CIP and COP or in CIP and the first MWPC of the forward tracker. The hits in these chambers are then combined to *rays*, straight lines in the rz plane. The z coordinate of the point of intersection with the beam pipe is filled in the *z-vertex histogram*. The rays which were formed from the correct combination of hits produce a significant peak above the combinatorial background which are randomly distributed (see illustration in figure 4.13).

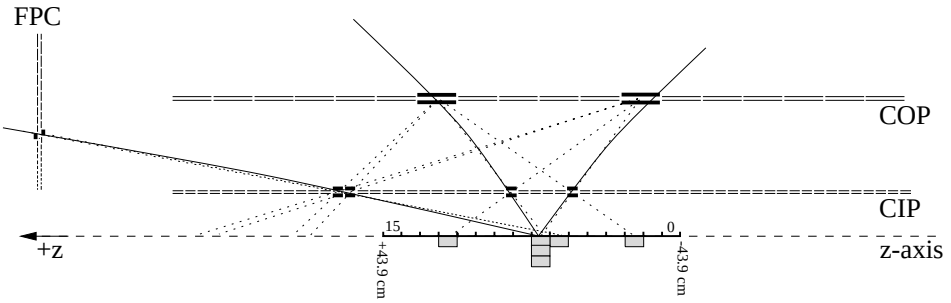

Figure 4.13: *z-vertex histogram*

The trigger element zVtx-sig1 is activated if a significant peak is found,

$$\frac{\left(n_{peak} - \frac{N_{rest}}{15}\right)}{\sqrt{n_{peak}}} > 1.5.$$

with n_{peak} the maximum number of entries in one bin and N_{rest} all the other entries.

- **DCRPhi_Ta**
  This trigger searches for tracks in the CJC which have a *distance of closest approach* of less than 2 cm from the beam axis and are therefore unlikely to originate from beam-wall background. To keep the trigger logic reasonable small only 10 (seven in CJC1 and three in CJC2) out of 56 signal wire layers of the CJC are used for this trigger. The DCRPhi_Ta TE is set if at least one track with a transverse momentum above 420 MeV is found.

- **DCRPhi_Tc**
  DCRPhi_Tc extends the DCRPhi_Ta trigger element by the requirement that at least three tracks with a transverse momentum above 420 MeV have to be found.

- **DCRPhi_THig**
  The DCRPhi_THig TE is determined in the same way as the DCRPhi_Ta TE despite that it uses a higher threshold of 800 MeV.

4.5.4 Trigger elements for muons

Muon specific trigger elements are derived from the limited streamer tubes in the central region and hits in the drift chambers in the forward muon toroid.

The subtriggers used in this analysis are based on muon triggers in the instrumented iron only. Five out of the sixteen limited streamer tubes provide a trigger signal to the central trigger logic. The definition of trigger elements in different regions of the central muon system is shown in picture 4.14.

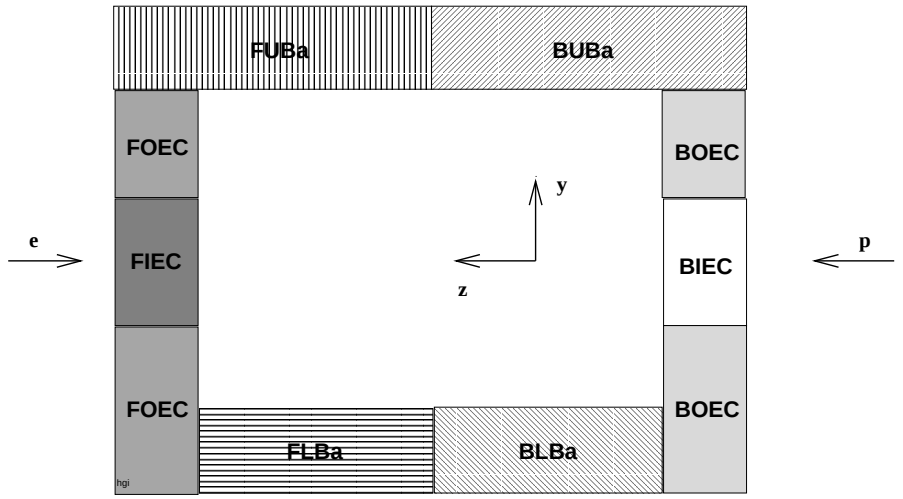

Figure 4.14: *Division of the instrumented iron in trigger sectors*

A trigger element is set if the number of hits in the five layers exceed a fixed number of coincidences. Due to the higher hadronic background, especially in the forward region, the number of required hits increases in the end-caps in

order to achieve a similar trigger rate as in the barrel. The minimum number of required coincidences in the different regions is listed in the following table.

trigger element	minimum number of hits
MU_FIEC	4
MU_FOEC	3
MU_BAR = {FUBa,BUBa,FLBa,BLBa}	2
MU_BOEC	3
MU_BIEC	3

From these trigger elements two logical "or" combinations are derived.

- **Mu_ECQ**
  The trigger element Mu_ECQ is the combination of the trigger elements MU_FOEC || MU_BOEC || MU_BIEC in the end-caps, excluding the high rate inner forward end-cap.

- **Mu_Any**
  Mu_Any is set if any of the five trigger elements in the instrumented iron is active.

4.5.5 P_T^{calo} triggered $W \to \mu\nu$ sample

Events with high energy deposits in the LAr calorimeter are mainly triggered by the set of subtriggers ST66, ST67, ST71, ST77. ST67 is sensitive to compact energy deposits typical for electrons and is mainly used for high Q^2 neutral current analyses. The other subtriggers were developed for the analysis of charged current events. Since the low charged current cross section limits the available event statistics for a precise determination of the trigger efficiency the *pseudo charged current* technique was developed [34] which uses a high statistics neutral current sample. After the neutral current events are triggered by the electron energy deposit in the LAr the electron signal is electronically removed from all subdetectors and the events get indistinguishable from charged current ones.

The trigger efficiency of the combined set is displayed in diagram 4.15 as a function of

$$P_T^{calo} = \sqrt{\left(\sum_i E_i sin\theta_i cos\phi_i\right)^2 + \left(\sum_i E_i sin\theta_i sin\phi_i\right)^2},$$

the transverse component of the vectorial sum over the energy clusters in the liquid argon calorimeter. The efficiency rises at $P_T^{calo} \approx 8\ GeV$ and reaches a plateau value above $P_T^{calo} \approx 16\ GeV$. The trigger efficiency for events with lower P_T^{calo} is increased by additional use of the muon trigger ST15.

For the simulated muonic W decays the trigger efficiency is $\epsilon \approx 85\%$ for an event sample with $P_T^{calo} \geq 12\ GeV$.

4.5.6 Electron triggered $W \to \mu\nu$ sample

Events with an electron in the LAr calorimeter are triggered by the subtrigger ST67. The trigger efficiency is almost 100% (as determined in [24]). Muonic

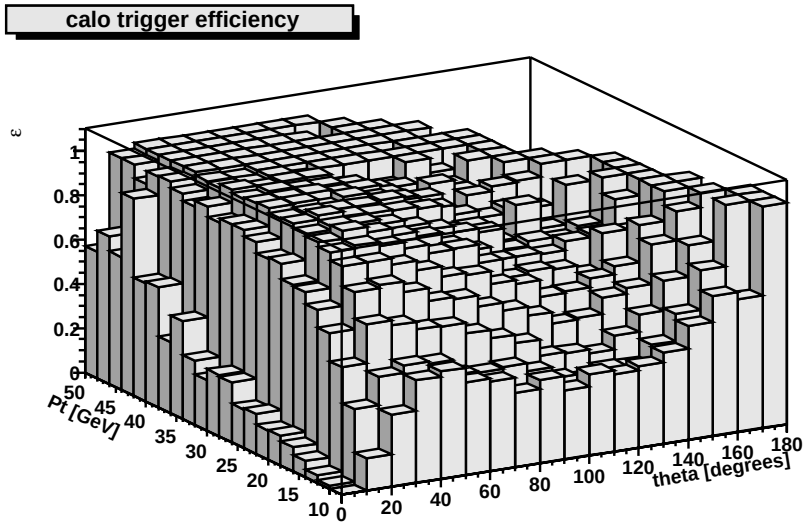

Figure 4.15: *Trigger efficiency of the combined set of LAr triggers ST66,ST67,ST71,ST77 as a function of the calorimetric pt and polar angle*

W decays with an electron in the SpaCal are mainly triggered by ST56. This subtrigger is based on the combination of signals in the central tracking detector and the instrumented iron together with energy in the electromagnetic section of the SpaCal. As for electrons in the liquid argon the trigger efficiency of the SpaCal calorimeter is nearly 100% [33] The trigger efficiency of the DCRPhi_Ta trigger element is determined as a function of polar angle and transverse momentum of the track from neutral current events with one isolated central track which is due to the electron. The efficiency is calculated as the fraction

$$\epsilon_{TE} = \frac{\text{number of events triggered by MT and TE}}{\text{number of events triggered by MT}}$$

with the independent set of *monitor triggers* (MT) ST66, ST67, ST77. In the same way the Mu_Any trigger efficiency was determined from an event sample with high p_T muons and energy deposits in the LAr. It is parameterized by the polar angle of the muon and the number of hits in the instrumented iron.

The efficiency of both components is displayed in figure 4.16.

The combined trigger efficiency of ST67 and ST56 is $\approx 70\%$ for muonic W decays with an electron in the detector and a muon with $p_T \geq 12\ GeV$ in the instrumented iron. The trigger efficiency is increased to $\approx 85\%$ by additional use of the subtriggers ST3 and ST61 which have higher thresholds for the energy in the SpaCal but do not require a muon and the muon trigger ST15. The efficiency gain by the SpaCal subtriggers ST3 and ST61 is determined from Monte Carlo simulation of muonic W decays with an average prescale of roughly 1.2 taken into account for both.

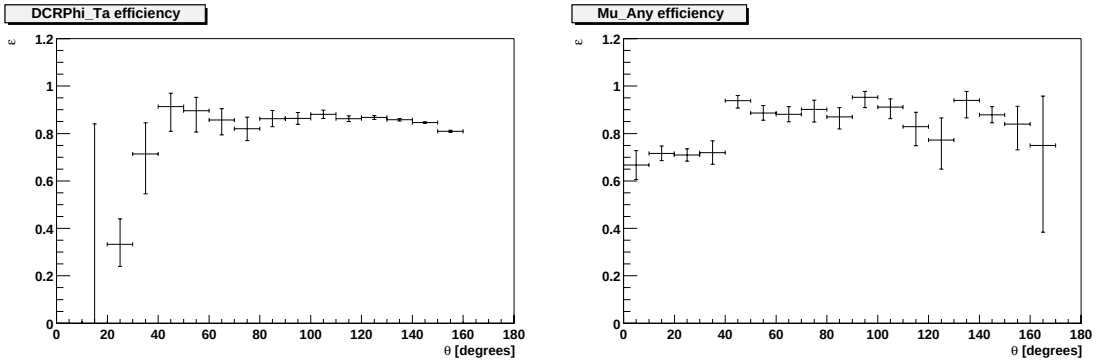

Figure 4.16: *Trigger efficiencies of the DCRPhi_Ta and Mu_Any trigger elements as a function of the polar angle for tracks above 2 GeV transverse momentum and muon candidates with at least six iron hits. The different sized error bars represent the concentration of evaluated events in the backward respective forward region in the monitor sample, between* $120° \leq \theta \leq 140°$ *no muon event activated the monitor trigger*

Chapter 5

$W \rightarrow \mu\nu$ event topology

At HERA W production is a rather rare but spectacular process.

$$e\ p \longrightarrow (e)\ W\ X$$
$$\hookrightarrow \mu\ \nu$$

In most ep events both scattered electron and proton remnant remain undetected. Since an unknown energy fraction is lost in the beam pipe in these cases the use of energy and momentum conservation laws for the event reconstruction is limited. It is usually impossible to fully reconstruct the kinematics.

The geometrical acceptance of the H1 detector, which reaches near to the beam pipe, allows a kinematic reconstruction limited to the transverse plane to be made. Undetected particles are known to leave the detector under very small angles and it is thus usually a good approximation to assume that they do not contribute to the transverse momentum balance of the event. One of the most important event properties in this context are the transverse momenta of the measured particles and this is also the attribute where $W \rightarrow \mu\nu$ events produce a rather unique signal.

The high W mass converts to kinetic energy of the leptons in the decay. One will detect an *isolated* muon (not associated with a jet) with high transverse momentum $p_{T,\mu} \sim \frac{1}{2}M_W$. In case of a neutrino one measures a significant imbalance in the reconstructed transverse momentum of the event,

$$P_{T,miss} = |\sum_{particles} \vec{p}_{T,particle}|$$

the *missing transverse momentum*, of the order $P_{T,miss} \equiv p_{T,\nu} \sim \frac{1}{2}M_W$.

Kinematic distributions of muonic W decays are simulated by the EPVEC Monte Carlo generator, the upper plots of figure 5.1 show the generated transverse momentum distribution of muon and neutrino.

The left lower plot displays the transverse momentum spectrum of the hadronic system X. The trigger condition $P_T^{calo} \geq 12\ GeV$ limits the selection efficiency to about one third. The efficiency is increased by considering also the electron triggered channel. Approximately 25% of W production events are expected to have a scattered electron detected in either the SpaCal or the LAr, the scattering angle is depicted in the right lower plot of figure 5.1.

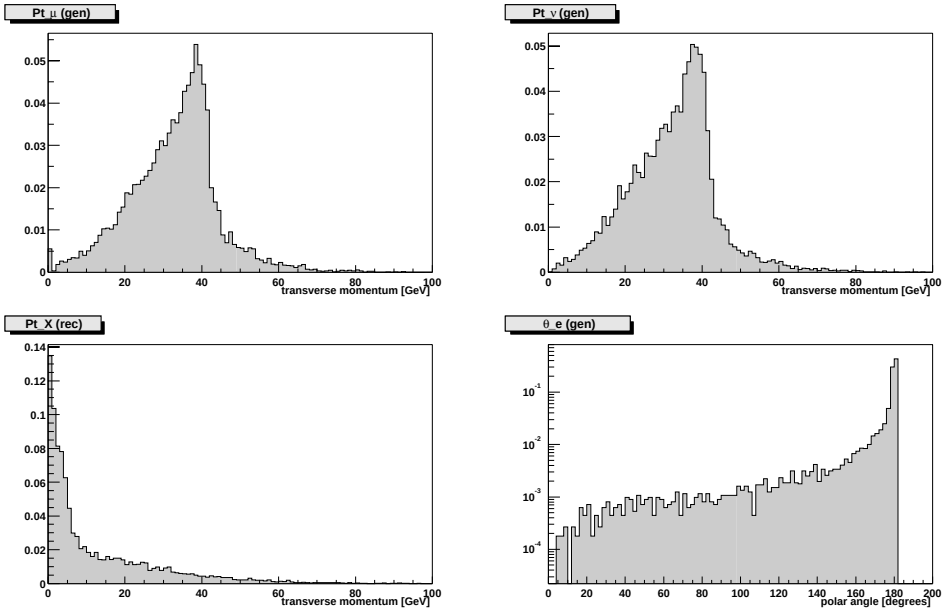

Figure 5.1: *Transverse momentum distributions of muon, neutrino and hadronic system X as expected from Monte Carlo simulation. In the lower right corner the simulated polar angle distribution of the scattered electron is shown. Approximately* 10% *of the events have an electron in the LAr and* $\approx$ 18% *in the SpaCal.*

The topology of the events triggered by the set of subtriggers acting on the energy deposits in the liquid argon calorimeter differs significantly from those triggered by an electron in the detector. These two channels will be therefore treated separately. For comparison with former analyses which investigate only the P_T^{calo} triggered muonic W decays events with an imbalance in the calorimeter and an electron in the detector are first considered for the P_T^{calo} channel. All events which failed the selection for the P_T^{calo} triggered sample are then considered for the electron triggered channel. Thus the latter sample accumulates not only events with $P_T^{calo} \leq 12\ GeV$, but also a small fraction of events which failed one of the other cuts in the former one.

In the following discussion of signal and background event properties a preselected sample will be used defined by either an imbalance in calorimetric energy deposit or an electron in the detector together with an isolated high $p_{T,\mu} \geq 12\ GeV$ muon candidate (with weak muon identification criteria applied based on a typical muon pattern in the forward muon detector, the instrumented iron or the liquid argon calorimeter) and high reconstructed missing momentum $p_{T,miss} \geq 12\ GeV$.

5.1 P_T^{calo} triggered $W \rightarrow \mu\nu$ sample

Events in the P_T^{calo} triggered sample are defined by the requirement of a minimal calorimetric imbalance of $P_T^{calo} \geq 12\ GeV$ for which the set of subtriggers {ST66,ST67,ST71,ST77} is efficient. As will be described in the next chapter this condition is also usefull to distinguish between W decays and other processes. The same threshold was choosen as in the previous analysis.

Since the electron does not have a significant transverse momentum in most of the W production events, the required energy deposit in the calorimeter is mainly due to the hadronic system X. The W recoils against the X system such that muon and neutrino get Lorentz boosted in the opposite direction to X. This results in a "Mercedes-starlike" event topologie in the transverse plane. A typical event of this kind is displayed in figure 5.2.

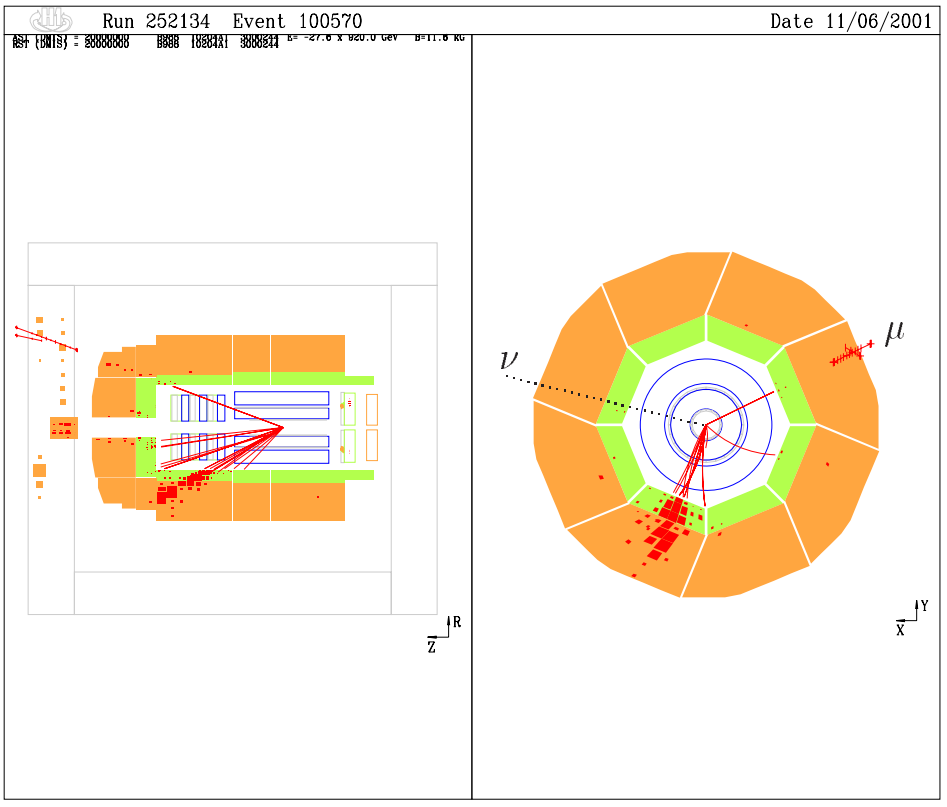

Figure 5.2: *Typical muonic W decay event in P_T^{calo} triggered sample*

5.2 Electron triggered $W \rightarrow \mu\nu$ sample

Events in the electron triggered sample must have an electron in the H1 detector. They are triggered either by subtrigger ST56 for events which have an electron in the SpaCal or by ST67 for higher Q^2 events with an electron in the liquid argon.

Since all events in this channel are required not to be already included in the P_T^{calo} triggered sample, the events considered here have low P_T^{calo} values such that the W gets a small transverse momentum and muon and neutrino are "back-to-back" in $r\phi$. A typical representative for these events is shown in figure 5.3.

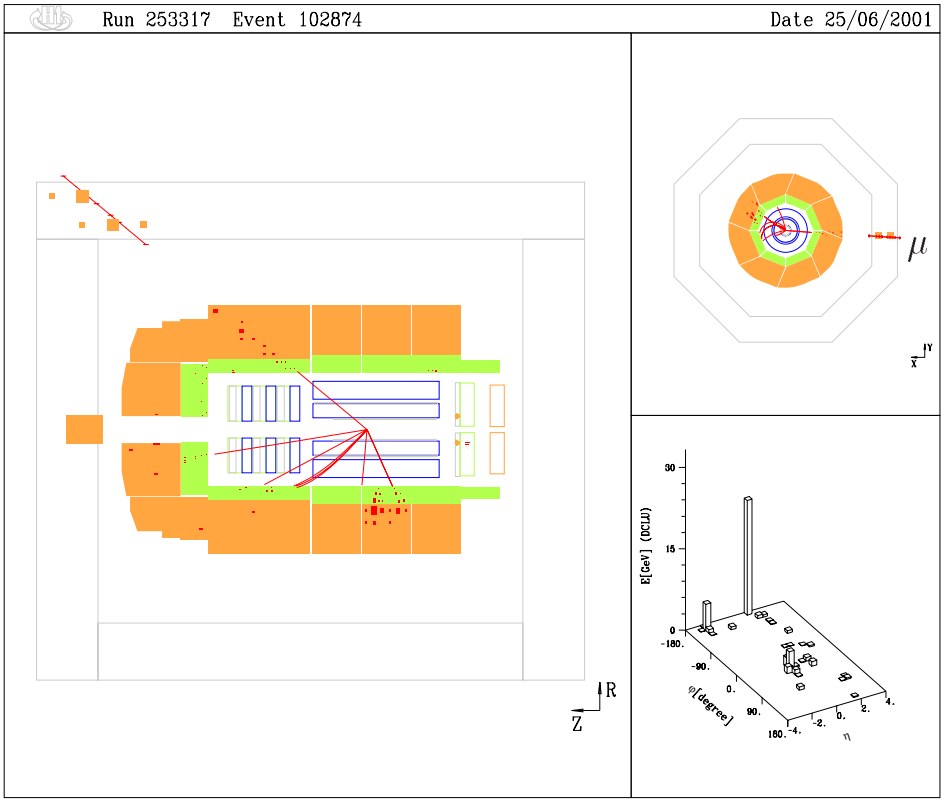

Figure 5.3: *Typical muonic W decay event in electron triggered sample, the scattered electron is in the SpaCal with $\theta_e \approx 172°$*

Chapter 6

Background

On the one hand W production with subsequent muonic decay has a clear experimental signature (as described in the previous chapter). On the other hand various processes with much higher cross sections can contribute to an event sample with muons and missing transverse momentum. For the *background* types discussed in the following the muon candidate typically has hadronic origin (despite events with cosmic muons and *muon pair production*) and the transverse momentum imbalance is due to a missmeasurement (with the exception of *charged current* events).

6.1 Non ep background

6.1.1 Beam-gas and beam-wall interactions

Events with *halo muons* from beam-wall or beam-gas interactions are a frequent process at HERA. Fortunately it is rather easy to get rid of these events. Most of them occur outside the detector and are rejected by the veto walls of the trigger system. The rest usually still has hits in the veto walls but is not rejected when the events happen by chance in the time window around nominal bunch crossings. These muons typically coincide with a simultaneous ep event which triggers such an *overlay event*. The halo muon track is nearly parallel to the beam pipe and clearly does not have an origin near the interaction point.

The H1 collaboration has developed a set of algorithms for non ep background finding [15] which searches for typical patterns in the events and flag them accordingly. In this analysis no such events were found after application of the default set of finders.

6.1.2 Cosmics

Every second some thousand cosmic muons hit the H1 detector. Most of them are not recorded because pure muon triggers have very high prescale factors. Only a small fraction will activate one of the triggers used in this analysis. "Cosmics" typically have one straight track penetrating the entire detector or a muon track opposite an energy cluster in the calorimetric if the cosmic muon "showered". Events with isolated cosmic muons are reliably recognized by standard H1 routines, the cosmic muon finder algorithms in the *Qbgfmar* package [15].

More difficult to reject are overlap events of a cosmic muon with an ep reaction. An example of such an event is shown in picture 6.1.

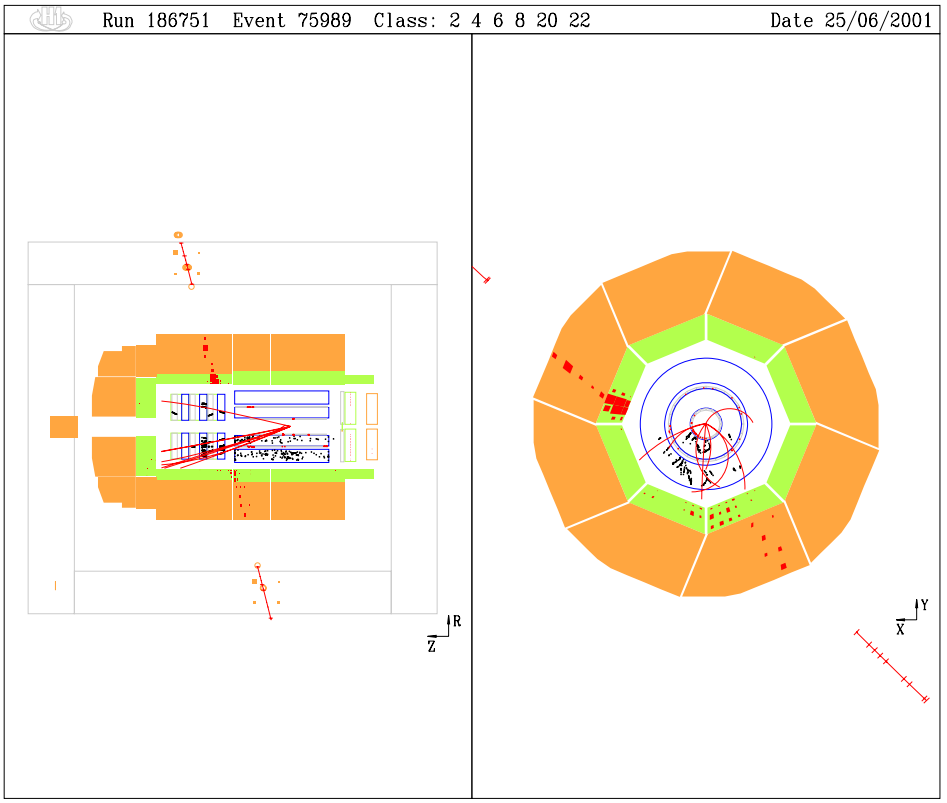

Figure 6.1: *Typical cosmic muon event found in the H1 data*

Events like the one shown with hits opposite in $r\phi$ in the instrumented iron are still recognized by the cosmic muon finders used for this analysis. Cosmic muons can only contribute to the event sample if the muon showers in the detector or escapes through a hole in the geometrical acceptance so that it does not produce two opposite iron signals.

One cannot exclude a contribution of cosmic muons completely but the probability to have unrecognized cosmics in the event sample selected in this analysis is small.

6.2 Jet photoproduction (γp)

The Feynman graph describing the dominant contribution to photoproduction at HERA is shown in figure 6.2

In these processes the gluon or photon fluctuates in a quark-antiquark pair which then *hadronizes* to two jets in the detector. Both jets can be produced with rather high transverse momenta. Since electron and proton remnant are

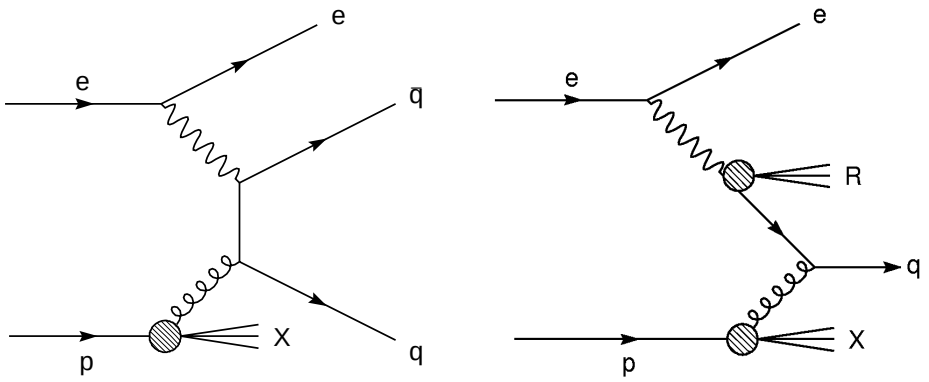

Figure 6.2: *Leading order Feynman diagrams for photoproduction, in the left for the direct and in the right for the resolved process*

scattered only marginally the jets typically balance each other in $r\phi$ showing a "back to back" topology.

If a high energetic hadron does not loose all its energy in the calorimeter and reaches the instrumented iron it can fake a muon signal. In this scenario it is then likely that the total transverse momentum of the event gets badly reconstructed and the event can enter the P_T^{calo} triggered sample.

Events of this kind are simulated by *Pythia* [36].

6.2.1 Photoproduction of light quarks

A typical example for a simulated photoproduction event in the P_T^{calo} triggered sample is shown in figure 6.3.

In this event one of the light quarks probably hadronized to a single meson which decayed to a muon and a neutrino.

6.2.2 Photoproduction of $b\bar{b}$ and $c\bar{c}$ pairs

The production rate of the heavy quarks types $c\bar{c}$ and $b\bar{b}$ is more than an order of magnitude lower than for the light $\{u\bar{u}$,$d\bar{d}$ and $s\bar{s}\}$ quarks. On the other hand b and c quarks can decay to muons which nets an enriched sample in the selection.

By requirering the muon candidate to be isolated many of the muons from c and b decay are rejected and the heavy quark contribution becomes much smaller than the photoproduction of light quarks.

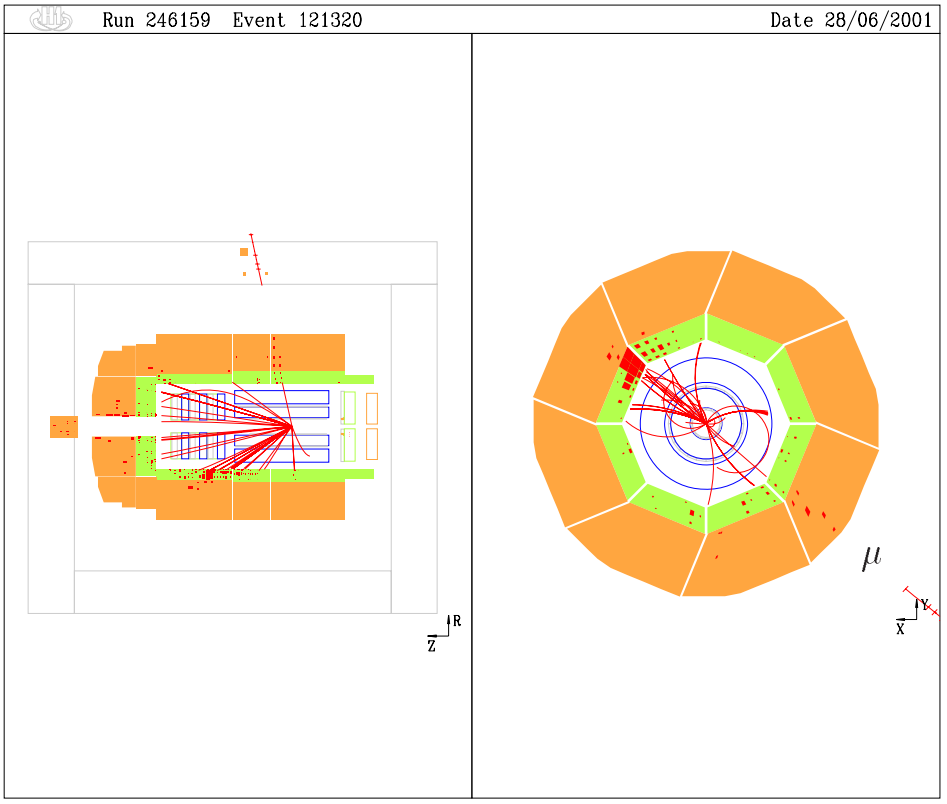

Figure 6.3: *Photoproduction event selected for the* P_T^{calo} *triggered channel*

6.3 Low Q^2 scattering

These events are in the transition region from photoproduction to *deep inelastic scattering*. Both direct and resolved processes can occur in low Q^2 scattering.

From the scattering kinematics of a direct process, using the *Jaquet - Blondel method*,

$$Q^2 = \frac{p_{t,had}}{1-y}, 0 \leq y \leq 1. \tag{6.1}$$

the momentum transfer of the electron is too low to produce a high transverse momentum hadronic system originating from the scattered quark. Because the tracking detectors tend to underestimate but not to overestimate low transverse momenta the direct processes are unlikely to enter the sample with a high transverse momentum muon candidate.

Resolved photon events can produce an experimental signature similar to photoproduction events, but at lower cross section. Therefore in the P_T^{calo} triggered sample the photoproduction contribution is expected to be much higher.

With Q^2 high enough to have the electron scattered in the SpaCal and still a relatively large cross section these events dominate the background in the electron triggered $W \rightarrow \mu\nu$ sample.

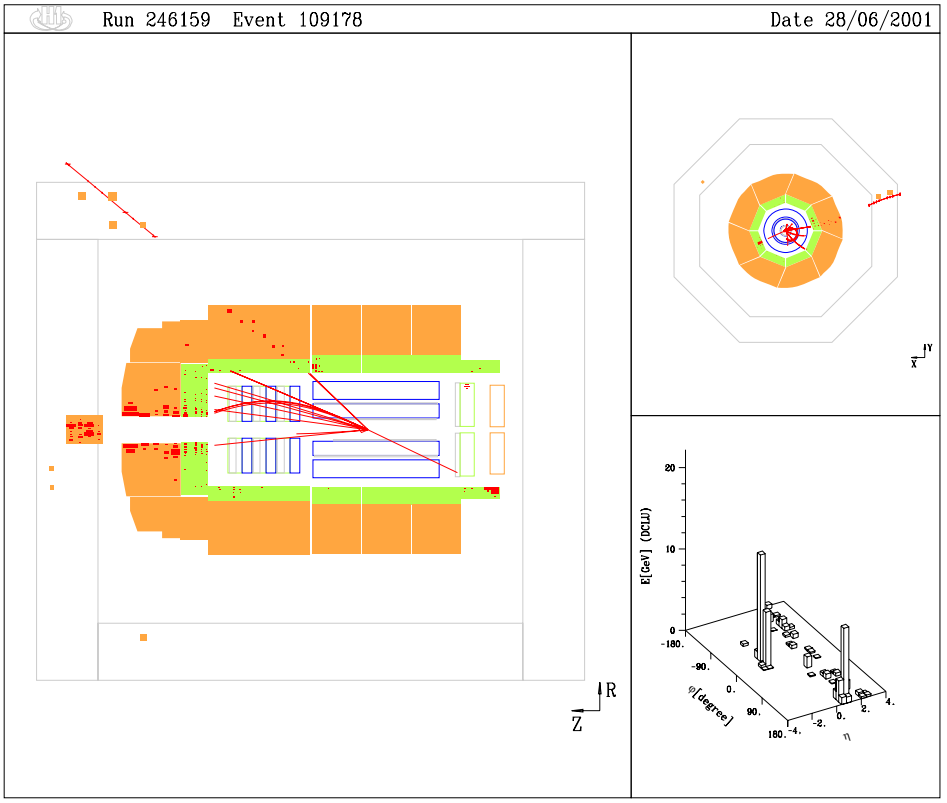

Figure 6.4: *Low Q^2 event selected for the electron triggered channel*

In picture 6.4 one typical such event is displayed.
Low Q^2 events are simulated by the *RapGap* Monte Carlo generator [26].

6.4 Deep inelastic scattering (DIS)

In the higher Q^2 regime only direct processes happen. The events can contribute to the sample if an isolated hadron or meson in the jet formed from the scattered quark produces a muon signal in the instrumented iron.

Since in deep inelastic scattering only two particles, quark and lepton, are involved in the primary interaction the events look relatively simple. There is usually one concentrated hadronic system which balances the scattered lepton in the transverse plane. The muon candidate usually lines up in the $r\phi$ plane with the direction given by lepton and jet.

Deep inelastic neutral and charged current scattering is simulated by the *Django* Monte Carlo generator [11].

6.4.1 Neutral current (NC) events

In high Q^2 neutral current events the scattered electron and quark generally have higher transverse momenta according to equation 6.1. In these events the reconstructed missing P_T often only amounts to a relatively small transverse momentum fraction of the electron and hadronic system. The electron usually still lines up in $r-\phi$ and balances the hadronic system as for events without a reconstructed missing P_T. The mismeasured P_T can be due to electron energy lost in the uninstrumented intersection region between different calorimeter modules. The shower pattern of electrons in the cracks may also significantly deviate from the expectation such that the electron gets misidentified as a hadron and its energy wrongly reweighted. Isolated high energetic hadrons penetrating the calorimeter, reaching the instrumented iron and faking a muon signal there are as well likely to cause high missing transverse momenta.

One simulated typical event of this kind is shown in picture 6.5.

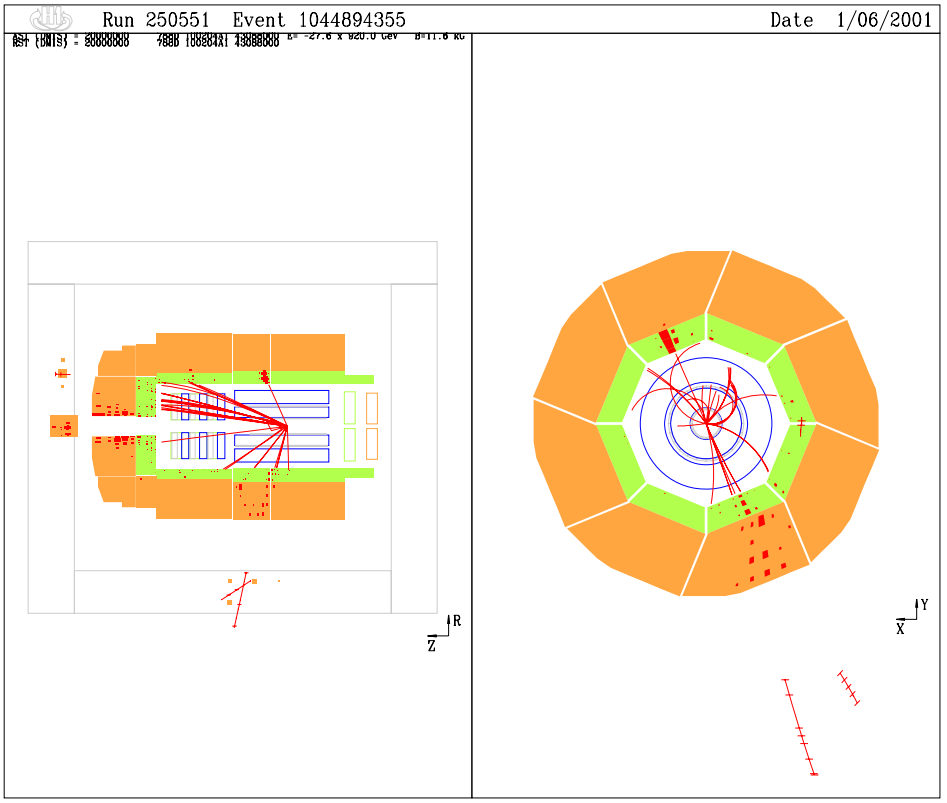

Figure 6.5: *Typical neutral current event*

Since the electron does not vanish down the beam pipe in these events and the energy missmeasurement which leads to the missing P_T often only amounts to a small fraction of the total energy the reconstructed event $\Sigma E - P_z$ is generally near twice the electron beam energy.

6.4.2 Charged current (CC) events

The charged current process is supressed by the lower cross section but generates events with high missing transverse momenta and a P_T^{calo} spectrum which also extends to high values.

6.5 Lepton pairproduction

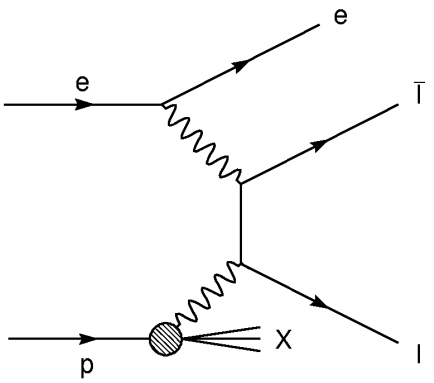

Figure 6.6: *Lepton pairproduction Feynman diagram*

The production of lepton pair events is similar to the photoproduction process despite that instead of a gluon a photon must be exchanged by the proton. Since this requires an electromagnetic instead of a strong interaction the cross section is much smaller.

Lepton pairproduction is simulated by the *LPair* Monte Carlo generator ([9] with description of matrix element calculation in [38]).

6.5.1 Muon pairproduction

The muon pairproduction background gets the dominant one after applying harsh muon identification criteria (see section *muon identification*). Although the cross section is the smallest of all contributing backgrounds this background is one of the hardest to get rid of in end. Clearly one will require the events to show only one isolated muon candidate, but this background still contributes with events showing only one isolated muon while the other one being inside a jet (unlikely) or going down the beam pipe (likely).

One typical event of this kind is shown from the Monte Carlo sample in event display 6.7.

The missing transverse momentum of these events mainly arises from mismeasured track momentum of the one visible muon whereas the one which goes down the beam pipe does not contribute much to the imbalance in transverse momentum. Therefore the missing P_t usually is parallel (or anti-parallel) with the isolated muon in the $r - \phi$ plane.

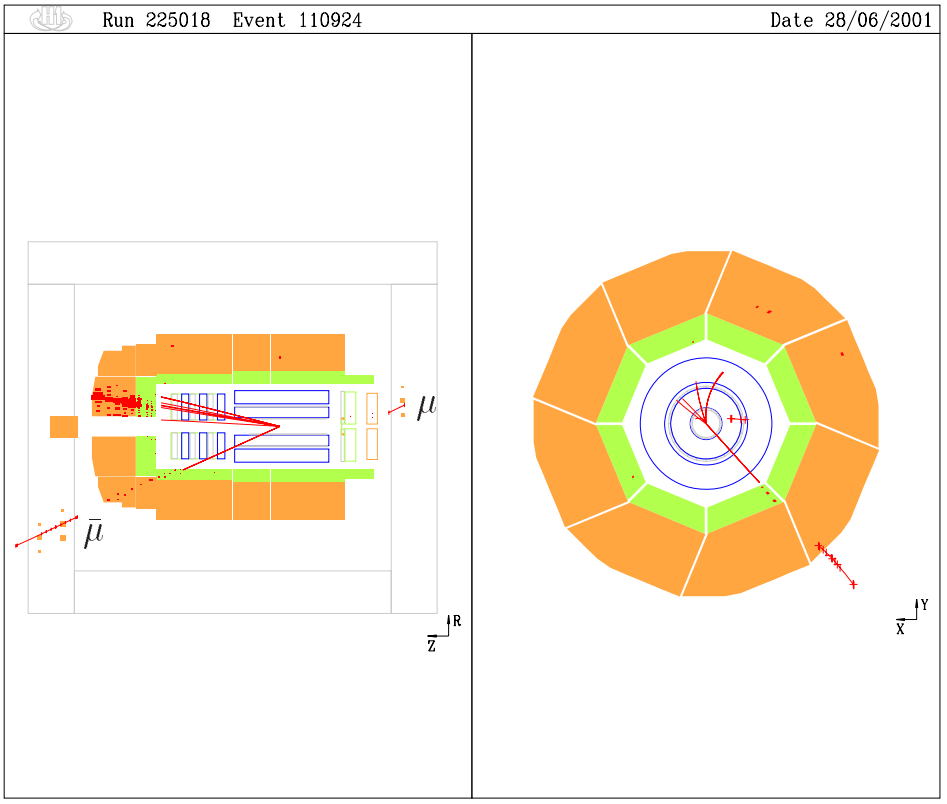

Figure 6.7: *Muon pairproduction event fulfilling cut requirements, second muon lost in backward region*

6.5.2 Tau pairproduction

The contribution of the tau pairproduction background is generally of the same order of magnitude as the muon pairproduction one. Although the branching ratio of muonic tau decays is less than 20%, the veto against events with two isolated muons does not work for semileptonic tau decays, so that in the end the muon and tau pairproduction background contributions become comparable.

Chapter 7

Particle identification and reconstruction

7.1 Electron identification

An electron candidate is identified by the presence of a compact and isolated cluster of energy in the electromagnetic sections of the liquid argon or spaghetti calorimeter. A set of *estimator* variables is defined which describe the shower shape. These are evaluated by different algorithms in the *QESCAT* package [12] for electron finding. In this analysis the default H1 electron identification implemented in QESCAT is used for electron candidates in the LAr calorimeter whereas for electron candidates in the SpaCal a more sophisticated identification is required to reject background with an electron-like signal in the backward region.

Since electromagnetic clusters are more compact than hadronic ones a more stringent bound is put on the cluster radius and no significant energy not associated with the electron cluster is required in the SpaCal. These conditions are described by the estimators

- **Ecra**
  radius of the electron cluster (calculated as described in [18])
- **Ebk**
  energy in the electromagnetic section of the SpaCal not associated with the electron cluster
- **Ehsk**
  energy in the hadronic SpaCal section
- **Eveto**
  energy in the innermost part of the SpaCal which defines a *veto layer* against non-ep background near the beam pipe

In this analysis the four-vector of the electron is reconstructed from the calorimeter information alone, the energy from the cluster energy and the polar and azimuthal angles from the position of the cluster center. Although no track

property	name	value
LAr electrons		
DCA cluster-track	Etra	< 12cm
SpaCal electrons		
DCA cluster-track	Etra	< 2.5cm
cluster radius	Ecra	< 5cm
energy not associated with electron	Ebk + 2 Ehsk	< 0.5 GeV
energy in veto layer	Eveto	< 1 GeV

Table 7.1: *Electron identification requirements, the variable names are defined in the H1 lotus code [23], they are only quoted here to help H1 members familiar with the code to identify them. Energy not associated with the electron cluster is counted twice in the hadronic section*

information is used for the determination of the electron four-vector a cluster-track link is always required to reject neutral pions, photons and noise. The *distance of closest approach* (DCA) between the extrapolated track and the cluster in the calorimeter can be smaller for SpaCal electrons than for ones in the LAr since the backward drift is mounted directly in front of the SpaCal.

The electron identification requirements are summarized in table 7.1.

7.2 Reconstruction of the hadronic final state

The hadronic final state is reconstructed from the information in the liquid argon and spaghetti calorimeters and the central tracking detector,

$$p_h = p_{LAr} + p_{SpaCal} - p_{noise} + p_{CTD}\,,$$

where p_{noise} subtracts the contribution of calorimeter cells attributed to electronic noise [35].

The combination of the calorimeter and track information is done by the *FSCOMB* algorithm (described in [4]). Since the momentum resolution of the central tracking detector is superior to the calorimeter for low momentum particles, for transverse momenta below some threshold (which is taken to be 2 GeV) the particle momentum reconstruction is based on the track measurement. To avoid double counting each track is extrapolated to the calorimeter and the energy in a cylinder with radius $25cm$ in the electromagnetic and $50cm$ in the hadronic section is assigned to the track. If the measured track momentum exceeds the energy in the calorimeter the track momentum is taken and the calorimeter energy is excluded from further processing. If otherwise the energy in the cylinder is higher the calorimeter information is used and the track neglected. Hadrons and mesons with transverse momenta above the 2 GeV threshold are always reconstructed from the calorimetric measurement alone with their tracks excluded from further processing.

On top of the FSCOMB algorithm operates the *jet-finder* which searches for associations of hadronic particles. Each isolated cluster is assumed to originate from a single primary quark or gluon which then hadronized in the detector. The sum over all reconstructed particle momenta in the cluster defines a *jet*, the

equivalent to the four-vector of the primary quark or gluon. For the jet finding a *longitudinally invariant k_t clustering algorithm* [6] (implemented using the KTCLUS package [10]) is used with a minimum of $p_{T,jet} > 5\ GeV$ required for a jet.

For events where the jet-finder does not succeed to find at least one jet it is convenient to define the *inclusive hadronic angle*

$$\gamma_h = 2\ arctan\left(\frac{\Sigma_h}{P_{t,h}}\right)$$

with

$$\begin{aligned}\Sigma_h &= \sum_i (E_i - p_{z,i}) \\ P_{t,h} &= \sqrt{\left(\sum_i p_{x,i}\right)^2 + \left(\sum_i p_{y,i}\right)^2}\end{aligned}$$

summed over all particles in the detector apart from electrons and muons and take it as an estimate for the polar angle θ of the hadronic system. This definition has the advantage to be more independent from the proton remnant (which usually contributes with low P_t) than simply taking

$$\begin{aligned}\theta &= arctan\left(\frac{P_{t,h}}{P_{z,h}}\right) \\ P_{z,h} &= \sqrt{\left(\sum_i p_{z,i}\right)^2} \\ p_{z,i} &= E_i cos\theta_i\end{aligned}$$

directly.

7.3 Muon identification

As already mentioned in the discussion on backgrounds, the cross section for photoproduction and inelastic scattering processes exceed the cross section of lepton pairproduction and W production by some orders of magnitude. Therefore an effective muon selection is needed to discriminate between real muons and *fake* muons, which mean hadronic particles faking a muon-like pattern in the detector.

The standard H1 muon identification procedure distinguishes between muon candidates observed in the central detector and ones measured in the forward muon toroid. The detection of *central muons* is based on a linking of an inner track from the drift chambers with an energy deposit typical for a muon in the liquid argon calorimeter or hits in the instrumented iron. *Forward muons* are formed from a track in the forward muon toroid alone without the need of a link to a track in the central detector.

To the sample of muon candidates obtained from this procedure hadronic particles can contribute in the following ways [30]:

- **In-flight decay**
  Both pions and kaons, the hadronic particles most frequently produced at Hera, decay dominantly into muons after $c\tau \approx 5m$. The probability of an unstable particle to decay within some distance is given by the exponential

  $$P(x) = 1 - e^{-\frac{x}{\beta\gamma c\tau}} \tag{7.1}$$

  (with β the particles velocity in units of c and γ it's ratio of energy and mass). Thus the probability for such a particle to decay decreases with higher momentum and is therefore small compared to the other contributions in the $p_{t,\mu} > 12\ GeV$ sample this analysis examines.

- **Sail through**
  Hadrons can pass the calorimeter without any interaction with the probability

  $$P(x) = e^{-\frac{x}{\lambda}}$$

  where x is the traversed distance and *lambda* the hadrons interaction length. The depth of the calorimeter in hadronic interaction lengths as a function of the polar angle was shown in figure 4.7.

  The sail through is the dominating source for the misidentification of hadrons as muons.

- **Punch through**
  Sometimes traversing hadrons pass some distance without energy loss before they start interacting in the calorimeter or simply have a too high energy so that they do not loose all their energy within the given interaction lengths. In these cases the hadrons are likely to cause hits in the first few layers of the instrumented iron.

The *fake muons* usually appear close to other hadrons in a jet, whereas the *real muons* are uncorrelated with any hadronic system. It is therefore convenient to require the muon candidates to be isolated. For this purpose one defines the two criteria

- D_{track}
  defined as the minimum of $\sqrt{(\eta_\mu - \eta_{track_i})^2 + (\phi_\mu - \phi_{track_i})^2}$ with *pseudorapidity* η calculated according to $\eta = ln\frac{\theta}{2}$ for all "good" tracks i (fulfilling the Lee West track selection requirements [39]).

- D_{jet}
  defined as the minimum of $\sqrt{(\eta_\mu - \eta_{jet_i})^2 + (\phi_\mu - \phi_{jet_i})^2}$ for all jets found by the jet-finder and for the entire hadronic system.

7.3.1 LAr signal

In comparison with electrons and hadrons muons usually deposit small energies when traversing the calorimeter. Due to their high mass muons do not emit much *Bremsstrahlung* like electrons nor due they interact strongly with the atoms in the traversed material like hadrons. High energetic muons only loose a

fraction of their energy when they ionize atoms in the traversed material. The mean energy loss due to excitation and ionisation of charged particles passing through matter is given as a function of the momentum of the incident particles by the *Bethe-Bloch equation* 7.2,

$$-\frac{dE}{dx} = 4\pi N_A r_e^2 m_e c^2 z^2 \frac{Z}{A}\frac{1}{\beta^2}\left(ln\left(\frac{2m_e c^2\gamma^2\beta^2}{I}\right) - \beta^2 - \frac{\delta}{2}\right) \qquad (7.2)$$

with z charge of the incident particle in units of the elementary charge, Z charge and A mass number of the traversed material and I a specific ionisation constant of the absorber which can be approximated by $I \approx 16Z^{0.9}eV$ for $Z > 1$. The parameter δ is another material dependent constant which cannot be described in general but is tabulated.

The energy loss described by equation 7.2 is meant *on-average*, an individual particle can differ from this average. Statistical fluctuations of the energy loss for particles with a fixed momentum are described by a *Landau distribution* with mean given by (7.2). Usually the fluctuation around the mean is relatively small, because ionizing particles generally cause many ionisations each with a small energy transfer so that the influence of individual collisions average out, but higher deviations are possible (the Landau distribution is known for its "long tail").

Because of the β factors in the *Bethe-Bloch* formula the (mean) energy loss depends on the particles mass and momentum. The momentum dependent energy loss due to ionisation is displayed in picture 7.1 for muons in iron.

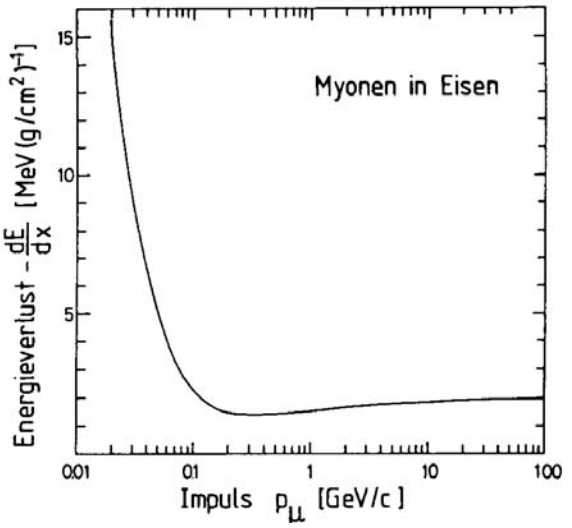

Figure 7.1: *Mean energy loss due to excitation and ionisation for muons in iron as a function of the muon momentum [20]*

For muons with energies above some hundred MeV the energy loss is near its minimum. These muons are therefore called *minimum ionizing particles*.

Within the depth of the LAr calorimeter a total energy deposit between two and four GeV is expected for muons.

7.3.2 Iron signal

The ten iron plates in the return yoke of the H1 detector yield an effective shielding for the streamer tubes inbetween of roughly one hadronic interaction length each.

That means that only a fraction of $\sim e^{-10} < 10^{-4}$ of hadrons penetrating the liquid argon calorimeter to the muon system is expected to reach the last layer of instrumented iron.

The distribution of the last layer with an iron hit is shown in diagram 7.2 for a muonic and hadronic sample.

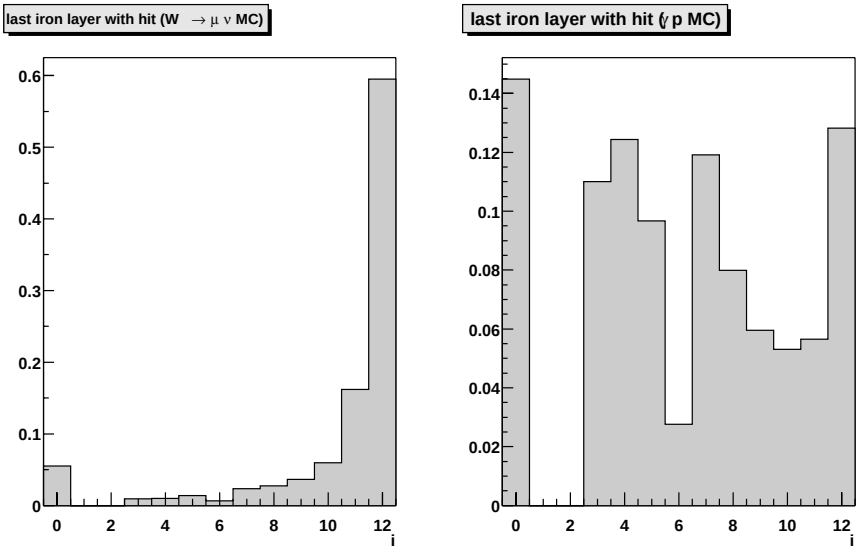

Figure 7.2: *Distribution of last layer with hit in instrumented iron for muon candidates found in simulated muonic W decay (left) and photoproduction (right), a value of zero means the particle does not have any iron hits*

The distribution of the hadronic sample does not fall steeply exponentially as expected from the above discussion because of the real muon component in the sample originating from in-flight-decay of pions and kaons.

It indeed does not make a big difference if one uses the last layer with an iron hit (distribution shown in figure 7.2) or the total number of iron hits (displayed in figure 7.6) to suppress hadronic background in the central muon sample.

Hadronic background is far less dominating in the forward muon sample although more hadrons are scattered in the forward region. The reason for this is that the iron toroidal magnet in the forward muon system itself is nearly twice as many interaction lengths thick as the instrumented iron which surrounds the liquid argon calorimeter and that forward muon candidates must have significantly higher energy than central muon candidates with the same p_t (simply

because of the small angle and $E = \frac{p_t}{sin\theta}$ for $m \ll E$). The probability for *in-flight-decay* is then significantly smaller according to equation 7.1.

7.3.3 Selection of muon candidates

The muon finder used in this analysis is optimized for maximum efficiency and gives flexibility through offering multiple hypothesis for one and the same muon candidate. So one has to decide how to handle multiple hypothesis usually arising when a muon gets detected in the overlap of the acceptance regions of forward tracker and forward muon system around 20°.

A *forward muon* and a *central muon* are assumed to belong to the same physical muon if they differ in $\sqrt{(\eta_{fwd} - \eta_{cen})^2 + (\phi_{fwd} - \phi_{cen})^2}$ by no more than 0.1.

Because of the better resolution the track information of the forward muon system is used in preference of that from the forward tracking detector.

Forward muons

From the hit pattern in the forward muon toroid tracks are formed. Depending on the number of hits before and after the toroidal iron yoke the tracks are classified into five different grades describing the reliability of the momentum measurement and the muon identification. For this analysis forward muon candidates are required to have hits on both sides of the toroid linked together to a good track (grade one or two).

Histograms 7.3 show the distribution of track qualities in the forward muon toroid for real and fake muons.

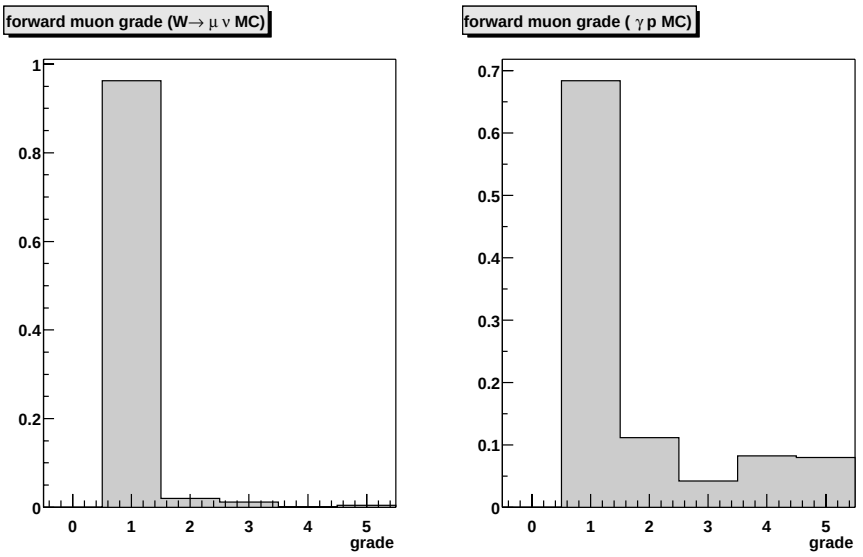

Figure 7.3: *Distribution of track qualities in the forward muon toroid (outside the main H1 detector) for muon candidates found in simulated muonic W decay (left) and photoproduction (right)*

Because the forward muons loose on average 3 GeV kinetic energy when traversing the liquid argon calorimeter and the forward iron end-cap before reaching the forward muon toroid and being measured, 3 GeV are added to their measured energy to correct this effect.

Central muons

The decision whether to accept a central muon candidate relies on a set of different variables, the ones used for this analysis are listed in the following summary with names as defined by the muon finder in the H1 lotus code [23]

- **track quantities**
  - **mutrqu**
    Quality of the forward, central or combined track associated with the muon candidate as defined by Lee West. Good tracks are assigned an *mutrqu* value of one. Tracks not passing the track selection are assigned either a value of two if they can be fitted to the primary event vertex or three otherwise. At H1 vertex fitted tracks are conveniently called $DTRA$ tracks and non-vertex fitted tracks $DTNV$ tracks.
- **calorimeter quantities**
  - **Nmuin**
    Number of clusters (isolated energy deposits) in the liquid argon calorimeter inside a cylinder of radius $25cm$ in the electromagnetic and $50cm$ in the hadronic section
  - **Emuin**
    Energy deposit around the extrapolated track in a cylinder of radius $25cm$ in the electromagnetic and $50cm$ in the hadronic part of the LAr calorimeter.
  - **Ewzm**
    Mean depth of energy deposit in the calorimeter, calculated from the cluster centers and energies as $\frac{\sum_i E_i \; r_i}{\sum_i E_i}$
- **iron quantities**
  - **Trmui**
    Theta angle of the *iron track* reconstructed from the hit pattern in the limited streamer tubes
  - **Trmuci**
    Theta angle reconstructed from the hit pattern in the tail catcher
  - **nlaymu**
    Number of limited streamer tube layers with a hit associated with the muon candidate
  - **Ilay0**
    Iron layer with the innermost hit, this quantity will be referred to as "first layer with hit".

- **Ilay1**
  Iron layer with the outermost hit, this quantity will be referred to as "last layer with hit".
- **Rhomu**
  Distance of closest approach (DCA) of the extrapolated muon track in the instrumented iron to the primary event vertex
- **z0mu**
  Distance along the beam pipe between extrapolated iron track and the primary event vertex (muon track z coordinate taken at the point of closest approach to the vertex in $r - \phi$)

According to the values of the above muon properties the muon candidates get classified into different grades which are summarized in table 7.2.

In figure 7.4 the distribution of the above muon grades (as defined in table 7.2) is shown for muons from W decay and those in a photoproduction sample. The displayed histograms are taken from Monte Carlo simulations and are filled with muon candidates having a transverse momentum of at least 12 GeV and fulfilling a $D_{jet} > 0.5$ and $D_{track} > 0.5$ isolation requirement.

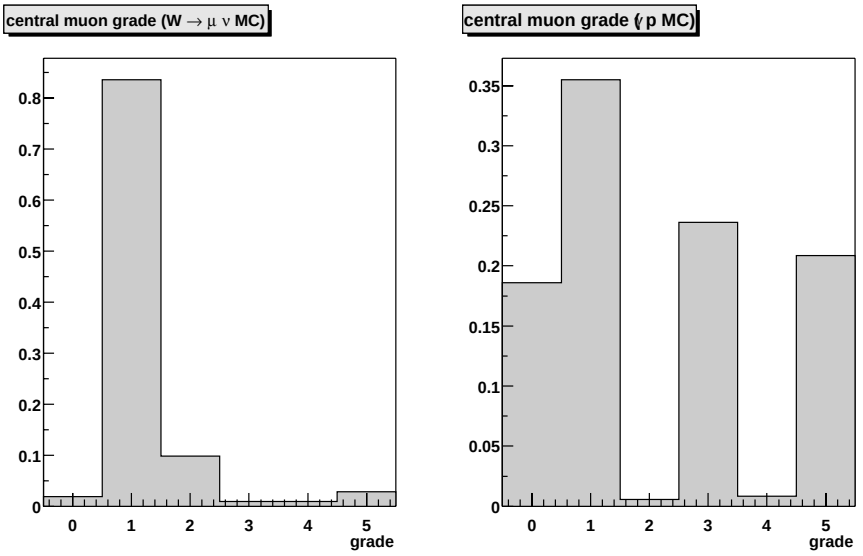

Figure 7.4: *Distribution of muon grades calculated according to the definition in table 7.2 for muon candidates found in simulated muonic W decay (left) and photoproduction (right), a grade of zero means a muon candidate fails the requirements of all grades*

Most real muons have an iron track formed from either hits in the limited streamer tubes or the tail catcher (corresponding to grade one and two) while most fake muons have not.

The contribution of grade two muons is mainly coming from edges between different modules in the instrumented iron. Since the tail catcher measures influence charge it is sensitive also for charged particles passing near by but

lotus grade	property	name	value
0	bad muon signal quality || near forward muon		
	iron muons		
1	θ from track	Thmu	> 0.01 (has track)
	Lee West track quality	mutrqu	1 (good)
	distance (in η - ϕ space) between central track and iron	Trmui	< 0.5 ($\Delta\phi = 28.7°$)
	DCA of muon to vertex	Rhomu	< 100cm
	z0 of muon to vertex	z0mu	< 100cm
	hits in intrumented iron	nlaymu	≥ 2
	first hit in iron layer	Ilay0	≤ 5
2	θ from track	Thmu	> 0.01 (has track)
	Lee West track quality	mutrqu	1 (good)
	distance (in η - ϕ space) between central track and iron or TC	Trmui < 0.5 || Trmuci < 0.5	
	long. depth of calo energy deposit	Ewzm	$> 75cm$
	number of calo cluster	Nmuin	≥ 1
	energy in small cylinder around track	Emuin	< 10 GeV
	fraction of calo/track energy	Emuin/Emu	< 0.2
3	θ from track	Thmu	> 0.01 (has track)
	Lee West track quality	mutrqu	1 (good)
	distance (in η - ϕ space) between central track and iron or TC	Trmui < 0.5 || Trmuci < 0.5	
	calorimeter muon		
4	θ from track	Thmu	> 0.01 (has track)
	Lee West track quality	mutrqu	1 (good)
	energy in small cylinder around track	Emuin	< 10 GeV
	number of calo cluster	Nmuin	≥ 1
	long. depth of calo energy deposit	Ewzm	$> 75cm$
	muon candidate formed from clustered iron hits		
5	DCA of muon to vertex	Rhomu	< 100cm
	z0 of muon to vertex	z0mu	< 100cm
	hits in instrumented iron	nlaymu	≥ 2
	first hit in iron layer	Ilay0	≤ 5

Table 7.2: *Requirements for assignment of grades to muon candidates in lotus code*

not going through a limited streamer tube. This is illustrated in the picture 7.5, where the angular distribution of both muon grades is shown. The white areas in the plot correspond to the holes in the geometrical acceptance of the instrumented iron mentioned in the detector section.

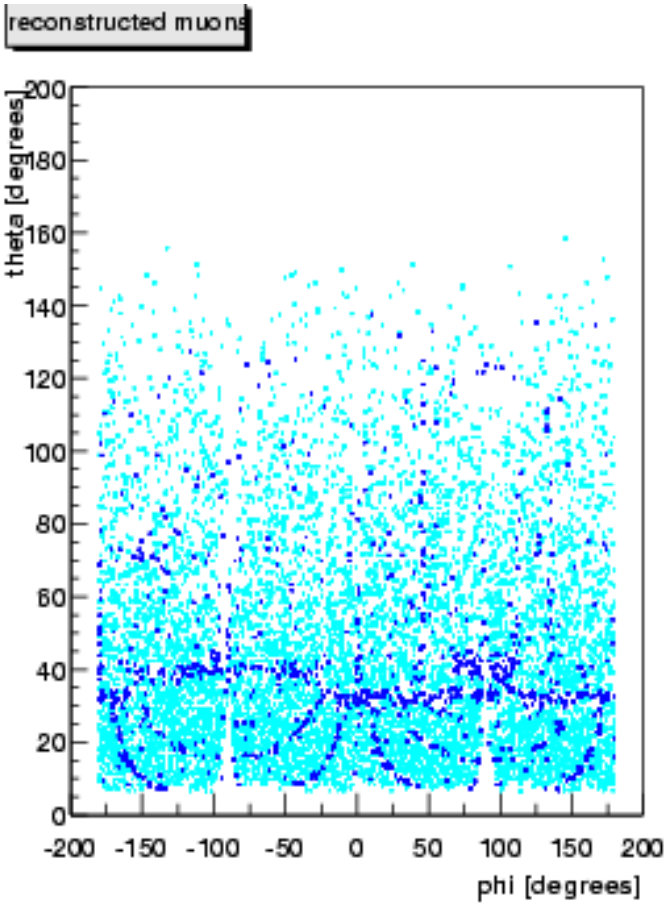

Figure 7.5: *Angular distribution of muon grades, each point corresponds to one simulated muon reconstructed with the appropriate grade, grade one muons are drawn in blue(darker) grade two ones marked red(lighter)*

In diagram 7.6 the distribution of the number of iron hits is shown for simulated muons from W decay (left) and in a photoproduction sample (right). For this analysis a minimum of three iron layers is required. If additional rejection of fake muon background is needed one can simply increase the required minimum number of iron hits of up to six without too much loss of efficiency.

The selection of real muons can be further improved by cutting on the deposited energy in the liquid argon calorimeter around the muon track. While the total energy deposit of muons as minimum ionizing particles is expected to be rather low between two and four GeV, muon candidates associated with hadronic systems typically have higher values due to contributions of nearby hadrons.

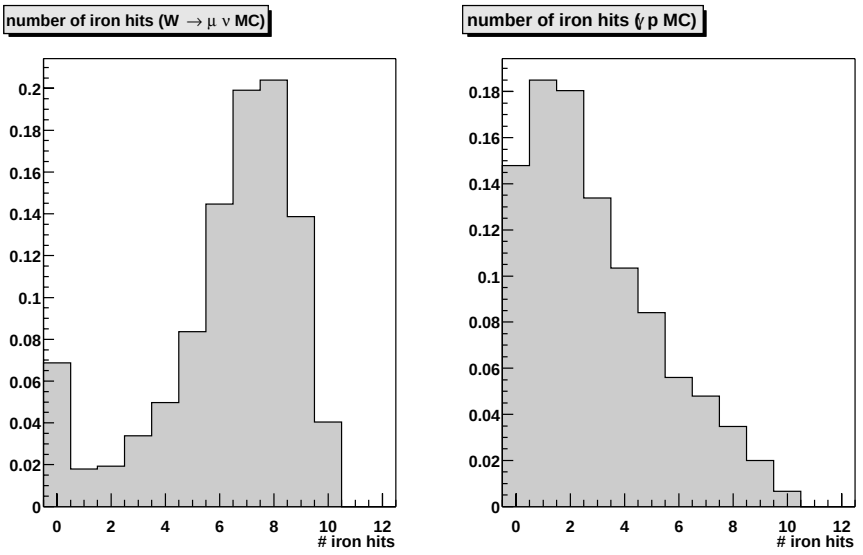

Figure 7.6: *Distribution of the number of hits in the instrumented iron yoke of the H1 detector for muon candidates found in simulated muonic W decay (left) and photoproduction (right)*

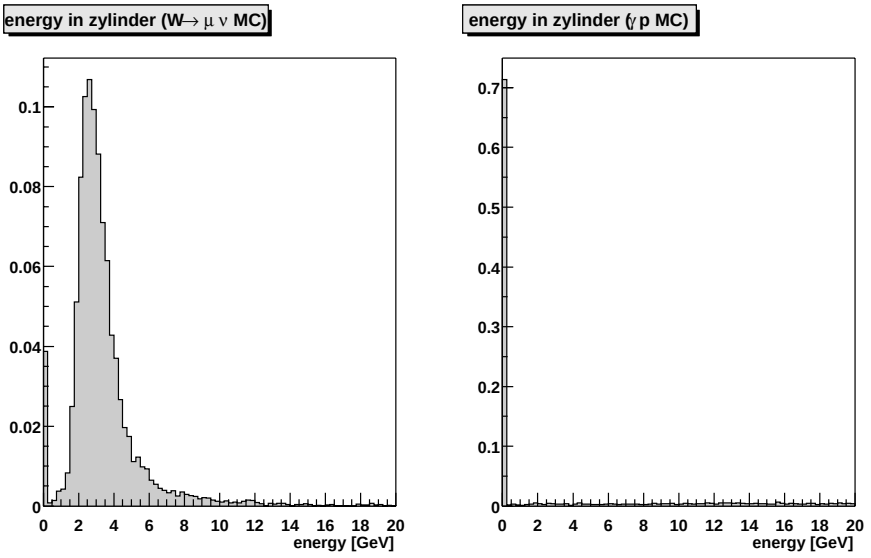

Figure 7.7: *Distribution of the energy deposit in the liquid argon calorimeter inside a cylinder of radius 25cm in the electromagnetic and 50cm in the hadronic section of the LAr for muon candidates found in simulated muonic W decay (left) and photoproduction (right)*

property		name	value
forward muons			
track quality in toroid		Iqfmu	$1 \parallel 2$
energy in small cylinder around track		Efmuin	$\leq 8\ GeV$
central muons			
lotus grade (as defined in table 7.2)		grmu	$1 \parallel 2$
for grade one only	hits in intrumented iron	nlaymu	≥ 6
	layer with last hit	ilay1	≥ 10
energy in small cylinder around track		Emuin	$\leq 8\ GeV$

Table 7.3: *Final muon requirements*

Diagram 7.7 show the distributions of the calorimetric energy deposit for a sample isolated muons with at least 12 GeV transverse momentum for a Monte Carlo simulation of W decay and photoproduction. Real muons exhibit a Landau distribution with a a relatively narrow peak and a mean value compatible with the expectation from Bethe-Bloch (equation 7.2 and diagram 7.1), whereas muon candidates in the hadronic sample are widely distributed with a large fraction not having any energy deposit at all.

In disagreement to the above shown Monte Carlo simulation in reality the liquid argon calorimeter sometimes misidentifies low energy deposits as noise. This effect was noticed in J/Ψ studies for roughly 15% of the muon events and would reduce the muon selection efficiency obtained from the simulation by the same amount. Therefore no minimum energy deposit (neither energy above threshold nor at least one calorimeter cluster associated with the muon) is required for muons in this analysis. Muons are said to be compatible with an isolated minimum ionizing particle pattern if they have an energy deposit below 8 GeV in a cylinder around their track.

The final requirements for the acceptance of a muon candidate are summarized in table 7.3.

With these cuts on the characteristic muon properties one can get rid of the majority of background alone without using any further kinematic cuts.

7.4 Neutrino reconstruction

The neutrino four-vector gets reconstructed by using the conservation laws for transversal and longitudinal momentum, that is the neutrino four-vector is assumed be the *missing momentum* of the event.

Since beam electron and proton enter the detector along the z-axis with no initial transverse momentum component, the *transverse momentum balance* reads

$$\begin{aligned} 0 &= \sum_i p_{x,i} + p_{x,\nu} \\ 0 &= \sum_i p_{y,i} + p_{y,\nu} \end{aligned}$$

where the sum extends over all visible particles in the detector.

From these individual components the *missing transverse momentum* $p_{t,miss}$ of the event is calculated as

$$p_{t,\nu} \equiv p_{t,miss} = \sqrt{\left(\sum_i p_{x,i}\right)^2 + \left(\sum_i p_{y,i}\right)^2}$$

Although the beam electron and proton remnant are usually scattered by such a tiny angle that they leave the detector undetected carrying away a lot of energy, both contribute only marginally to the transverse momentum balance. Therefore the transverse components of the neutrino momentum are well defined regardless how many particles are gone down the beam pipe undetected.

Another variable which is quite independent of the invisible momentum of the proton remnant is the $\sum E - p_z$ of the event having an initial value of twice the electron beam energy,

$$2 \cdot E_e \quad \geq \quad \sum_i E_i - p_{z,i} + E_\nu - p_{z,\nu} \tag{7.3}$$

where the sum extends again over all particles observed in the detector. For the $\sum E - p_z$ balance one must distinguish between events with a visible electron scattered into the detector volume and events where the electron is scattered by such a small angle that it is gone down the beam pipe. Equality in the equation 7.3 holds in good approximation if the electron is in the detector otherwise the right side is smaller by twice the energy of the scattered electron. Therefore the reconstruction of the event $\sum E - p_z$ can only be done completely for events where the electron finder has found an electron candidate.

In these events the hypothesis of a (nearly) massless neutrino yields the last equation,

$$0 \quad = \quad {E_\nu}^2 - \left({p_{x,\nu}}^2 + {p_{y,\nu}}^2 + {p_{z,\nu}}^2\right)$$

necessary to obtain the entire neutrino four-vector. The events are then said to be fully reconstructed.

In the above sums enter the reconstructed particle energies and momenta and not detector level objects like calorimeter clusters and tracks. It does indeed not matter whether one measures the particles with a tracking detector or with a calorimeter, one only has to combine them correctly and be cautious not to count things twice. As described in previous sections the electron and jet finders used in this analysis take care of *double counting* themselves and one has to deal with this issue mere for (isolated) particles not identified as electrons. Muons have their four-momentum determined by the forward and central tracking detectors while depositing some energy in the liquid argon calorimeter. In this case their track momentum enters the momentum balance and the energy inside a cylinder around their track (defined in the same way as used for the muon candidate selection) is subtracted from the total energy in the LAr which is attributed to the hadronic system.

Chapter 8

Event selection

From the $W \to \mu\nu$ event topology discussed in chapter five one will require an isolated high p_t muon, missing transverse momentum and either a significant imbalance in the calorimeter or an electron in the detector for a candidate event.

After application of the improved muon identification described in the previous chapter the expectation for the signal to background ratio is still below one. Therefore additional cuts are necessary on variables introduced in the following.

The distributions shown for these variables are plotted for an event sample with an isolated high $p_{t,\mu} > 12\ GeV$ muon (of grade one or two), at least $p_{t,\nu} > 12\ GeV$ missing momentum and either $P_T^{calo} > 12\ GeV$ or an electron in the detector.

8.1 $\sum E - p_z$ balance

Related to the neutrino is the $\sum E - p_z$ (im)balance of the event, sometimes also referred to as the *missing longitudinal momentum* (although one still needs the masslessness hypothesis to determine the complete four-vector of missing momentum).

The distribution of the event $\sum E - p_z$ is shown in figure 8.1 for signal and background Monte Carlo events fulfilling the selection requirements of the P_T^{calo} triggered sample. Because in most W events the scattered beam electron vanishes down the beam pipe and the decay neutrino is often emit ed in forward direction due to the Lorentz boost along the proton direction, the signal is not well separated from the background. In the figure also the limited resolution for the measurement of particle momenta which enter the $\sum E - p_z$ balance becomes visible in the fraction of events with an $\sum E - p_z$ above twice the electron beam energy.

The $\sum E - p_z$ balance is more useful for the background rejection of the electron triggered sample . The distribution of the event $\sum E - p_z$ is shown in figure 8.2.

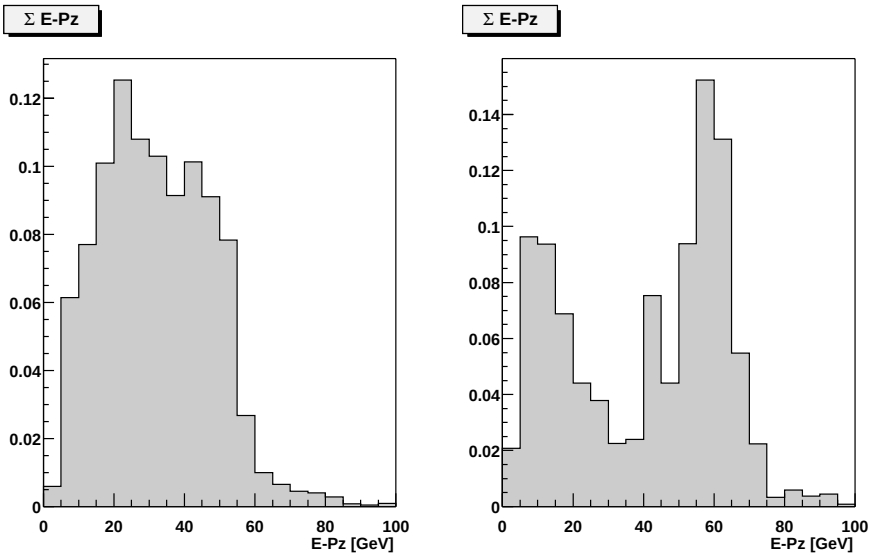

Figure 8.1: $\Sigma E - P_z$ *distribution of Monte Carlo events fulfilling the* $P_T^{calo} > 12\ GeV$ *requirement for signal and background, please excuse the "spiky" distribution for background which is due to limited Monte Carlo statistics and hence high weights for some individual events*

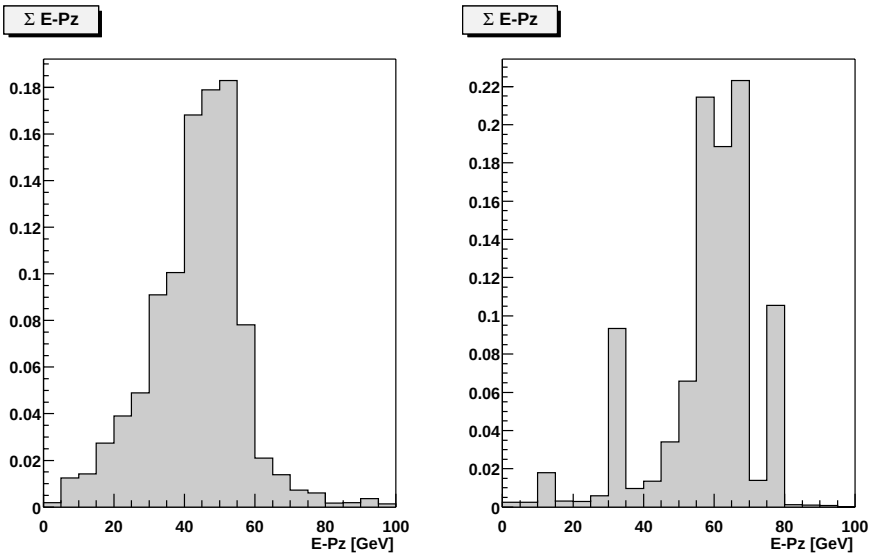

Figure 8.2: $\Sigma E - P_z$ *distribution of signal and background Monte Carlo events with an electron in the SpaCal*

8.2 V_{ap}/V_p ratio

The V_{ap}/V_p variable describes the transverse imbalance of calorimetric energy deposits. It is defined by

$$\begin{aligned} \vec{v_i} &= E_i sin\theta_i cos\phi_i \ \hat{e_x} + E_i sin\theta_i sin\phi_i \ \hat{e_y} \\ \vec{V} &= \sum_i \vec{v_i} \\ V_p &= |\sum_{\substack{i \\ \vec{v_i}\cdot\vec{V}>0}} \vec{v_i}| \\ V_{ap} &= |\sum_{\substack{i \\ \vec{v_i}\cdot\vec{V}<0}} \vec{v_i}| \end{aligned}$$

where the sums extends over all clusters i in the liquid argon calorimeter.

The variable was originally developed for a charged current analysis [32]. In both CC and W decay analyses the majority of background has no intrinsic neutrino and the missing momentum is faked by a missmeasurement.

Most of these background events have a rather balanced transverse momentum distribution, the missing p_t typically occurs in neutral current and photoproduction events with high transverse momenta where the missing p_t amounts to a relatively small fraction of the total transverse momentum.

In [32] it has been shown that the $V_{ap}/V_p \lesssim 0.15$ cut has a higher background rejection power for CC analysis than the previously used $\frac{p_t^{had}}{E_t^{had}} > 0.7$ requirement.

For muonic W decays in the P_T^{calo} triggered sample the W typically recoils against a jet which produces the required calorimetric energy deposit. In this sample the neutrino gets Lorentz boosted in the W direction and is therefore predominantly emitted opposite to the jet whereas the muon does not cause a high energy deposit in the calorimeter (and is also predominantly emitted opposite to the jet). Therefore one expects low V_{ap}/V_p values for this sample.

In the data set one high P_T^{calo} event gets exclusively rejected by this cut. This event has a calculated $V_{ap}/V_p = 0.34$ near the chosen cut value of 0.3 and is shown in picture 8.3.

The distribution of the V_{ap}/V_p variable is shown for a simulated P_T^{calo} triggered $W \to \mu\nu$ sample and the sum of standard model background in picture 8.4.

Events in the electron triggered $W \to \mu\nu$ sample generally have higher V_{ap}/V_p values. The overall calorimetric transverse momentum of these events is usually small and a significant contribution to the overall calorimetric energy deposit of the events is due to the muon. The V_{ap}/V_p variable is therefore not very useful for this sample.

8.3 $p_{t,\nu}^{\perp}$ variable

Due to the recoil of the W in most events in the P_T^{calo} triggered $W \to \mu\nu$ sample the decay particles μ and ν are not in a *back to back* configuration

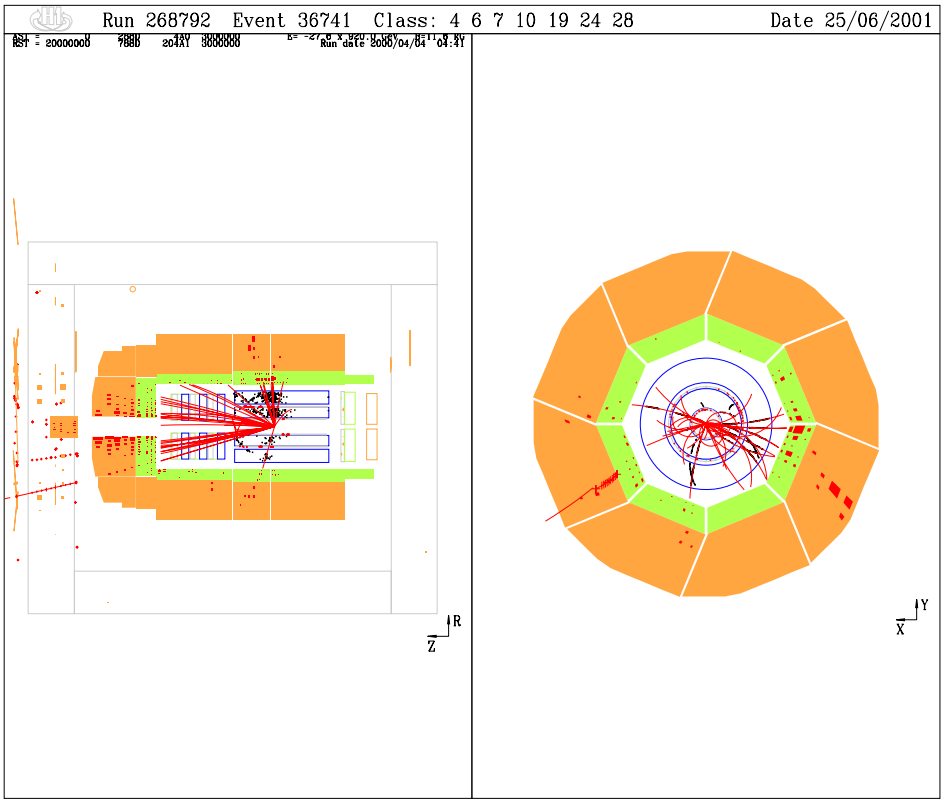

Figure 8.3: *Event exclusively rejected by the* $\frac{V_{ap}}{V_p}$ *cut, the calculated* $\frac{V_{ap}}{V_p}$ *of this events is close to the cut value.*

in the laboratory frame. From the Lorentz boost which generally acts non parallel to the neutrino momentum the neutrino gets a momentum component perpendicular to the muon in $r-\phi$ space. So,

$$\begin{aligned} p_{t,\nu}^{\perp} &= \frac{\vec{p_{t,\nu}} \times \vec{p_{t,\mu}}}{p_{t,\mu}} \\ &= \frac{p_{x,\mu}p_{y,\nu} - p_{y,\mu}p_{x,\nu}}{p_{t,\mu}}. \end{aligned} \tag{8.1}$$

will be in the order of some GeV. The distribution of $p_{t,\nu}^{\perp}$ is shown in picture 8.5 for simulated $W \to \mu\nu$ events and the total standard model background.

A threshold condition on $p_{t,\nu}^{\perp}$ acts as a kinematic cut on the signal while suppressing most background events where the missing p_t is due to a miss-measurement. In most events of the dominating remaining background to the $W \to \mu\nu$ sample, neutral current and inelastic muon pairproduction, the vector of missing transverse momentum is aligned in $r\phi$ space with the muon trajectory. In the case of neutral current events a hadronic system is misidentified as a muon which in combination with an underestimation or overestimation of the particles momentum by the tracking detectors fakes a neutrino signal. In the

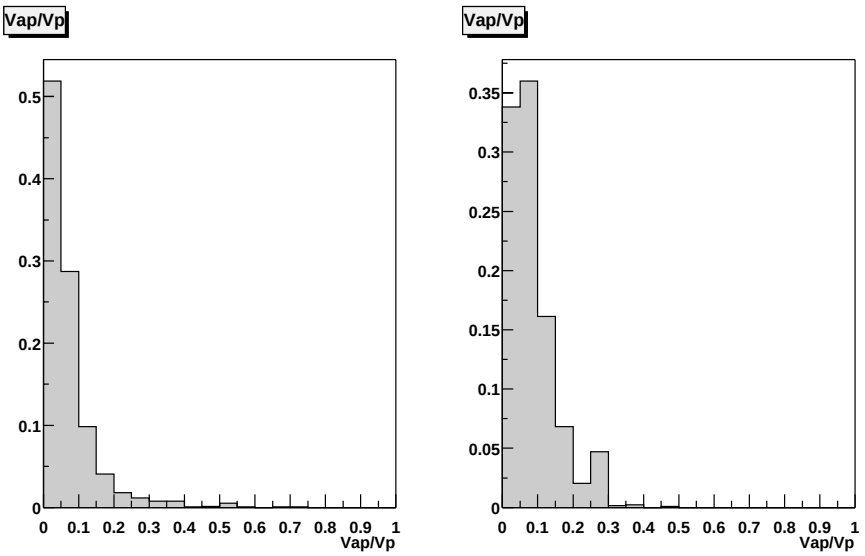

Figure 8.4: *V_{ap}/V_p distribution of Monte Carlo events fulfilling the $P_T^{calo} > 12\ GeV$ requirement for signal and background*

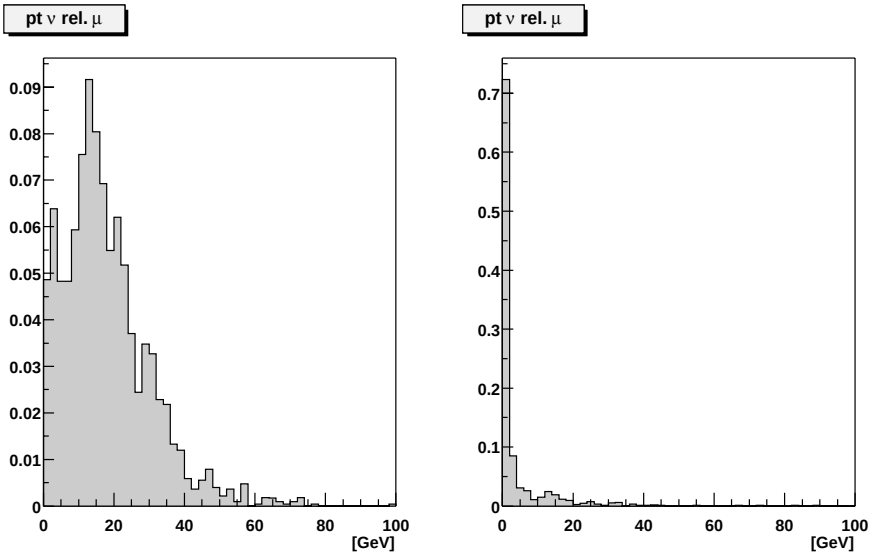

Figure 8.5: *$p_{t,\nu}^{\perp}$ distribution of Monte Carlo events fulfilling the $P_T^{calo} > 12\ GeV$ requirement for signal and background*

case of muon pairproduction one muon typically leaves the detector undetected under small angles. Although this muon does not have a high transverse momentum and does not significantly affect the imbalance, it makes the events passing the two muon veto condition (which will be discussed hereafter). If the other muon track then becomes mismeasured in addition the muon pairproduction event looks much like a W decay.

The topologies of the tree kinds of events is once again graphically illustrated in picture 8.6.

In tau pairproduction background events one tau decays to a muon and the other one to one or more hadrons. The relatively low tau mass does not allow for high momentum components of the neutrinos produced in the decay process relative to the muon and jet.

8.4 No electron in ϕ-crack

The effectiveness of the $p_{t,\nu}^{\perp}$ requirement depends on the assumption that the missmeasurement of high p_t tracks is dominating the error in the reconstruction of the missing transverse momentum. It is therefore necessary to ensure that no other circumstances could add further contributions to the transverse missing momentum and spoil the alignment of the muon and missing momentum vectors in $r - \phi$ space.

This analysis therefore rejects events with an electron candidate inside a $\pm 2^{\circ}$ wedge around a ϕ-crack.

8.5 Two muon veto

To suppress the contribution from muon pairproduction background in the remaining sample events with two isolated muon candidates are rejected. This requirement lowers the efficiency by less then one percent.

One event in the high P_T^{calo} data is exclusively rejected by the two muon veto which is compatible with the expectation of 0.25 exclusively rejected muon pairproduction events from Monte Carlo simulation.

8.6 Final cuts

For the discussed cut variables different sets of threshold values are defined for the selection of muonic W decay candidate events in the P_T^{calo} and electron triggered sample. In the P_T^{calo} triggered sample much of the background is already rejection by the $P_T^{calo} \geq 12\ GeV$ trigger condition itself such that the other requirements do not have to be very harsh. In the electron triggered sample the background level is generally higher, with the dominant contribution from low Q^2 deep inelastic scattering events.

8.6.1 Selection of P_T^{calo} triggered $W \to \mu\nu$ events

The requirements for the selection of muonic W decays in the P_T^{calo} triggered channel is shown in table 8.1.

Figure 8.6: *Graphical illustration of usefulness of* $p_{t,\nu}^{\perp}$

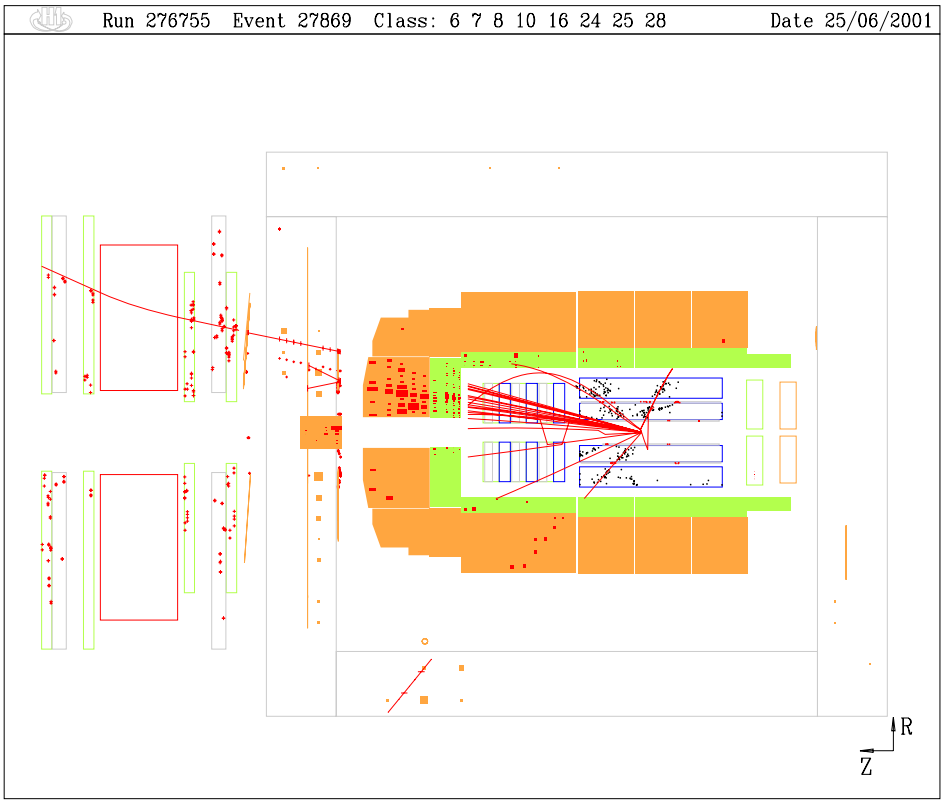

Figure 8.7: *Muon pairproduction candidate event rejected by the two muon veto*

Selection of P_T^{calo} triggered $W \to \mu\nu$ events		
cut		value
trigger	P_T^{calo}	$\geq 12\ GeV$
muon	$p_{t,\mu}$	$\geq 12\ GeV$
neutrino	$p_{t,\nu}$	$\geq 12\ GeV$
	$p_{t,\nu}^{\perp}$	$\geq 6\ GeV$
event selection	V_{ap}/V_p	≤ 0.3
	$\Sigma E - P_z$	$\leq 0.9 \cdot 2\ E_{beam}(e)$
		if electron in LAr || SpaCal
		no electron in phi crack
	number of isolated muons	1

Table 8.1: *Final cuts for P_T^{calo} triggered $W \to \mu\nu$ sample*

Selection of electron triggered $W \to \mu\nu$ events		
cut		value
trigger		electron in LAr || SpaCal
muon	$p_{t,\mu}$	$\geq 12\ GeV$
neutrino	$p_{t,\nu}$	$\geq 18\ GeV$
event selection	$\Sigma E - P_z$	$\leq 0.9 \cdot 2\ E_{beam}(e)$
		no electron in phi crack
	number of isolated muons	1

Table 8.2: *Final cuts for electron triggered $W \to \mu\nu$ sample*

A specifically useful variable for this channel is the transverse component of the neutrino with respect to the muon $p_{t,\nu}^{\perp}$ which makes uses of the "Mercedes-star like" event topology.

8.6.2 Selection of electron triggered $W \to \mu\nu$ events

The applied cuts for the selection of $W \to \mu\nu$ events with an electron in the detector is shown in table 8.2.

The most important variable for the discrimination between signal and background is the event $\Sigma E - P_z$ which rejects most of the low Q^2 background. Since the fraction of inelastic muon pairproduction background is higher in this sample as in the sample with a high imbalance in the calorimetric energy deposits it is necessary to introduce a higher threshold of $p_{t,\nu} \geq 18\ GeV$ for the missing transverse momentum. Also the veto condition against events with two isolated muons is important here.

Chapter 9

Results

9.1 Monte Carlo expectation

The expected event rates and efficiencies quoted in this chapter are estimated from Monte Carlo simulations of muonic W decays and the different background processes described in chapter six.

9.1.1 P_T^{calo} triggered $W \to \mu\nu$ sample

Table 9.1 shows the expected efficiency of the different cuts and their power for background rejection. The inefficiency for signal events and the rejection of background are weighted with the inverse number of conditions an event failed such that cut conditions which reject more events exclusively are counted with a higher weight,

$$\begin{aligned} \bar{\epsilon}(cut_i) &= \text{weighted inefficiency} = \text{weighted rejection} \\ &= \sum_j \frac{1}{\text{number of cuts event j failed}} \end{aligned} \tag{9.1}$$

summed over all events j rejected by cut i.

Cut efficiencies in P_T^{calo} triggered muon channel								
		signal			background		data	
cuts		expected events		weighted inefficiency	expected events	weighted rejection	events	weighted rejection
trigger	$P_{T,calo} > 12\ GeV$	45.5%	5.79	19.5%	7.37e+04	9.53%	-	-
	efficiency	38.8%	**4.94**	9.99%	**6.35e+04**	4.33%	**4.57e+04**	-
non e-p finders		36.6%	**4.66**	1.63%	**3.25e+04**	6.15%	**9.16e+03**	15.3%
muon identification	$p_{t,\mu} > 12\ GeV$	29.2%	3.71	4.33%	784	9.54%	755	12.5%
	grade 1 $\|\|$ 2	26.7%	3.4	10.4%	181	9.53%	134	17.3%
	$D_{track} > 0.5$	24.6%	3.13	3.24%	69.4	9.33%	65	3.47%
	$D_{jet} > 0.5$	24.4%	3.11	1.94%	46.4	9.25%	55	4.15%
	$E_{calo} < 8\ GeV$	22.9%	**2.91**	2.61%	**42.7**	9.24%	**48**	3.19%
neutrino	$p_{t,\nu} > 12\ GeV$	21.3%	**2.71**	3.65%	**2.29**	9.51%	**14**	6.39%
event selection	$\Sigma E - P_z < 0.9 \cdot 2\ E_{beam}(e)$ (if e)	18.9%	2.41	3.04%	1.04	8.84%	10	4.25%
	$\frac{V_{ap}}{V_p} < 0.3$	18.5%	2.35	11%	1.04	9.51%	10	5.95%
	$p_{t,\nu}^{\perp} > 6\ GeV$	15.5%	1.97	22%	0.263	9.54%	8	19.8%
	no electron in crack	15.4%	1.96	0.198%	0.259	0.0161%	8	0.248%
	two muon veto	15.2%	**1.93**	0.646%	**0.0605**	0.00172%	**7**	1.05%

Table 9.1: *Cut efficiencies in the P_T^{calo} triggered muon channel. The number of expected events after the application of the sequence of cuts is shown for simulated muonic W decays and the standard model background and compared with the number of events found in the data. For the signal the expected number of events is shown with an accompanying selection efficiency. The inefficiency of the individual cuts is weighted according to the definition in equation 9.1*

Monte Carlo expectation for P_T^{calo} triggered muon channel	
muonic W decay	1.93
muon pairproduction	0.04
tau pairproduction	0.02
all other processes	$\lesssim 0.1$

Table 9.2: *Monte Carlo expectation for events in P_T^{calo} triggered $W \to \mu\nu$ sample*

The applied weighting procedure is the reason for the low quoted values for the inefficiency of the $P_T^{calo} > 12\ GeV$ trigger condition. The other cuts are tuned to keep events passing the P_T^{calo} requirement in the selection while being more inefficient for the other events. Mainly the $p_{t,\nu}^{\perp} > 6\ GeV$ condition is highly correlated with the calorimetric imbalance and the "Mercedes star-like" event topology. Most events are rejected by both conditions which together have a weighted inefficiency of roughly 40%.

The $p_{t,\nu}^{\perp} > 6\ GeV$ requirement has an exclusive inefficiency of approximately 15%, which is high on the one hand but justified by the cutting power against background on the other hand since this cut improves the signal to background ratio by almost a factor ten. The $\Sigma E - P_z < 0.9 \cdot 2\ E_{beam}(e)$ condition also has an exclusive inefficiency of approximately 15%. It is expected to cut ≈ 0.2 events in the signal and in the background thereby improving the signal to background ratio significantly. In consideration of the conservatively large estimated error of 75% on the lepton pairproduction cross section in the former analysis [31] this cut seems to be a good choice at present and is assumed to make the analysis more robust.

The number of muonic W decay events fulfilling the selection requirements and the remaining background from Monte Carlo simulation is summarized in table 9.2. Processes which does not give a contribution to the final sample in the Monte Carlo simulation are not explicitly listed in the table, with approximately ten times the data luminosity available in the Monte Carlo simulation statistical fluctuations of this background are estimated to be $\lesssim 0.1$.

9.1.2 Electron triggered $W \to \mu\nu$ sample

With the same weighting procedure applied as for the P_T^{calo} triggered sample in the previous section, the rejection of signal and background events by the different cuts is calculated for the electron triggered muon channel. The results are shown in table 9.3.

Cut efficiencies in electron triggered muon channel								
		signal			background		data	
cuts		expected	events	weighted inefficiency	expected events	weighted rejection	events	weighted rejection
trigger	e in detector	53%	6.75	43.8%	8.49e+07	0.105%	-	-
	electron identification	16.5%	2.1	9.45%	4.17e+06	11%	-	-
	efficiency	16.5%	**2.1**	15.1%	**3.72e+06**	5.2%	-	-
non e-p finders		15.6%	**1.98**	2.03%	**3.3e+06**	7.53%	-	-
muon identification	$p_{t,\mu} > 12\ GeV$	13.4%	1.7	4.87%	6.99e+03	11.8%	-	-
	grade 1 || 2	12.5%	1.6	11.9%	676	11.8%	-	-
	$D_{track} > 0.5$	11.5%	1.46	4.4%	201	11.5%	-	-
	$D_{jet} > 0.5$	11.4%	1.45	2.51%	106	11.4%	-	-
	$E_{calo} < 8\ GeV$	10.6%	**1.35**	3.56%	**70.8**	11.4%	**53**	-
neutrino	$p_{t,\nu} > 18\ GeV$	9.36%	**1.19**	8.9%	**4.78**	11.8%	**16**	20.7%
event selection	$\Sigma E - P_z < 0.9 \cdot 2\ E_{beam}(e)$	7.13%	0.908	4.29%	0.35	11%	2	4.54%
	no electron in crack	6.81%	0.866	0.232%	0.344	0.0206%	2	0.0524%
	two muon veto	6.69%	**0.851**	0.785%	**0.0871**	0.00237%	**2**	1.22%
not in $P_{T,calo}$ sample		3.3%	**0.42**	-	**0.0777**	-	**2**	-

Table 9.3: *Cut efficiencies in the electron triggered muon channel. The number of expected events after the application of the sequence of cuts is shown for simulated muonic W decays and the standard model background and compared with the number of events found in the data. For the signal the expected number of events is shown with an accompanying selection efficiency. The inefficiency of the individual cuts is weighted according to the definition in equation 9.1*

Monte Carlo expectation for electron triggered muon channel	
muonic W decay	0.42
muon pairproduction	0.05
tau pairproduction	0.03
all other processes	$\lesssim 0.5$

Table 9.4: *Monte Carlo expectation for events in electron triggered $W \to \mu\nu$ sample*

In the data a preselected event sample is used which contains events with a good muon candidate. Therefore the observed number of events can only be compared with the Monte Carlo expectation after application of the complete muon identification.

After the muon identification one can see a discrepancy in the effectiveness of the $p_{t,\nu} > 18\ GeV$ requirement in the table. Differing from the events with $P_T^{calo} > 12\ GeV$ the transverse momentum balance of events selected in this channel is dominated by the contribution from the muon track. Hence a deviation of the resolution in the measurement of track momenta primarily effects the electron triggered event sample. The observed distribution of missing transverse momenta in a control sample study (to be found in the appendix) indicates that the resolution is overestimated in the Monte Carlo simulation and the long tails in the data are not precisely described.

This still needs some further investigation.

The expected number of selected events is summarized in table 9.4. An approximate 20% increase in efficiency for the detection of muonic W decays is expected from the analysis of events triggered by an electron in the detector, but also a worse signal to noise ratio compared to the P_T^{calo} triggered event sample. Since the photoproduction Monte Carlos used for the background estimation in the P_T^{calo} triggered channel have to harsh precuts to be used in the electron triggered channel and the available Monte Carlos without a preselection have a smaller event statistic the uncertainty on the background estimation is higher in this channel.

9.2 Events in the data

A total of nine candidate events for muonic W decay is found in the 1994-2000 e^+ dataset whereas only 2.5 were expected from Monte Carlo simulation. Table 9.5 shows the contributions of the 1994-97 and 1999-2000 running periods in comparison with the expected number of events from Monte Carlo simulation.

The distribution of the event $\Sigma E - P_z$ and missing transverse momentum $P_{T,miss}$ of the selected events is shown in comparison of the expectation for muonic W decays and background processes passing the selection in figure 9.1.

9.2.1 P_T^{calo} triggered $W \to \mu\nu$ sample

Seven of the nine events pass the selection requirements of the $P_T^{calo} \geq 12\ GeV$ channel.

Selected events in the 1994-2000 e^+ dataset ($101pb^{-1}$)			
	data	Σstandard model	W decay
P_T^{calo} sample	7	1.99	1.93
electron sample	2	0.50	0.42

Table 9.5: *Number of selected events in the data compared to the Monte Carlo expectation, the dominant contribution to the sum over all standard model processes is expected from W production*

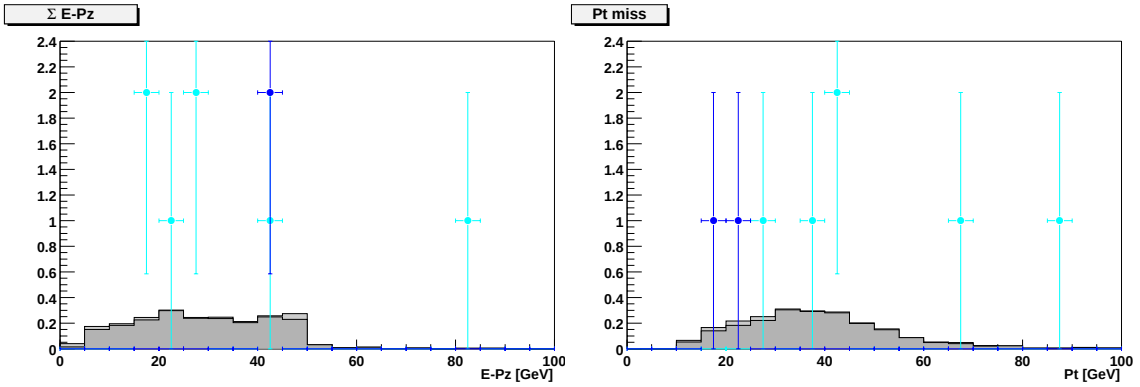

Figure 9.1: $\Sigma E - P_z$ *and* $P_{T,miss}$ *distributions for events selected in the* P_T^{calo} *(dark points) or electron triggered channel (light points), the expectation for muonic W decays is displayed as the dark histogram, the background contribution is shown in light on top. Event 16793 of run 195308 selected in the* P_T^{calo} *triggered sample is not included in the diagram because its missing* P_T *is practically undetermined*

The events are shown in the following event displays with their event characteristics quoted next to the display.

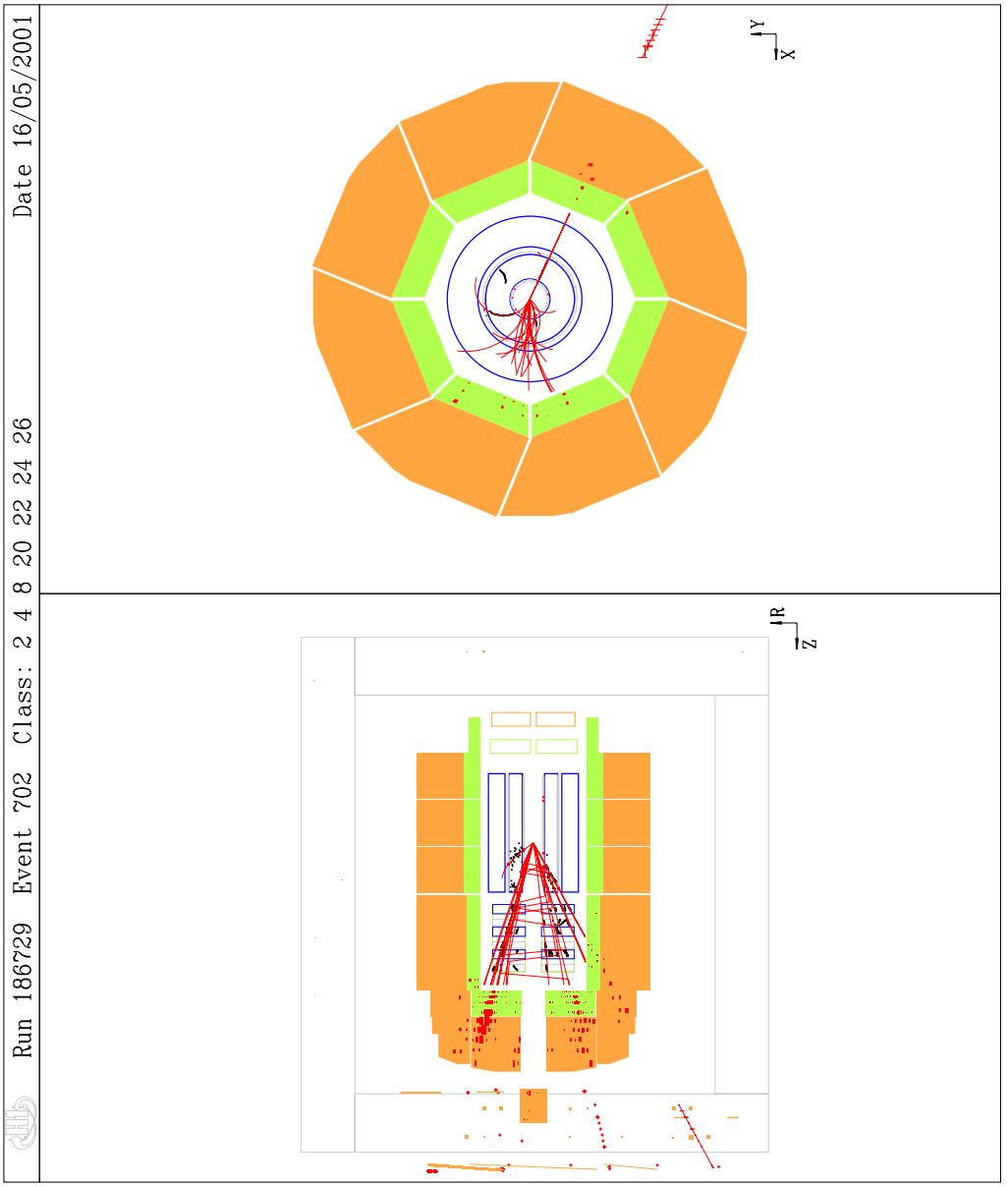

event properties	
isolated muon	
$p_{T,\mu}$	$27.6^{+6.41}_{-4.38}$ GeV
θ_μ	28.9°
ϕ_μ	−155°
hadronic system	
$P_{T,X}$	64.4 GeV
ϕ_X	2.04°
missing momentum	
$p_{T,\nu}$	$40.5^{+4.14}_{-5.01}$ GeV
ϕ_ν	166°
$\not{p}_{T,\nu}$	25.5 GeV
hypothetic W = $\mu + \nu$	
M_W^T	$22.4^{+4.49}_{-2.89}$ GeV

Figure 9.2: *Event 702 of run 186729*

event properties	
isolated muon	
$p_{T,\mu}$	$37.9^{+8.65}_{-5.94}\ GeV$
θ_μ	35.4°
ϕ_μ	162°
hadronic system	
$P_{T,X}$	26.8 GeV
ϕ_X	45.5°
missing momentum	
$p_{T,\nu}$	$41.4^{+6.79}_{-4.33}\ GeV$
ϕ_ν	−57.5°
$p^{\perp}_{T,\nu}$	26.6 GeV
electron	
E_e	7.57 GeV
θ_e	118°
hypothetic W = $\mu + \nu$	
M_W	$81.1^{+13.1}_{-9}\ GeV$
hypothetic top = $X + W$	
M_{top}	$127^{+9.42}_{-6.13}\ GeV$

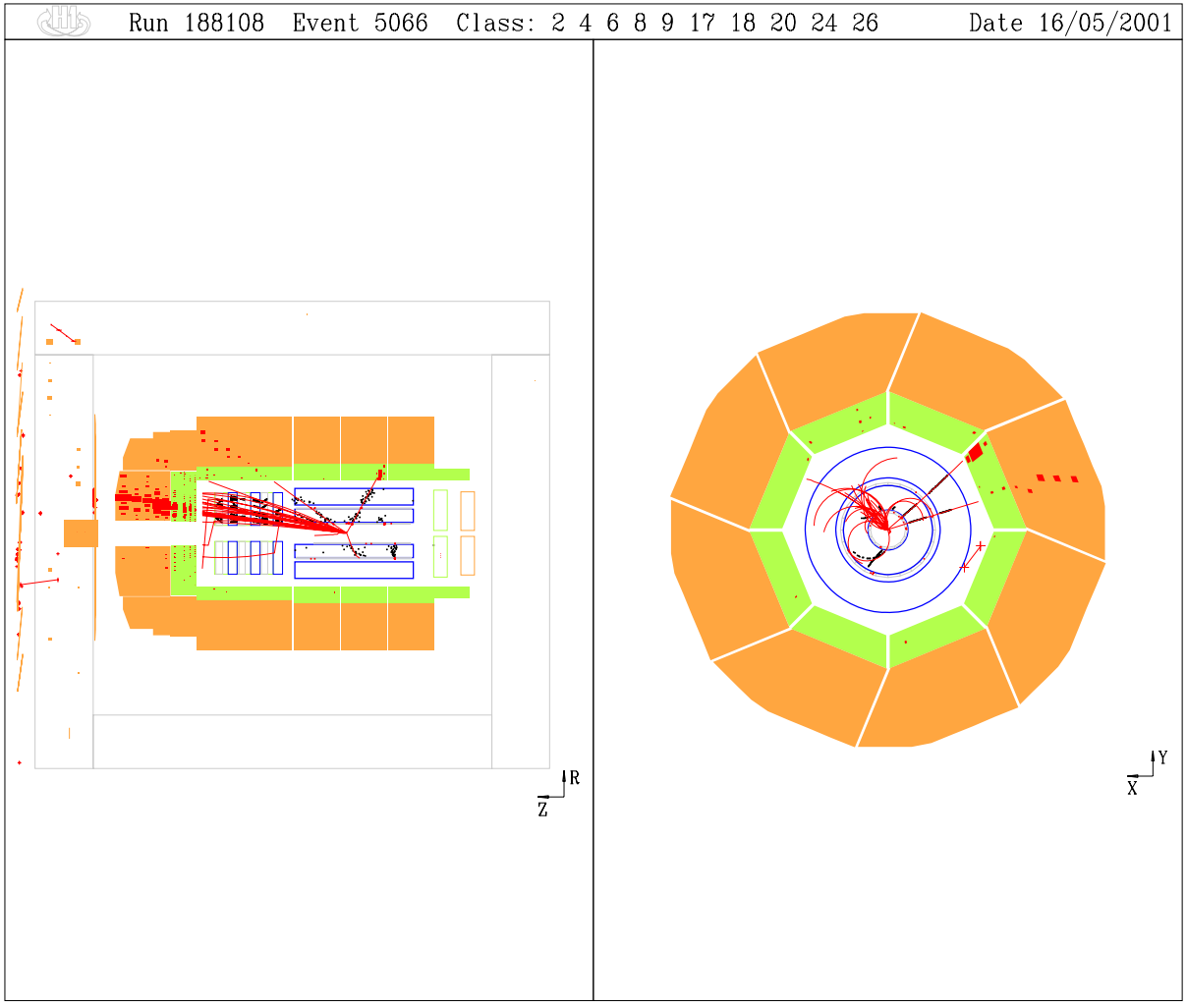

Figure 9.3: *Event 5066 of run 188108*

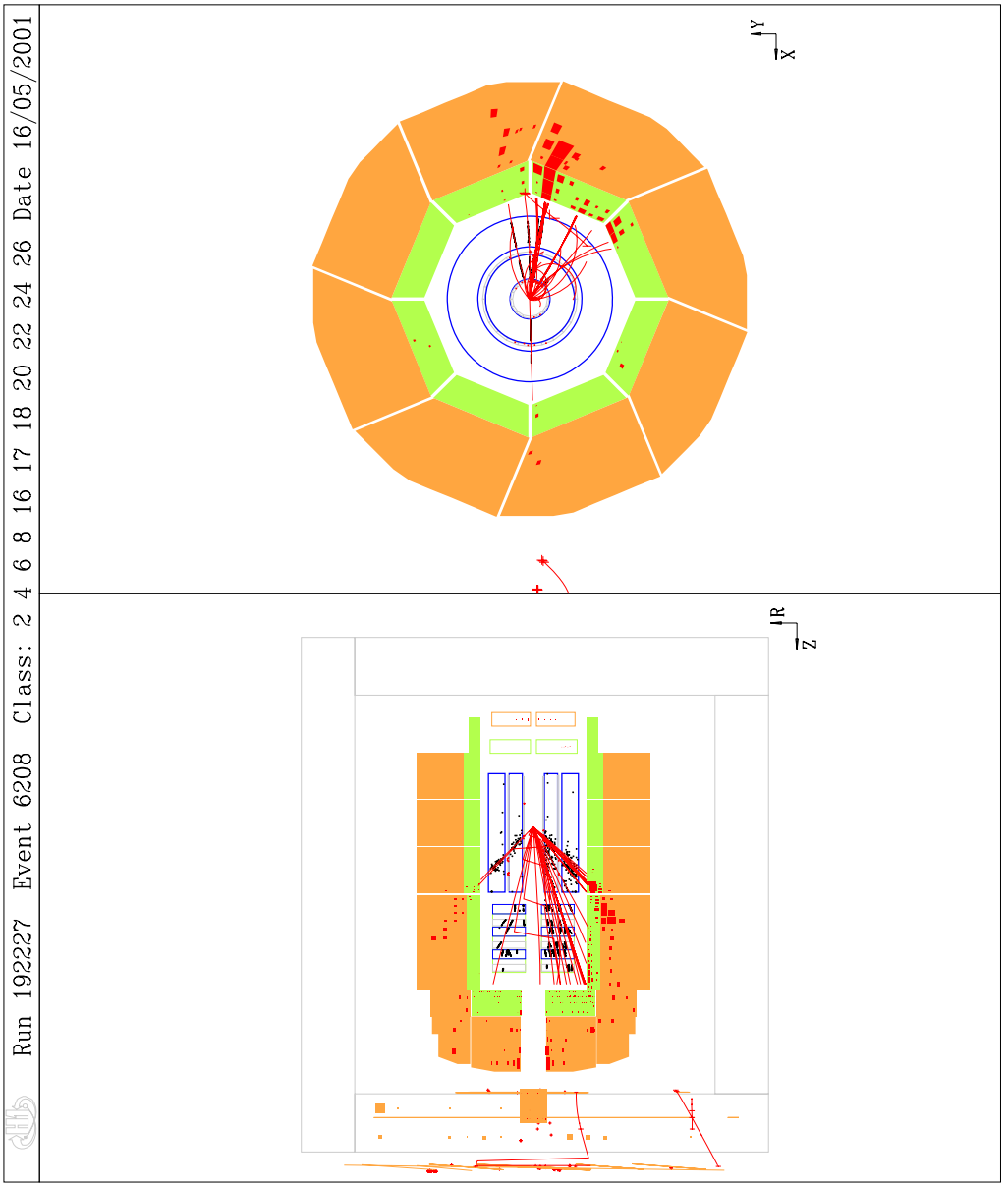

event properties	
isolated muon	
$p_{T,\mu}$	$79^{+50.1}_{-22.1}$ GeV
θ_μ	28.6°
ϕ_μ	−1.76°
hadronic system	
$P_{T,X}$	57.6 GeV
ϕ_X	−166°
missing momentum	
$p_{T,\nu}$	$28.3^{+43.9}_{-11.4}$ GeV
ϕ_ν	145°
$\not{p}_{T,\nu}$	15.7 GeV
hypothetic W = $\mu + \nu$	
M_W^T	$90.5^{+99.3}_{-46.5}$ GeV

Figure 9.4: *Event 6208 of run 192227*

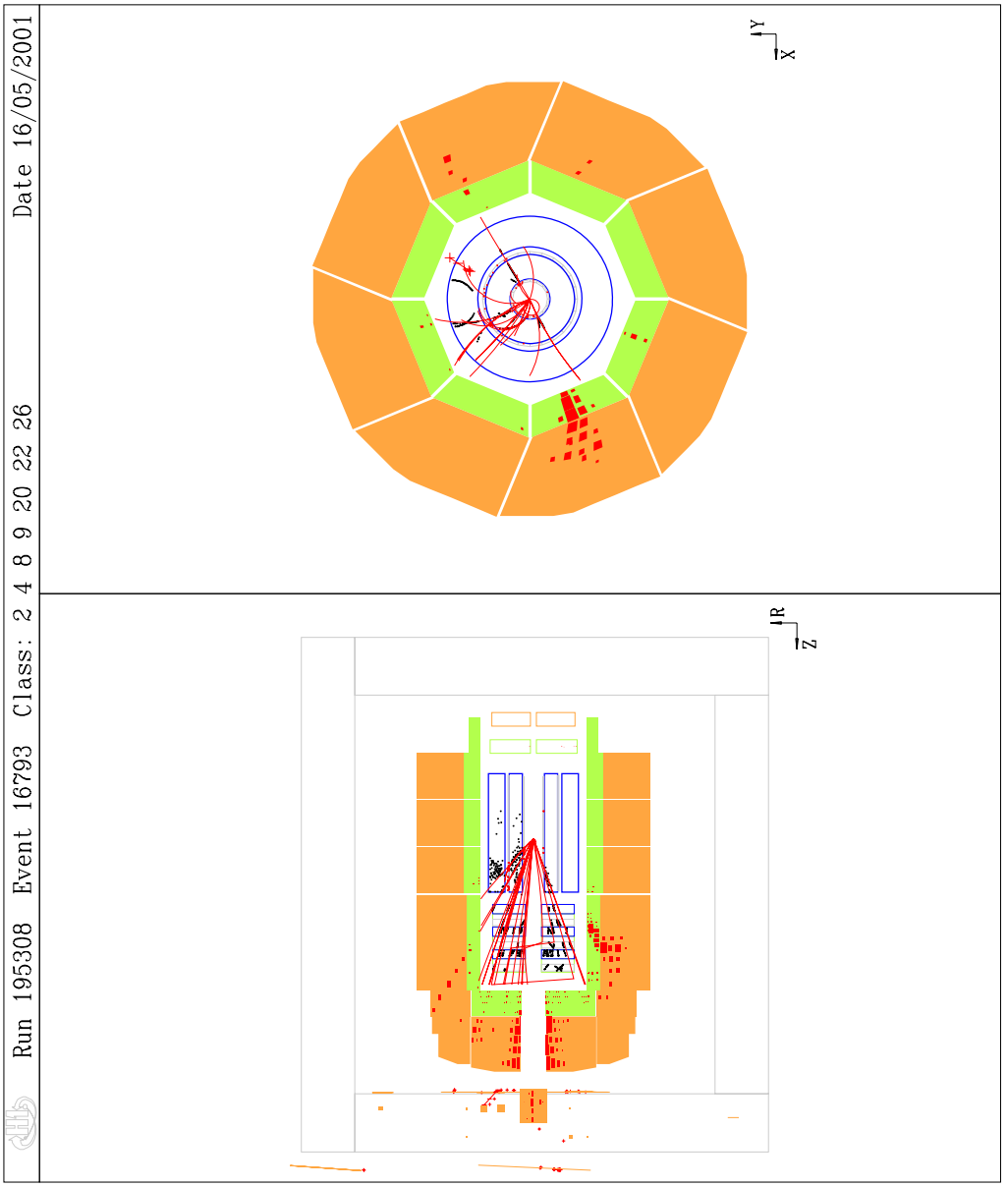

event properties	
isolated muon	
$p_{T,\mu}$	$255^{+\infty}_{-162}$ *GeV*
θ_μ	30.9°
ϕ_μ	149°
hadronic system	
$P_{T,X}$	29.6 *GeV*
ϕ_X	−12.7°
missing momentum	
$p_{T,\nu}$	$228^{+\infty}_{-198}$ *GeV*
ϕ_ν	−33.4°
$p^{\perp}_{T,\nu}$	9.34 *GeV*
hypothetic W = $\mu + \nu$	
M_W^T	$482^{+\infty}_{-482}$ *GeV*

Figure 9.5: *Event 16793 of run 195308*

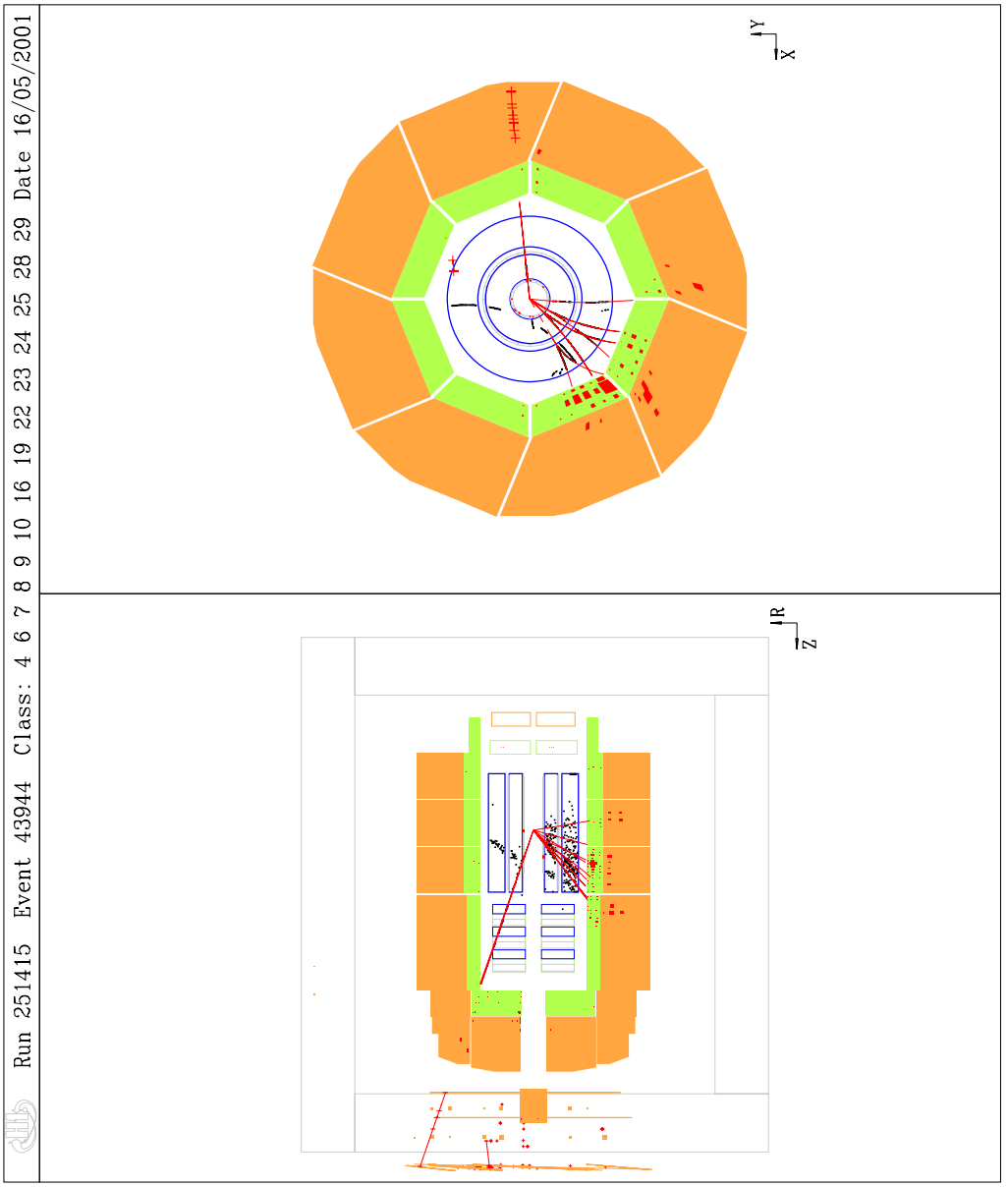

event properties	
isolated muon	
$p_{T,\mu}$	$102^{+103}_{-34.2}$ GeV
θ_μ	18.8°
ϕ_μ	174°
hadronic system	
$P_{T,X}$	17.5 GeV
ϕ_X	−43.8°
missing momentum	
$p_{T,\nu}$	$89.1^{+84}_{-35.7}$ GeV
ϕ_ν	0.978°
$\not{p}_{T,\nu}$	10.8 GeV
hypothetic W = $\mu + \nu$	
M_W^T	$191^{+169}_{-72.2}$ GeV

Figure 9.6: *Event 43944 of run 251415*

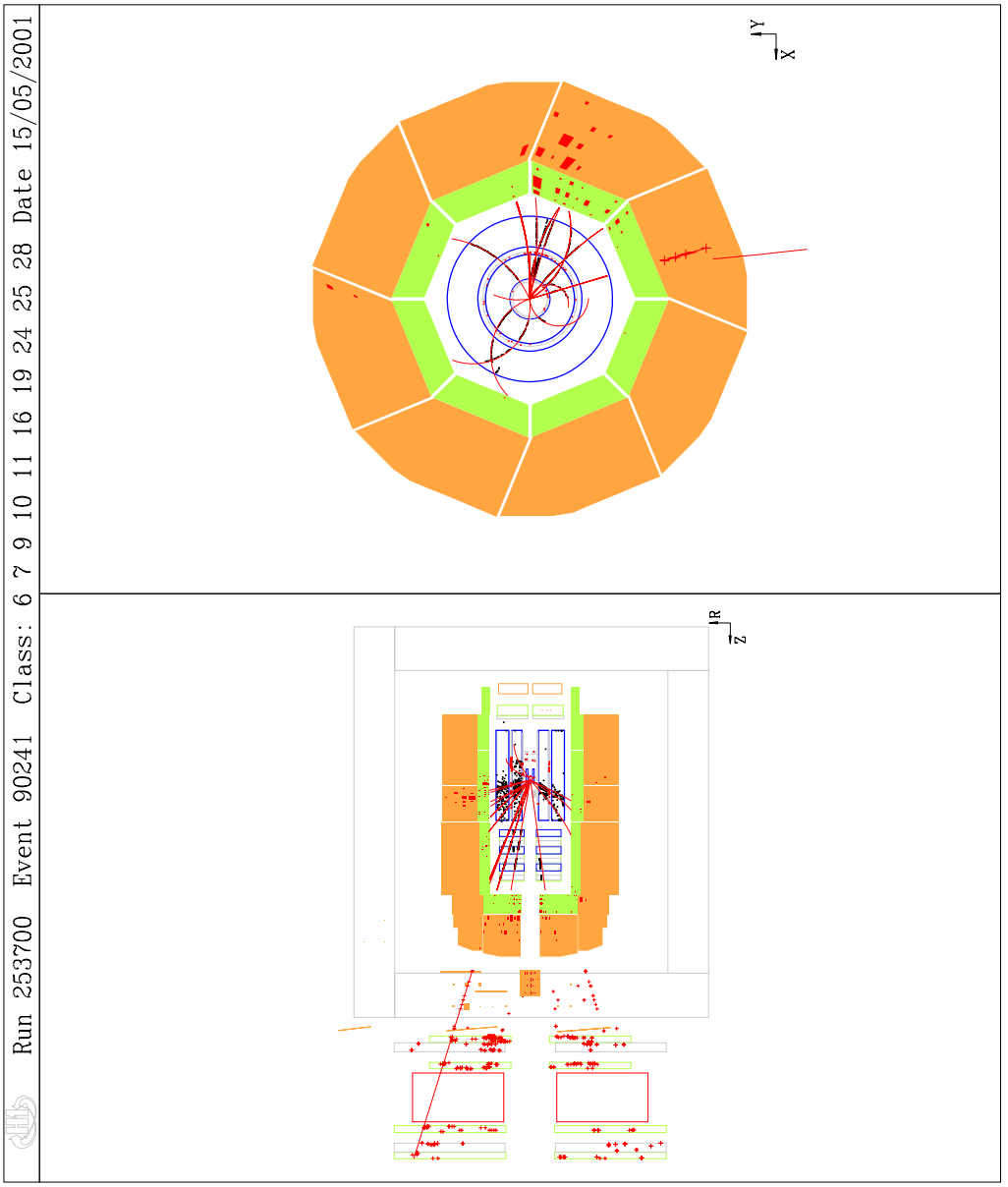

event properties	
isolated muon	
$p_{T,\mu}$	$20.1^{+4.35}_{-3.04}$ GeV
θ_μ	16.9°
ϕ_μ	−106°
hadronic system	
$P_{T,X}$	20.6 GeV
ϕ_X	−167°
missing momentum	
$p_{T,\nu}$	$35.2^{+4.22}_{-3.21}$ GeV
ϕ_ν	43.3°
$p_{T,\nu}^{\perp}$	17.9 GeV
hypothetic W = $\mu+\nu$	
M_W^T	$51.4^{+8.49}_{-6.16}$ GeV

Figure 9.7: *Event 90241 of run 253700*

event properties	
isolated muon	
$p_{T,\mu}$	$21.3^{+2.5}_{-2.02}$ GeV
θ_μ	63.9°
ϕ_μ	102°
hadronic system	
$P_{T,X}$	47.9 GeV
ϕ_X	49.1°
missing momentum	
$p_{T,\nu}$	$65.7^{+2.89}_{-2.64}$ GeV
ϕ_ν	−113°
$p^{\perp}_{T,\nu}$	37.2 GeV
electron	
E_e	13.5 GeV
θ_e	17.3°
hypothetic W = $\mu + \nu$	
M_W	$72.1^{+6.03}_{-4.92}$ GeV
hypothetic top = $X + W$	
M_{top}	$152^{+5.2}_{-4.65}$ GeV

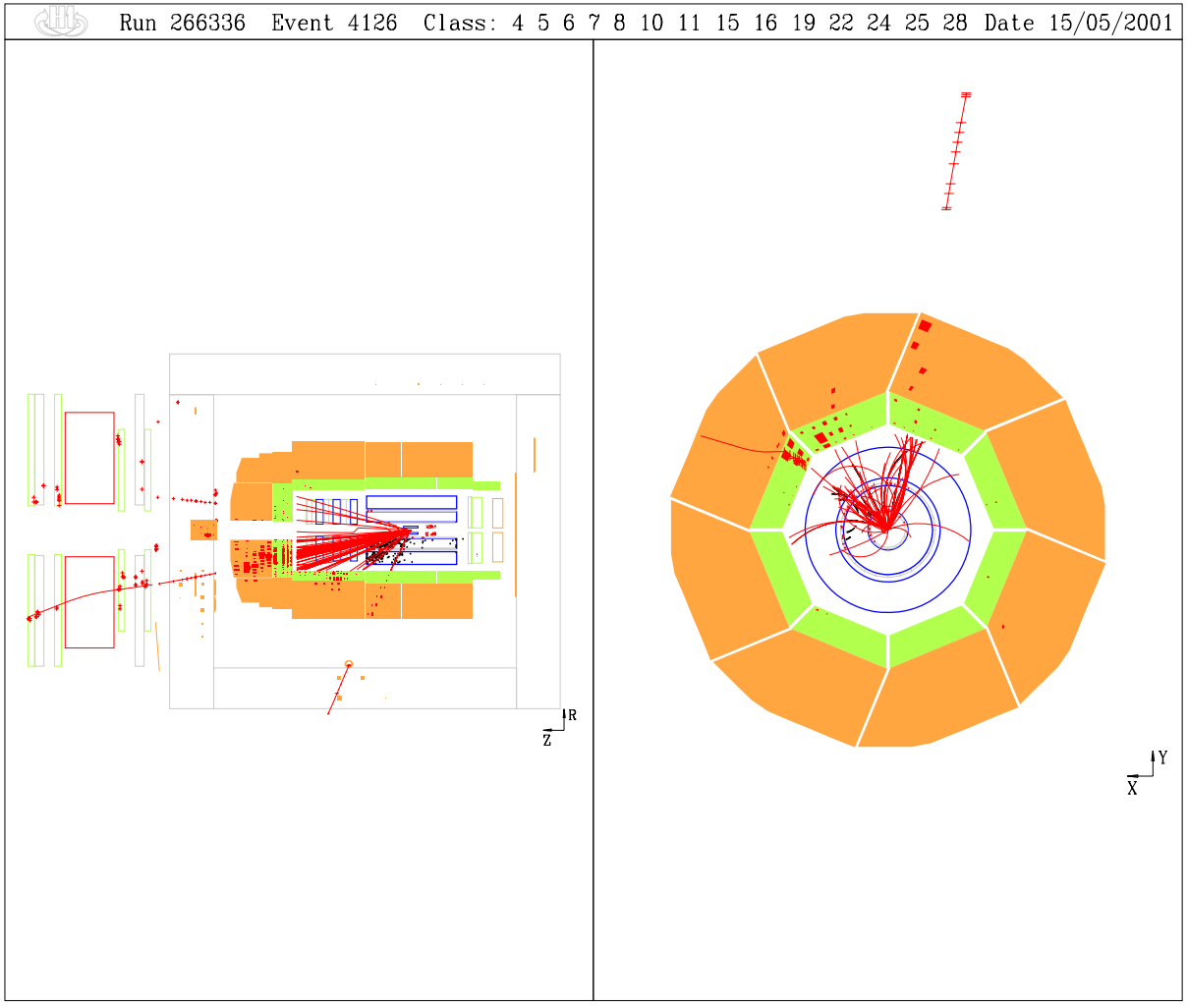

Figure 9.8: *Event 4126 of run 266336*

The hadronic transverse momentum $P_{T,X}$ spectrum of the observed events is compared with the standard model Monte Carlo expectation in figure 9.9. In contrast to the Monte Carlo expectation the events are not concentrated at low $P_{T,X}$ but distributed to rather high values.

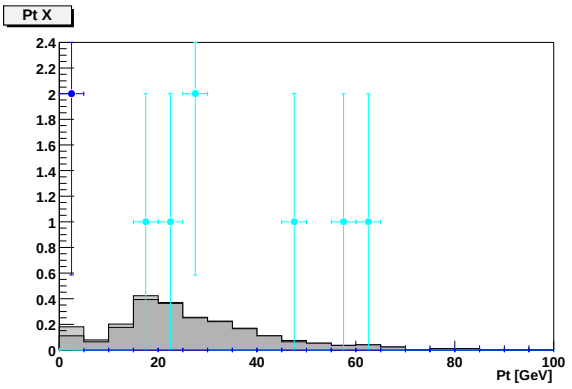

Figure 9.9: *Hadronic P_T distribution of muon events selected in the P_T^{calo} (light points) or electron triggered channel (dark points). The expectation for muonic W decays is displayed as the dark histogram, the background contribution is shown in light on top*

This observation motivates the hypothesis of anomalous single top production which yields a natural explanation for the excess at high hadronic transverse momenta in terms of a hard b quark jet from the top decay.

A hypothetic top mass is calculated (as the invariant mass of the hadronic system and the W) for events with fully reconstructible kinematics by an electron in the detector. For the two events 5066 *of run* 188108 and 4126 *of run* 266336 with an electron candidate in the P_T^{calo} sample the obtained mass values are near the top quark mass but significantly too low considering the calculated error bounds. The muon in the first event is measured with the wrong charge for the assumed single top decay $t \to bW^+ \to b\mu^+\nu$ and is found to be incompatible with the top hypothesis.

In the second event the reconstructed mass value is not very reliable. The electron candidate in the forward region ($\theta_e \approx 17°$) is likely to have hadronic origin, the energy cluster identified as the electron in this event has no good track link and is not well isolated in the calorimeter. A more detailed study of this event [1] which considered the electron candidate to belong to the hadronic system and uses a W mass hypothesis instead of the event $E - P_z$ with the electron for the event reconstruction has found the event to be compatible with a top signal.

9.2.2 Electron triggered $W \to \mu\nu$ sample

Two new candidate events for muonic W decays are found in the channel with an electron in the detector. They are shown together with the reconstructed event characteristics in the following event displays.

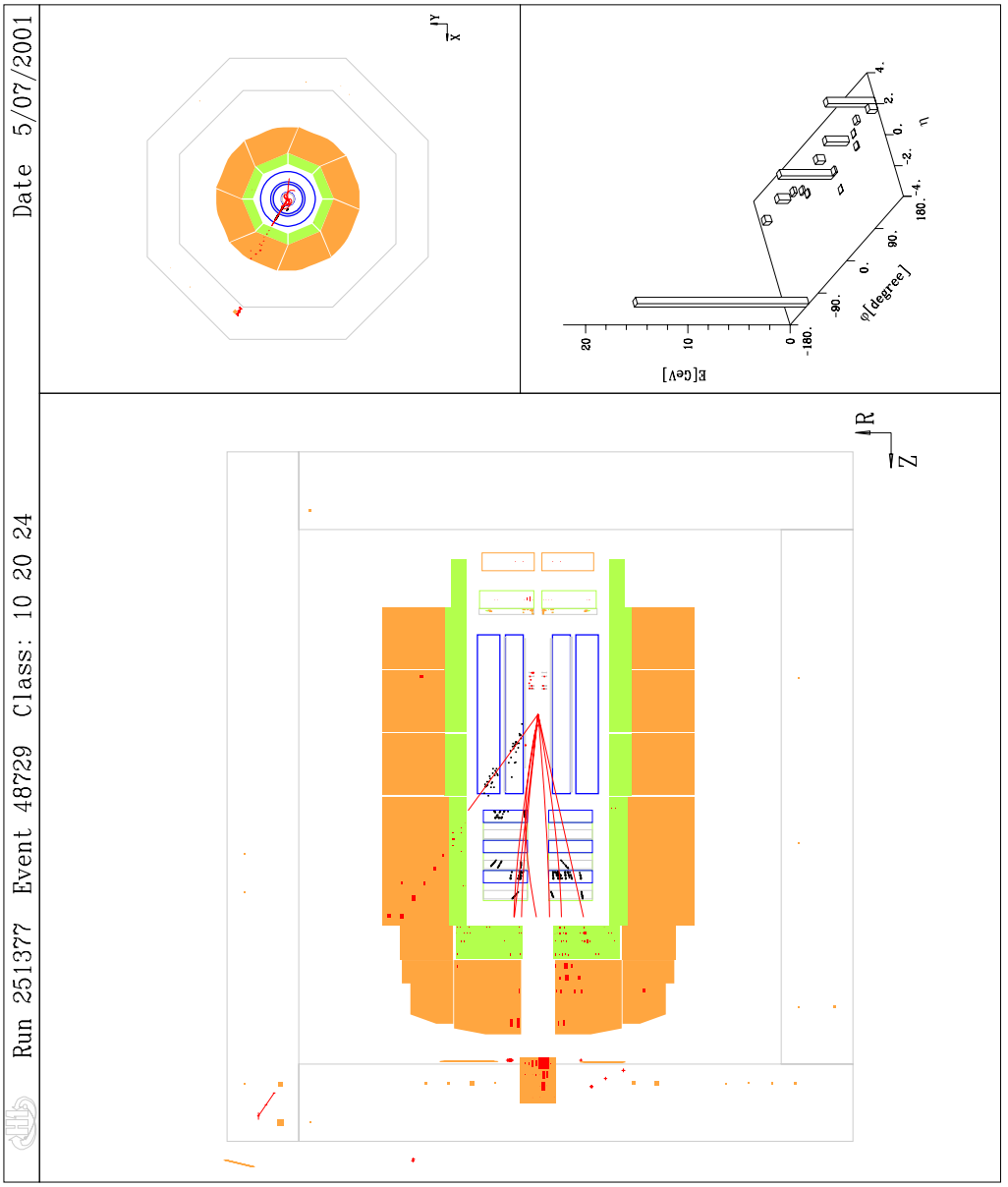

event properties	
isolated muon	
$p_{T,\mu}$	$23.8^{+2.41}_{-2}$ GeV
θ_μ	36°
ϕ_μ	30.4°
missing momentum	
$p_{T,\nu}$	$21.7^{+2.34}_{-2}$ GeV
ϕ_ν	−147°
$\not{p}_{T,\nu}$	1.18 GeV
electron	
E_e	16 GeV
θ_e	177°
hypothetic W = $\mu + \nu$	
M_W^T	$45.4^{+4.71}_{-4.01}$ GeV

Figure 9.10: *Event 48729 of run 251377*

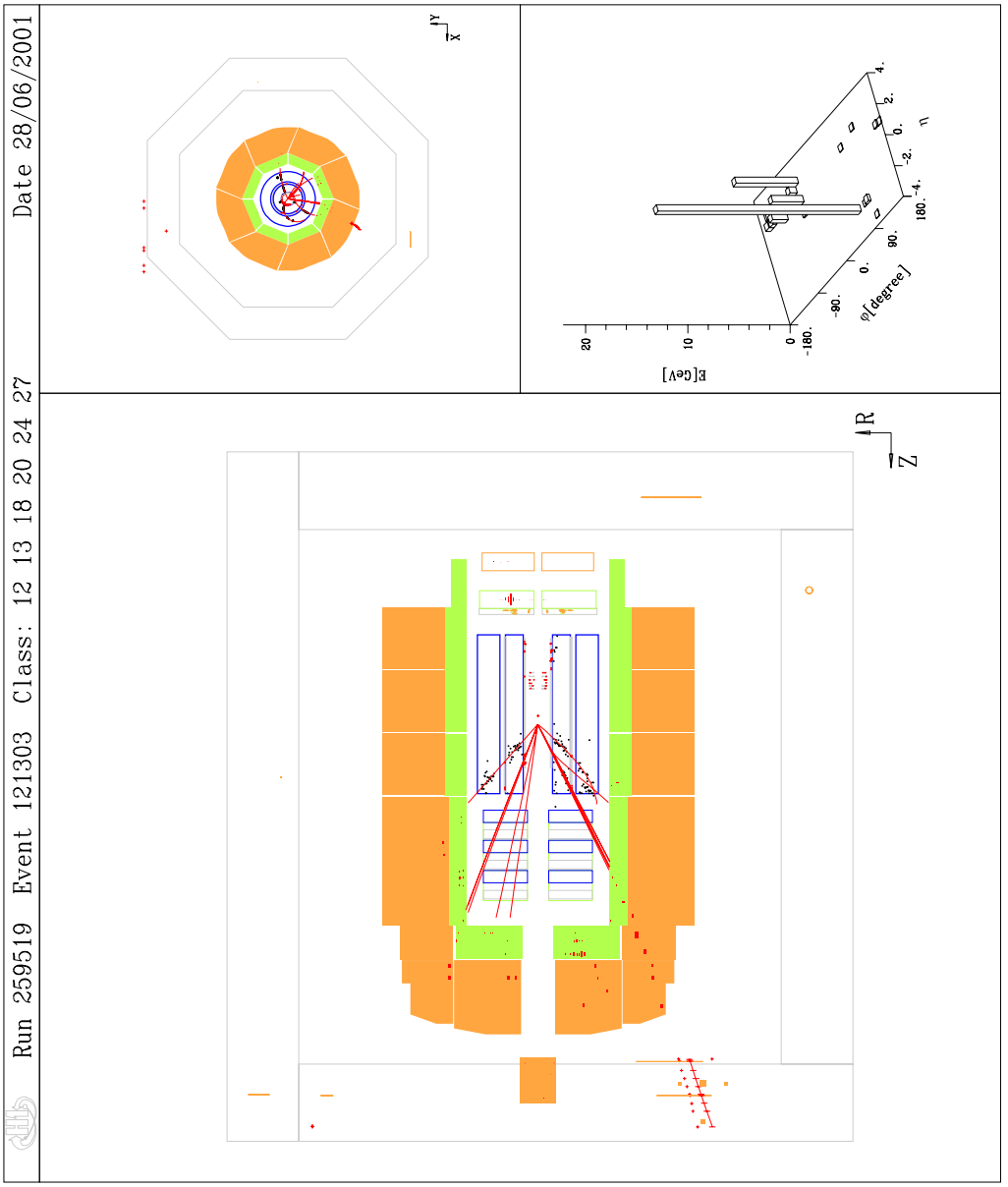

event properties	
isolated muon	
$p_{T,\mu}$	$21.4^{+43.1}_{-8.56}$ GeV
θ_μ	26.6°
ϕ_μ	−81.7°
missing momentum	
$p_{T,\nu}$	$19.3^{+23.2}_{-9.86}$ GeV
ϕ_ν	101°
$\not{p}_{T,\nu}$	0.873 GeV
electron	
E_e	19.2 GeV
θ_e	167°
hypothetic W = $\mu + \nu$	
M_W^T	$40.6^{+48.1}_{-14.1}$ GeV

Figure 9.11: *Event 121303 of run 259519*

The two observed events can still be explained as a mere statistical fluctuation, but it is interesting to note that there is an excess of the same order as in the P_T^{calo} sample.

Due to the measured beam electron one can fully reconstruct the event kinematics and calculate the hypothetic W mass for all events in this channel. In both events the reconstructed mass values are untypical low. The calculated mass in event 121303 *of run* 259519 is compatible with the world average value of the W mass within the calculated uncertainty dominated by the track measurement of the muon momentum. In this event the muon track is partially measured in the central and forward tracking detectors. A visual scan of the event revealed that both track segments are rather short. The quoted transverse momentum is taken from the *combined track* determined by a fit of both track segments to the event vertex. Fits of track segments within the individual trackers give transverse momentum values of 4.9 GeV for the central track and 2.8 GeV for the forward track which would reduce the reconstructed missing momentum to 2.9 GeV and 1.1 GeV respectively.

The muon track in the other event 48729 *of run* 251377 has a long track length in the central tracking chamber such that the muon momentum is much better determined giving confidence in the reconstructed missing momentum. The quoted error on the calculated W mass is therefore small. It makes an interpretation of the event as W decay difficult. Since the tracking detectors are known to sometimes underestimate their errors and the mass resolution is estimated to have a width of roughly 25 GeV in the Monte Carlo simulation the calculated mass value for the event does not completely exclude the interpretation of the event as W decay.

Events in this sample are unlikely to be decays of top quarks. In the top decay the b jet produces a high transverse imbalance in the calorimetric energy deposits such that the majority of events would pass the $P_T^{calo} > 12\ GeV$ requirement and are thus contained in the P_T^{calo} sample.

9.3 Comparison with previous analyses

The selection efficiency in the P_T^{calo} triggered sample is nearly identical to that in the previous analysis based on the thesis by Nick Malden [31].

The former analysis employs a harsher cut on V_{ap}/V_p to reduce the photoproduction and neutral current background.

For the rejection of muon pairproduction events the former analysis cuts on the azimuthal angle $\Delta\phi_{\mu-X}$ between the muon and the hadronic system. In the inelastic muon pairproduction events with a high $P_T^X > 12\ GeV$ transverse momentum hadronic system the hadronic system is usually balanced in $r\phi$ space by one of the muons while the other muon vanishes through the beam pipe and does not effect the p_t balance of the event. To keep the efficiency loss for muonic W decays small the requirement on the *acoplanarity angle* $\Delta\phi_{\mu-X}$ is formulated as a two dimensional cut. It is applied if the number of tracks in the central tracking detector is two or smaller. Note that the hadronic system is mostly scattered in the forward region of the H1 detector outside the geometrical acceptance of the central tracking detector and does not contribute to the number of central tracks.

In this analysis these cuts are substituted by the $p_{t,\nu}^{\perp} > 6\ GeV$ condition

variable	cut value in official	cut value in this analysis
V_{ap}/V_p	$< 0.4, < 0.15$ if $P_T^{calo} < 25\ GeV$	< 0.3
$P_{t,X}$	$> 12\ GeV$	-
$\Delta\phi_{\mu-X}$	$< 170°$ if ≤ 2 central tracks	-
$p_{t,\nu}^{\perp}$	-	$> 6\ GeV$
$\Sigma E - P_z$ (if e)	-	$< 0.9 \cdot 2\ Ebeam(e)$

Table 9.6: *Cut values for cuts different in this analysis compared to the previous analysis [31]*

Comparison of selected events in 1994-2000 e^+ dataset ($101pb^{-1}$)			
	data	Σstandard model	W decay
previous analysis	8	2.57	2.11
this analysis	7	1.99	1.93

Table 9.7: *Number of selected events in the P_T^{calo} triggered channel. The table shows the number of events found in the H1 data and the Monte Carlo expectation for the previous analysis [31] in comparison with this analysis.*

which is a more general cut condition to ensure that the reconstructed missing momentum is not simply due to a missmeasurement of the muon track.

The cut conditions which are different in the two analyses are summarized in table 9.6.

This analysis has an approximately 8.5% lower signal efficiency than the previous one and an improved signal to background ratio by roughly a factor five. The lower efficiency of this analysis is mainly due to the $\Sigma E - P_z$ condition introduced in this analysis to achieve a higher robustness in terms of fluctuations of the lepton pairproduction background. (Without this cut the efficiency of this analysis would be slightly higher than in the previous analysis with an improvement in the signal to background ratio of still approximately two.)

The Monte Carlo expectation for the event selection in both analyses and the resulting number of selected events in the data is shown in table 9.7.

In comparison with the previous analysis one event is lost due to the $p_{t,\nu}^{\perp} > 6\ GeV$ requirement. This is in good agreement with the estimated exclusive inefficiency $\approx 15\%$ of this cut. The lost event is shown in picture 9.12.

No new event is found in the data set which could replace the one lost. The one event deviation is compatible with a statistical fluctuation in the small data set.

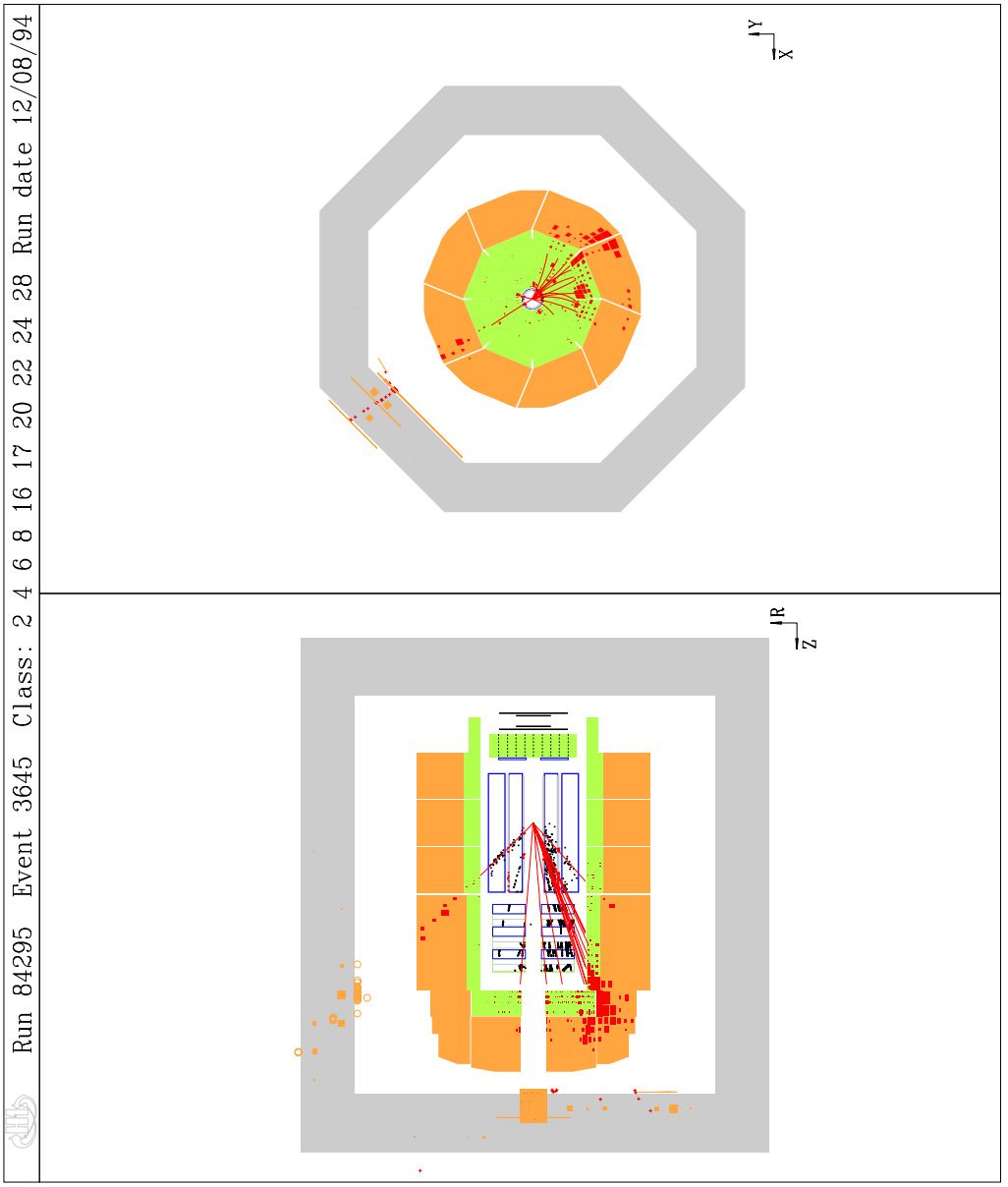

event properties	
isolated muon	
$p_{T,\mu}$	$26.9^{+4.11}_{-3.15}$ GeV
θ_μ	46.4°
ϕ_μ	57.3°
hadronic system	
$P_{T,X}$	43.9 GeV
ϕ_X	−119°
missing momentum	
$p_{T,\nu}$	$17.1^{+3.93}_{-4.53}$ GeV
ϕ_ν	67.8°
$p^{\perp}_{T,\nu}$	3.12 GeV
hypothetic W = $\mu+\nu$	
M_W^T	$3.94^{+0.899}_{-0.533}$ GeV

Figure 9.12: *Event 3645 of run 84295. This event is selected in the previous analysis [31], but fails the $p^{\perp}_{t,\nu} > 6$ GeV cut required in this analysis*

Chapter 10

Summary

Nine events with isolated high p_t muons and missing transverse momentum are observed in the H1 data compared to a standard model expectation of ≈ 2.50 from which a contribution of ≈ 2.35 is expected from W production.

The observed events are compatible with muonic W decays, reconstructed transverse masses and the invariant mass of muon and neutrino calculated for events with an electron in the detector agree with the expectation from Monte Carlo simulation.

Measured high transverse momenta of the hadronic system X motivates the hypothesis of anomalous single top production in flavour changing neutral current processes. This idea is currently examined by other H1 analyses.

In comparison with previous analyses the detection efficiency for muonic W decays is increased by approximately 20% (from 15.2% to 18.5%) in this analysis by using an additional trigger which is sensitive to muon events with an electron in the detector. Two new events are found in the electron triggered channel in $101 pb^{-1}$ of H1 e^+p data taken during the years 1994-97 and 1999-2000.

For the P_T^{calo} triggered events this analysis is compatible with the results of the previous analysis. This analysis achieves a signal to background ratio which is better by roughly a factor of five than the former analysis for the cost of an approximately 8.5% lower efficiency. One of the eight events observed in the data set selected by the previous analysis is lost.

The overall detection efficiency is still limited by the trigger setup but can possibly be increased by the H1 upgrade program currently being installed. From 2002 on a *fast track trigger* will allow to trigger events on high p_t tracks.

When H1 starts data taking after the Hera upgrade in autumn 2001 it is foreseen to collect the amount of data available for this analysis during each year. With the higher luminosity coming the event statistic will hopefully be high enough then to clarify the origin of the observed excess.

Chapter 11

Appendix

11.1 Control plots

For the P_T^{calo} triggered muonic W decays a control sample study has already been done by Nick Malden in his thesis [31]. He got a good background description and nice looking control plots.

Since electron candidates in the liquid argon calorimeter were also already investigated for the electronic W decays in the former analysis the control plots will concentrate on events with an electron in the spaghetti calorimeter here.

Events enter the control sample if they have an electron candidate in the detector fulfilling the electron identification requirements and an isolated muon with at least 6 GeV transverse momentum whereas no missing momentum is required.

Picture 11.1 shows the distribution of the energy and polar angle for events with an electron in the SpaCal. The increase in the number of events with electrons in the backward direction in the data seems reasonable since the cross section is larger for smaller momentum transfers Q^2. It looks like there is a cutoff for polar angles $\theta_e \gtrsim 172°$ in the Monte Carlo simulation but no such precut could be found in the generator steering.

In picture 11.2 the missing transverse momentum is shown together with the event $\Sigma E - P_z$ for events with an electron either in the SpaCal or the LAr calorimeter. The expected number of events in the data agrees with the Monte Carlo expectation and the shape of the distributions are reasonably well described.

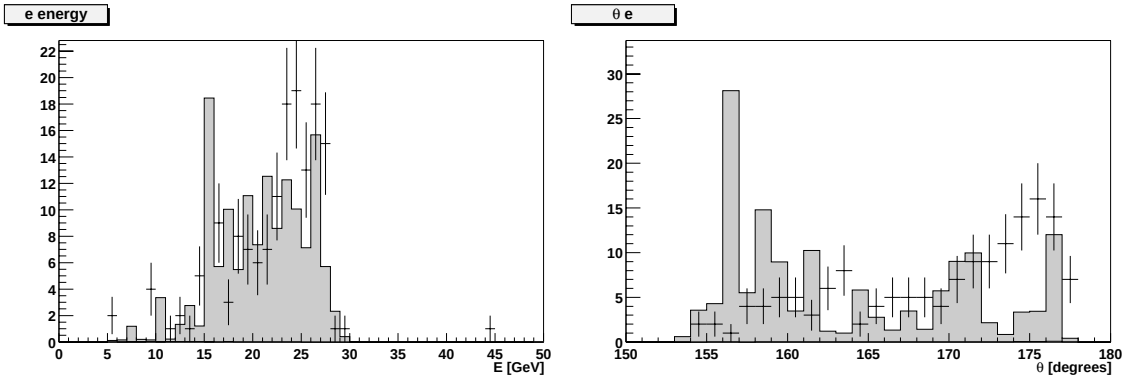

Figure 11.1: *Distribution of electron energy and polar angle in events selected in the data (points) compared to the standard model Monte Carlo expectation (histogram)*

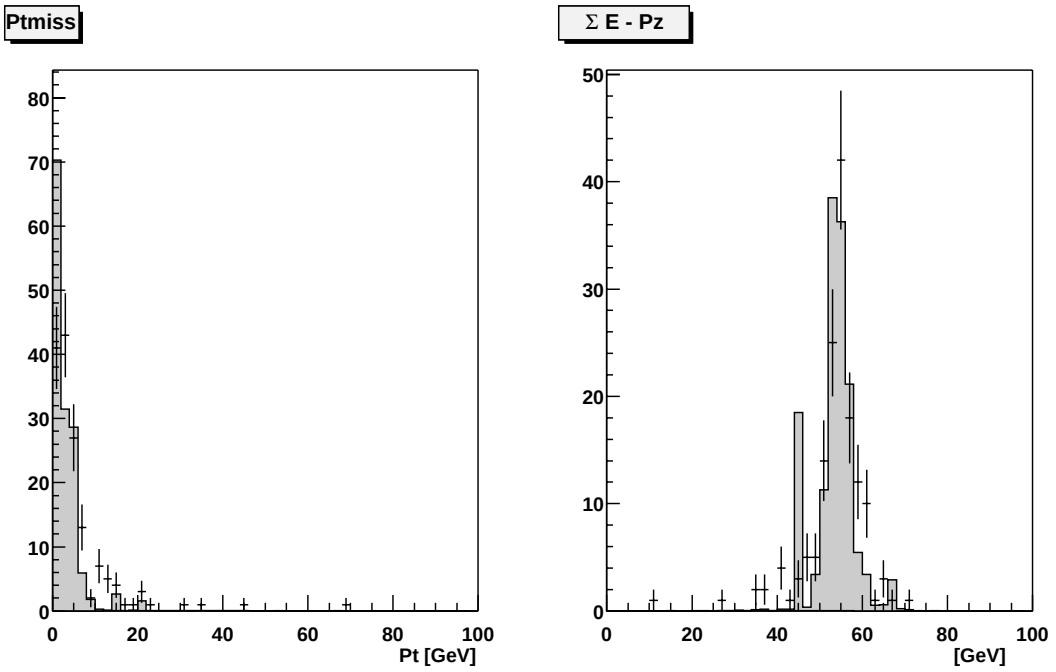

Figure 11.2: *Distribution of missing transverse momentum and $\Sigma E - P_z$ of events selected in the data (points) compared to the standard model Monte Carlo expectation (histogram)*

Bibliography

[1] *Search for Single Top Production in ep collisions at HERA*, ICHep2000, Osaka.

[2] F. Abe et al. Search for flavor-changing neutral current decays of the top quark in p anti-p collisions at $\sqrt{s} = 1.8\ TeV$. *Phys. Rev. Lett.*, 80:2525–2530, 1998.

[3] I. Abt et al. The H1 detector at HERA. *Nucl. Instrum. Meth.*, A386:310, 1997.

[4] C. Adloff et al. Diffraction dissociation in photoproduction at HERA. *Z. Phys.*, C74:221–236, 1997.

[5] C. Adloff et al. Observation of events with an isolated high energy lepton and missing transverse momentum at HERA. *Eur. Phys. J.*, C5:575, 1998.

[6] P. Bate. *High Transverse Momentum 2-Jet and 3-Jet Cross Section Measurements in Photoproduction*. PhD thesis, University of Manchester, 1999.

[7] U. Baur, J.A.M. Vermaseren, and D. Zeppenfeld. Electroweak vector boson production in high-energy e p collisions. *Nucl. Phys.*, B375, 1992.

[8] Martin Breidenbach et al. Observed behaviour of highly inelastic electron - proton scattering. *Phys. Rev. Lett.*, 23:935–939, 1969.

[9] W. Buchmueller and G. Ingelmann, editors. *LPAIR: A Generator for Lepton Pair Production*, volume 3. DESY, Hamburg, 1991. Proceedings of the Workshop *Physics at HERA*.

[10] S. Catani, Yu.L. Dokshitzer, M.H. Seymour, and B.R. Webber. Longitudinally invariant K(t) clustering algorithms for hadron-hadron collisions. *Nucl. Phys.*, B406:187–224, 1993.

[11] K. Charchulaa, G. Schuler, and H. Spiesberger. Combined QED and QCD radiative effects in deep inelastic lepton-scattering: the Monte Carlo generator DJANGO6. *Comput. Phys. Commun.*, 81:381, 1994.

[12] H1 collaboration. QESCAT - e identification software in H1PHAN. Part of H1PHAN (PHysics ANalysis) library.

[13] G.M. de Divitiis, R. Petronzio, and L. Silvestrini. Flavour changing top decays in supersymmetric extensions of the standard model. *Nucl. Phys.*, B504:45–60, 1997.

[14] C. Diaconu. H1EPVEC/2.0. $W^{\pm}$ and Z production Monte Carlo generator based on EPVEC, 2000.

[15] E. Chabert et al. QBGFMAR: An Updated Phan Package for Cosmic and Halo Muon Topological Rejection in High P_T Physics Analysis. Technical report, H1, 1998. internal note H1-IN-556.

[16] G. Frising. Eine Likelihood-Analyse der H1 Jet-Daten. Master's thesis, RWTH Aachen, 2000.

[17] Harald Fritzsch and Dirk Holtmannspotter. The production of single t-quarks at LEP and HERA. *Phys. Lett.*, B457:186, 1999.

[18] A. Glazov. *Measurement of the Proton Structure Functions F2(x,Q2) and FL(X,Q2) with the H1 Detector at HERA*. PhD thesis, Humboldt-University Berlin, 1998.

[19] Particle Data Group. Review of Particle Physics, 2000.

[20] C. Grupen. *Teilchendetektoren (in German)*. BI Wissenschaftsverlag, 1993.

[21] K. Hagiwara, R.D. Peccei, and D. Zeppenfeld. Probing the weak boson sector in $e^+e^- \to W^+W^-$. *Nucl. Phys.*, B282:253, 1987.

[22] Tao Han and Jo Anne L. Hewett. Top charm associated production in high energy e^+e^- collisions. *Phys. Rev.*, D60:074015, 1999.

[23] B. Heinemann. Short introduction to the LOTUS code and CVS. Also see http://www-h1.desy.de/~rauschjr/nt.doc.html for description of variables.

[24] B. Heinemann. *Measurement of Charged Current and Neutral Current Cross Sections in Positron-Proton Collisions at* $\sqrt{s} \simeq 300\ GeV$. PhD thesis, University of Hamburg, 1999.

[25] H. Itterbeck. *Techniques and Physics of the Central-Myon-Trigger System of the H1-Detector at HERA*. PhD thesis, RWTH Aachen, 1997.

[26] H. Jung. The RAPGAP Monte Carlo For Deep Inelastic Scattering, version 2.07/00. *Comput. Phys. Commun.*, 86:147, 1995.

[27] C.S. Kim, Jungil Lee, and H.S. Song. Anomalous gauge boson couplings in high-energy e p collisions. *Z. Phys.*, C63:673–680, 1994.

[28] J. Kroseberg. Untersuchungen zum experimentellen Nachweis von W-Produktion mit dem H1-Detektor am Beispiel des Zerfalls $W \to \mu\nu_\mu$. Master's thesis, Institut fuer Kernphysik Westfaelische Wilhelms-Universitaet Muenster, 1998.

[29] U. Langenegger. *A Measurement of the Beauty and Charm Production Cross Sections at the ep Collider HERA*. PhD thesis, Inst.of Techn., Zurich, 1998.

[30] U. Langenegger and G. Tsipolis. On Muon Identification in the Barrel of the H1 Detector. H1 note, H1 collaboration, 1998. H1-04/98-542.

[31] N. Malden. *W production in ep collisions.* PhD thesis, University of Manchester, 2000.

[32] G. Martin. *Untersuchung von Prozessen des geladenen und neutralen Stroms mit dem H1-Detektor bei HERA.* PhD thesis, University of Hamburg, 1997.

[33] S. Mohrdieck. *Inelastische J/Psi-Erzeugung in Elektro-produktion am H1-Experiment bei HERA.* PhD thesis, University of Hamburg, 2000.

[34] A. Schoening. *Untersuchung von Prozessen mit virtuellen und reellen $W^{\pm}$ Bosonen am H1-Detektor bei HERA.* PhD thesis, University of Hamburg, 1996.

[35] V. Shekelyan. Simulation and Reconstruction in H1 Liquid Argon Calorimetry. Technical report, H1, 1993. internal note H1-IN-288.

[36] T. Sjoestrand. High Energy Event Generation with PYTHIA 5.7 and JETSET 7.4. *Comput. Phys. Commun.*, 82:74–90, 1994.

[37] Michael Spira. W boson production at NLO. 1999. hep-ph/9905469.

[38] J.A.M. Vermaseren. Two photon processes at very high-energies. *Nucl. Phys.*, B229:347, 1983.

[39] L. West. How to use the Heavy Flavour Working Group Track, Muon and Electron Selection Code. 1997.